A Novel Encoding Technology for Magnetic Resonance Imaging (MRI)

by

Frank John Rybicki III
BA, University of Pennsylvania, 1988

Submitted to the Harvard-MIT Division of Health Sciences and Technology
in Partial Fulfillment for the Degree of

Doctor of Philosophy in Medical Engineering

at the

MASSACHUSETTS INSTITUTE OF TECHNOLOGY

April 1994

Author _____
Harvard-MIT Division of Health Sciences and Technology
April 21, 1994

Certified by _____
Sow-Hsin Chen
Professor of Nuclear Engineering, MIT
Thesis Committee Chairman

Certified by _____
Sam Patz
Assistant Professor of Radiology, Harvard Medical School
Thesis Advisor

Certified by _____
Mirko Hrovat
Instructor in Radiology, Harvard Medical School
Thesis Supervisor

Certified by _____
Marie Foley Kijewski
Assistant Professor of Radiology, Harvard Medical School
Thesis Supervisor

Accepted by _____
Roger G. Mark
Co-Director, Harvard-MIT Division of Health Sciences and Technology

A Novel Encoding Technology for Magnetic Resonance Imaging (MRI)

Abstract

This project addresses a fundamental aspect of magnetic resonance imaging (MRI): the encoding of spatial information. Standard MRI methods utilize linear magnetic field gradients to encode spatial position into the signal. These methods are termed Fourier encoding since the MRI signal is reconstructed by Fourier transform (FT) mathematics. This work extends the scope of spatial encoding techniques by proposing a novel field geometry. The field is a function of two spatial variables, x and z, and has the form:

$$B_z(x,z) = g_x x \cos(q_z z). \qquad [1]$$

This encoding field, named the PERiodic-Linear (PERL) field for its periodicity in z and linearity in x, is significant for three reasons. First, it is a periodic function of a spatial variable. Second, it enables an imaging method in which two dimensional (2D) information is acquired while only a single encoding field is applied. Thus, switching of the encoding field is not required as in 2DFT imaging. Third, present imaging methods acquire information in k-space. When the PERL field is used for encoding, the signal (called the PERL signal) is acquired in a new vector space. This thesis characterizes the space by developing a set of transform equations defined as the PERL transform (PT). The PT has a set of intrinsic basis functions which are calculated numerically and implemented into a reconstruction algorithm. The reconstruction algorithm is tested by computer simulations: the point-spread function (PSF) of the algorithm is identified, conditions in which the PSF becomes ideal are discussed, and the algorithm is proven robust in the presence of noise. The reconstruction illustrates a successful method to obtain images given the PERL signal, but it does not address the feasibility of creating a coil system to generate the PERL signal from the sample. This thesis then presents a PERL coil design with cylindrical geometry. The design begins with a mathematical formalism for which the input is a desired or target field, and the output is the current density on a cylindrical form required to produce the field. Since the PERL field in [1] fails to satisfy Laplace's equation, a functional form approximating [1] is derived and used as the input to the formalism. The output current density is converted to the current pattern on the cylindrical surface by introducing the stream function. The final current pattern is expressed as the product of two terms. The first term determines the geometric configuration of the design. The second term is identified as an efficiency function of the coil written in terms of the coil radius and the two parameters g_x and q_z. The efficiency function is shown to limit the imaging volume. A second constraint on practical applications of the PERL technology is described by a tradeoff between the image resolution in z and the penetration of the field in the orthogonal direction x. This tradeoff creates a spectrum of imaging techniques in which the image field of view (FOV) in x is linked to the number of required switches of the current in the encoding coil. Two pulse sequences using the PERL technology for single excitation imaging of static spins are presented to elucidate this spectrum. On one end of the spectrum is a pulse sequence which requires zero field switching. This sequence optimizes speed, but it is constrained by a limited penetration of the field into the sample along x. While this is ideal for surface imaging, field switching is required for deeper penetration. The number of required field switches (i.e. speed) is linearly related to the penetration along x (i.e. FOV). Thus, PERL imaging creates the opportunity to minimize the number of field switches to accommodate a particular FOV. On the other end of the spectrum, a pulse sequence with unrestricted penetration is obtained with a large number of field switches. In this limiting case PERL imaging reduces to echo-planar imaging (EPI).

Thesis Advisor: Samuel Patz. Assistant Professor of Radiology, Harvard Medical School

Biographical Note

Dr. Frank John Rybicki III was born in Pittsburgh, PA on August 23, 1966 to the loving parents Dr. Frank and Annette Rybicki. The Rybicki family relocated to Cherry Hill, NJ in 1970 where they have lived ever since. Dr. Rybicki spent much of his youth playing competitive tennis, and he graduated from The Lawrenceville School, Lawrenceville, NJ in 1984. He subsequently attended The University of Pennsylvania, Philadelphia, PA where he received a Bachelor of Science degree in mathematics in 1988. Dr. Rybicki then enrolled in the Harvard-MIT Division of Health Sciences and Technology, a joint program between Harvard Medical School, Boston, MA and The Massachusetts Institute of Technology, Cambridge, MA. In addition he became a member of the MD/PhD program at Harvard Medical School. He completed his PhD in Medical Engineering in 1994 and plans to complete his MD in 1996.

Acknowledgments

Over the last six years I have become deeply indebted to several individuals at Harvard and MIT, but none are more important to me than my research advisors Marie Foley Kijewski and Sam Patz at The Brigham and Women's Hospital Department of Radiology. It is rare for a graduate student to have an advisor who is superlative as a scientist and as a person; I had two of them.

Marie accepted me into her laboratory as a first year medical student and gave me the responsibility of my own mathematical project. Working with Marie taught me that there is a place in medicine for a student of mathematics, a message I take home every day. In addition to providing me the opportunity to work independently, Marie has been a guiding and supportive influence throughout the years. In this time I have realized that both Marie and Sam have the innate sense of an ideal mentor: allowing autonomy while maintaining stability.

During the past two years I have been grateful to Sam on so many accounts that they are too numerous to list. Happily, though, I'll scratch the surface a bit. First and foremost is Sam's seemingly endless scientific knowledge and keen intuition. His guidance made my transition to the MRI group smooth, and his advising and dedication allowed me to complete my thesis work without significant delays. Sam's gift as a thesis advisor was his ability to respect me as a peer while teaching me as a student. However, my appreciation is deeper than the scientific (and financial) support he provided. Along with Marie, he has always maintained an interest in my life as a whole and created an environment where I could improve as an individual as well as a scientist. If I have matured intellectually or personally over the past six years, it is because of their careful attention and nurturing. Not only are they my role models, but also they are my lifelong friends.

I am also grateful to Mirko Hrovat and Yuly Pulyer at The Brigham and Women's Hospital Department of Radiology. I am one of the long line of students in our lab who was fortunate enough to have Mirko's intellectual stimulation and scientific advice. On many occasions I have counted on Mirko's feedback on new ideas and followed his recommendations which lead me to solutions. Over the past two years I have also gained a great respect and admiration for Yuly who brought to our group the idea of a periodic encoding field for MRI which ultimately lead to this thesis.

There are also several individuals outside our department who have made a positive impact on my work. First, I would like to thank Professor Chen at the MIT Department of Nuclear Engineering for accepting the role as my thesis chairperson and overseeing my project. In addition, I would like to thank Eric McFarland who spent countless hours teaching me the essentials of engineering in my early years of graduate school.

Finally, and most importantly, I thank my parents for their overwhelming love and support. Both have dedicated themselves to making me the best person I could possibly become, and I hope that I have made them proud parents now and forever.

Table of Contents

List of Figures

Figure 4.3.1.a Plot of the Bessel function $J_n(x)$ for several orders of n.

Figure 4.3.1.b Plot of selected modified Bessel functions.
Figure 4.5.1 Assumed spin density equal to one in the square region between zero and two in both the x and z dimensions. The axes are labeled by pixel number. The origin is at pixel (33,33), and the pixel dimensions are 0.12 cm square.

Figure 4.5.2 Calculated PERL signal from the spin density equal to one in the square region between zero and two in both the x and z dimensions.

Figure 4.5.3 Preliminary coil design with cylindrical geometry to produce a periodic field in the z dimension.

Figure 4.5.4 Preliminary coil design with rectangular geometry to produce a periodic field in the z dimension.

Figure 4.5.5 Three dimensional plot of the field generated by the preliminary rectangular coil design.

Figure 4.5.6 Plot of B_z vs. z illustrating the periodicity along z for the rectangular geometry. In this plot, $x=0.125\,a$ and $y=0$.

Figure 4.5.7 Plot of B_z vs. d illustrating the penetration problem as the spacing between current elements decreases. In this plot $x=0.25\,a$, $y=0$, and $z=0.125\,a$.

Figure 4.6.1 Modified pulse sequence using two PERL coils.

Figure 4.7.1 Preliminary reconstruction based on the addition theorem for Bessel functions. Note the severe ringing which makes this reconstruction algorithm unsatisfactory.

Figure 5.2.1 The PERL transform between the variables m and x.

Figure 5.3.1 Plots of $\phi_m(x)$ for m = 0, 25, and 50 respectively.

Figure 5.4.1 The system function centered at x'=0 computed from the basis functions $\phi_m(x)$. $M_{max} = 51$, and the separation between points along x is 0.05.

Figure 5.4.2 The function diff(x) as defined in the text.

Figure 6.3.1. One dimensional rectangular input having width 0.01 cm and centered at the origin (x'=0). This function approximates $\delta(x)$.

Figure 6.3.2 Reconstruction of function approximating $\delta(x)$. Compare with the form of h(x-x').

Figure 6.3.3 Input spin density equal to one in the square region between zero and two in both the x and z dimensions. The axes are labeled by pixel number. The origin is at pixel (33,33), and the pixel dimensions are 0.12 cm square.

Figure 6.3.4 Reconstructed spin density. Note the ringing along x (Fourier) is comparable to the ringing along z (PERL).

Figure 6.3.5 Nonuniform input spin density. The axes are labeled by pixel number. The origin is at pixel (33,33), and the pixel dimensions are 0.12 cm square.

Figure 6.3.6 Reconstruction of nonuniform spin density.

Figure 6.3.7 Input spin density identical to square box between zero and two in both the x and z dimensions with the addition of zero mean Gaussian noise of maximum amplitude 0.1. The origin is at pixel (33,33), and the pixel dimensions are 0.12 cm square.

Figure 6.3.8 Reconstruction of spin density in the presence of noise.

Figure 7.2.1 Cylindrical coordinate system used in the PERL coil design.

Figure 8.3.1 Vector plot of the current density $\bar{j}$. Constants are set to one to illustrate the functional form. Vector arrows point in the direction of the current density; vector lengths indicate the magnitude of the current density.

Figure 8.4.1 Plot of the PERL coil streamlines with constants set to one to illustrate the functional form. See text for description.

Figure 8.5.1 The efficiency function for the PERL coil as a function of coil radius a. The lower plot includes larger values of a.

CHAPTER 1. Introduction.

Section 1.1 Definition of the PERL field

This project investigates the encoding of spatial information for magnetic resonance imaging (MRI). Specifically, a new magnetic field geometry is presented, and its properties are discussed.[1,2,3,4,5] The encoding field appears in Figure 1.1.1 and depends on two spatial variables, x and z:

$$B_z(x,z) = g_x x \cos(q_z z) \qquad [1.1.1]$$

This field is called the PERL field since it is PERiodic in the z-dimension and Linear in the x-dimension. The PERL field geometry offers fundamentally new ways to image, and it requires a new reconstruction algorithm and a new coil design. For example, to image stationary spins, a pulse sequence resembling a spin echo experiment is described in Chapter 4 which requires no switching of the current in the encoding coil during the acquisition of an entire two dimensional (2D) data set. This is achieved with the PERL field applied as a "pre-encode" field between the 90° and 180° pulses, and the signal is acquired with a standard linear gradient. Since the encoding fields are not switched during data acquisition, this method is theoretically faster than echo-planar imaging (EPI), the fastest MRI technique available today.

The problem which arises from the pulse sequence introduced above and detailed in Chapter 4 is the limited penetration depth of the PERL field into a sample. As a solution, a second pulse sequence is illustrated which allows deeper penetration but requires field switching. The number of required field switches is linearly related to the field penetration. Thus, the PERL field creates a spectrum of imaging techniques in which the number of required field switches is related to the image field of view (FOV),

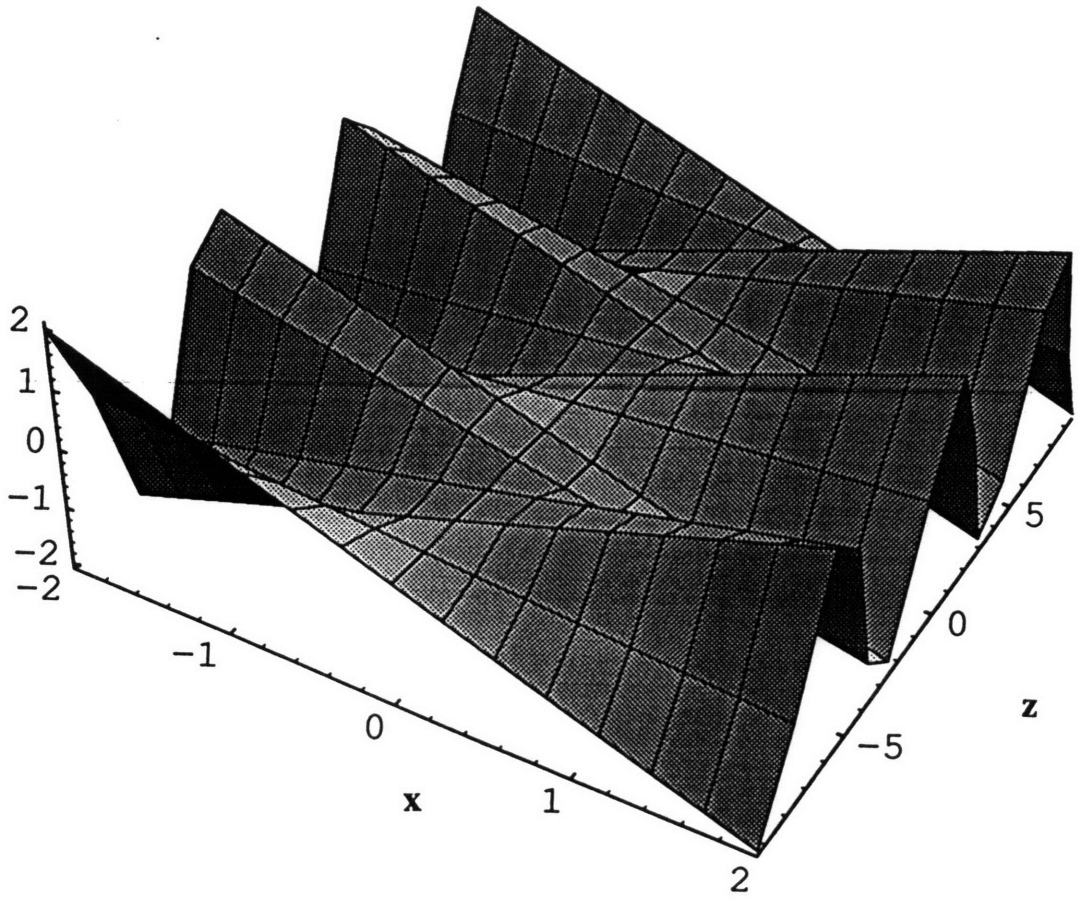

Figure 1.1.1 The PERL encoding field, $B_z(x,z) = g_x x \cos(q_z z)$.

and PERL imaging creates the new opportunity to minimize the number of field switches to accommodate a particular FOV.

This thesis focuses on two consequences of spatial encoding with the PERL field geometry. First, the acquired signal is not related to the image spin density by a two-dimensional Fourier transform (2DFT). That is, the PERL signal is acquired in a new vector space. This thesis characterizes the space by developing a set of transform equations defined as the PERL transform. The PERL transform is demonstrated by: a) numerical calculation of its intrinsic basis functions, and b) implementation of these basis functions into a reconstruction algorithm. The algorithm is then tested by computer simulation and several of its properties are described. In particular, the point spread function of the algorithm is identified, and the conditions for which it becomes ideal are presented. Additional computer simulations prove the robustness of the algorithm in the presence of noise.

The second consequence of spatial encoding with the PERL geometry is the requirement of a coil system to create the functional form of the field. This thesis presents a PERL coil design with cylindrical geometry. The coil is designed with a mathematical formalism[6,7] for which the input is the desired or target field, and the output is the current density on a cylindrical form required to produce the field. Since the PERL field in Eq. 1.1.1 fails to satisfy Laplace's equation, an approximate functional form is derived and used as the input to the formalism. The output current density is then converted to the current pattern on the cylindrical surface by introducing the stream function.[8,9,10] The final current pattern is expressed as the product of two terms. The first term determines the geometric configuration of the design. The second term is identified as a coil efficiency function, and its dependencies on the coil radius is shown to limit the imaging volume.

Section 1.2 Significance of the PERL technology

The PERL field as an encoding field for MRI is significant for three reasons. First, it is a periodic function of a spatial variable. Second, it enables an imaging method in which 2D information is acquired while only a single encoding field is applied. Thus, switching of the encoding field is not required as it is in 2DFT imaging. Third, the vector space in which the PERL signal is acquired is not k-space. The characterization of the PERL transform is significant not only because it allows reconstruction of the PERL signal, but also because it represents a novel mathematical transform with a set of basis functions which are shown to have spatial localization. Additional applications of the PERL transform are currently under investigation. Although the coil design is based on an existing mathematical formalism, the solution for the PERL field profile is also unique.

Section 1.3 Related Work of Others

While there are no direct MRI techniques analogous to the PERL technology, imaging methods utilizing mathematics similar to the PERL transform are described, and coil designs which resemble the PERL coil are discussed. The first part of this section emphasizes the mathematics; the second part describes the hardware.

The PERL transform mathematics is based on Bessel functions. In particular, each spin echo obtained by encoding with the PERL field is modulated by a Bessel function where the order of the Bessel function equals the index of the spin echo. Because this unique from of the signal is not reconstructed by 2DFT mathematics, this section touches on some of the many FT modifications and non-Fourier transformation techniques applied to magnetic resonance. Although none of these modifications or techniques is directly related to the PERL transform, they include methods to either supplant the FT[11], modify the FT for a particular pulse sequence[12,13], or improve a

characteristic of the imaging system.[14] Hankel transform applications also appear in the literature;[15] in particular, Hankel transforms are proven effective in systems which use data collected in the presence time varying or rotating gradients.[16]

The idea of rotating gradients for MRI introduced by Hinshaw[17] is known as the sensitive point method. This method is extremely time inefficient because only a single image pixel is sensitive, and changing the sensitive point requires either changing the gradient offsets or physically moving the sample. In 1985 Macovski introduced a dramatically new method of utilizing rotating gradients.[18] The idea behind his technique is to acquire a single signal in the presence of a rotating gradient. Image data at different points in space is then obtained by a mathematical operation which yields spatial information at a single point. By varying the nature of the mathematical operation, this technique becomes the mathematical equivalent to physically moving a sensitive point through the sample. This new technology originally produced a localization function about the sensitive point which follows the Bessel function of order zero. (This function is written $J_0(x)$ and is illustrated in Figure 4.3.1.) Numerous improvements have been described for the localization function,[19] many of which involve combinations of Bessel functions.

The second part of this section discusses hardware which shows resemblance to the PERL coil. The most important contribution to the literature is the zig-zag coil.[20] This is an RF coil used for spectroscopy, as opposed to the PERL coil which is used for spatial encoding. The zig-zag coil utilizes alternating current to limit the penetration of the RF field to avoid contamination of the spectrum from underlying tissues. Since the zig-zag coil has alternating current elements, it produces a periodic field. For the spectroscopic application, this limits the surface interrogated into discrete segments separated by the wavelength of the coil. The reduced volume for which signal is

observed is therefore a disadvantage for the zig-zag coil, whereas the periodicity of the PERL field is the basis of the imaging technique.

Section 1.4 Organization of Thesis

This thesis is organized into four parts. The first part consists of an introduction to MRI (Chapter 2) and a review of fast imaging techniques (Chapter 3). Readers familiar with these topics may choose to begin with the second part (Chapter 4) which presents the pulse sequences utilizing the PERL field and discusses the tradeoffs of the imaging techniques including the penetration problem for periodic fields. Although Chapter 4 is included in this thesis to give a complete picture of PERL imaging, this part is based on the ideas of two members of this thesis committee (Sam Patz and Mirko Hrovat) and Yuly Pulyer, Visiting Associate Professor of Radiology at Harvard Medical School. The third and fourth parts of this thesis are original to the author. The third part of this work is the characterization of the PERL transform and the reconstruction algorithm which appear in Chapters 5 and 6. The final part is the design of the PERL coil in Chapters 7 and 8.

Chapter 1 References

[1] S Patz et al. Novel Encoding Technology for Ultrafast MRI. Society of Magnetic Resonance in Medicine 11, August, 1992, p.111.
[2] FJ Rybicki et al. A Novel Ultrafast MRI Technology . Proceedings of the American Association for the Advancement of Science 1993 Annual Meeting, Abstract #241, Feb. 1993.
[3] FJ Rybicki et al. Reconstruction Algorithm for a Novel Ultrafast MRI. Society of Magnetic Resonance in Medicine 12, August, 1993, p.1246.
[4] S Patz et al. Novel Encoding Technology for Ultrafast MRI. (Submitted to Magnetic Resonance in Medicine.)
[5] FJ Rybicki et al. Reconstruction Algorithm for Novel Ultrafast MRI. (Submitted to Magnetic Resonance in Medicine.)
[6] R Turner. A target field approach to optimal coil design, J. Physics D. 19, L147, 1986.
[7] R Turner and RM Bowley. Passive screening of switched magnetic field gradients, J. Physics E. 19, 876, 1986.
[8] Edelstein et al. Current streamline method for coil construction. US Patent 4,840,700. Jun. 20, 1989.
[9] Schenck et al. Transverse gradient field coils for nuclear magnetic resonance imaging. US Patent 4,646,024. Feb. 24, 1987.
[10] Roemer et al. Self-shielded gradient coils for nuclear magnetic resonance imaging. US Patent 4,737,716. Apr. 12, 1988.
[11] CH Paik and MD Fox. Fast Hartley transforms for image processing. IEEE Transactions on Medical Imaging Vol 7, No 2, Jun 1988, p. 149.
[12] MM Tropper, Image reconstruction for the NMR echo-planar technique, and for a proposed adaption to allow continuous data acquisition. Journal of Magnetic Resonance 41:193, 1981.
[13] SJ Norton. Fast magnetic resonance imaging with simultaneously oscillating and rotating field gradients. IEEE Transactions on Medical Imaging Vol MI-6, No 1, Mar 1987, p. 21.
[14] TN Ma and K Takaya. High-resolution NMR chemical shift imaging with reconstruction by the chirp z-transform. IEEE Transactions on Medical Imaging Vol 9, No 2, Jun 1990, p. 190.
[15] WE Higgins and DC Munson. A Hankel transform approach to tomographic image reconstruction. IEEE Transactions on Medical Imaging Vol 7, No 1, Mar 1988, p. 159.
[16] I Shenberg and A Macovski. A direct MRI Hankel transform system using rotating gradients. IEEE Transactions on Medical Imaging Vol MI-5, No 3, Sep 1986, p. 121.
[17] WS Hinshaw. Image formation by nuclear magnetic resonance: the sensitive point method. Journal of Applied Physics 47:3709, 1976.
[18] A Macovski. Volumetric NMR imaging with time-varying gradients. Journal of Magnetic Resonance in Medicine 2:29, 1985.
[19] DC Noll et al. A homogeneity correction method for MRI with time-varying gradients. IEEE Transactions on Medical Imaging Vol 10, No 4, Dec 1991, p. 629.
[20] T Nakada et al. Phosphorus-31 spectroscopy of the stomach by a zig-zag coil. Magnetic Resonance in Medicine 5:449, 1987.

Chapter 2. Fundamentals of MRI

Section 2.1. Introduction and the concept of resonance

A plethora of descriptions of MRI exist, including those in textbooks,[1,2,3,4,5] the scientific literature,[6,7,8,9] and former student theses.[10] The approach in this chapter leads quickly to a description of k-space, the two-dimensional vector space in which MR data is acquired.

The goal of all medical imaging modalities is to measure and resolve spatial information about the human body. There are a wide variety of imaging modalities to perform these tasks including projection radiography, x-ray computed tomography, ultrasound, nuclear medicine, and MRI. This chapter focuses on MRI and describes how magnetic resonance is used to create medical images.

The standard approach to teaching MRI begins with the magnetic properties of nuclei, and this is the focus of Section 2.2. However, it is useful to first introduce the concept of resonance since magnetic resonance is merely one of many forms of resonance in nature. The textbook[11] definition of resonance states that whenever a system capable of oscillating is acted on by a periodic series of impulses having a frequency equal or nearly equal to one of the natural frequencies of oscillation of the system, the system is set into oscillation with a relatively large amplitude. In terms of NMR, when magnetic nuclei are placed in a static magnetic field, they oscillate in their motion with a characteristic frequency called the Larmor frequency as described in Section 2.3. When a second (magnetic) field oscillating at the same frequency is applied, resonance absorption occurs, thus the name nuclear magnetic resonance. (Note that throughout this thesis the term "field" refers to a magnetic field.)

Section 2.2 Magnetic properties of nuclei

The discussion of NMR begins with the magnetic properties of atomic nuclei. For individual nuclei, these properties are characterized by either $\bar{\mu}$, the magnetic moment, or $\bar{L}$, the angular momentum. (Note that throughout this thesis the "bar" symbol "$\bar{}$" denotes a vector quantity and the "double bar" symbol "$\bar{\bar{}}$" denotes a matrix.)

A magnetic moment is established by the rotation of a charge about an axis; angular momentum is established by the rotation of mass about an axis. Thus, any object with a magnetic moment has a corresponding angular momentum. It is worth noting that an object without a net charge may have a nonzero angular momentum; such is the case with a neutron. Although electrically neutral, the rotating neutron possesses a magnetic moment because its charge components are unequally distributed within its volume.

The vectors $\bar{\mu}$ and $\bar{L}$ are linearly related with proportionality constant γ, the gyromagnetic ratio of the species:

$$\bar{\mu} = \gamma \bar{L}. \qquad [2.2.1]$$

The value of the gyromagnetic ratio may be derived either classically or quantum mechanically; for these derivations the reader is referred to the references.[12] For protons, the most abundant nuclei in the body and the nuclei most often used for MRI, the classical model yields accurate results for γ. However, the quantum model is required for other nuclei. A table of experimentally determined values for the gyromagnetic ratio appears in von Jako.[13] The remainder of this chapter and this thesis considers only the hydrogen nucleus which has a gyromagnetic ratio of $\gamma = (2\pi)\ 4257.6$ rad/G s.

Section 2.3. Spinning nuclei in a magnetic field, uniform magnetic fields

This section provides a classical description of a spinning proton in a static magnetic field $\overline{B}_0$ directed along the +z axis. When a nuclear magnetic moment is exposed to $\overline{B}_0$, it experiences a torque defined in Eq. 2.3.1 which aligns it with the field (i.e. along z) in a manner similar to the alignment of a compass needle (a bar magnet) with the earth's magnetic field. While the compass needle undergoes rotational motion toward its equilibrium position or minimum energy state, the magnetic moment precesses because in addition to experiencing a torque, it also has an intrinsic angular momentum. The precessional motion is often described classically by analogy with a gyroscope or a spinning top[14] where the top experiences a torque from gravity and its own internal spin from angular momentum. Thus, the nucleus precesses about the direction of $\overline{B}_0$ as seen in Figure 2.3.1.[15] (Note that in MRI jargon, the term "spin" refers to the proton's magnetic moment. As described in Section 2.4, the most common goal in MRI is to create a map of the density of these moments which is colloquially called the "spin density".)

For the present discussion consider a nucleus with magnetic moment $\overline{\mu}$ and angular momentum $\overline{L}$. Application of $\overline{B}_0$ exerts a torque $\overline{\tau}$ on the proton. The torque is related to the magnetic field via

$$\overline{\tau} = \overline{\mu} \times \overline{B}_0 \qquad [2.3.1]$$

and is related to the angular momentum via

$$\overline{\tau} = \frac{d}{dt}\overline{L}. \qquad [2.3.2]$$

Combining Eqs. 2.3.1 and 2.3.2 gives $\frac{d}{dt}\overline{L} = \overline{\mu} \times \overline{B}_0$, and substituting Eq. 2.2.1,

$$\frac{d}{dt}\overline{L} = \gamma \overline{L} \times \overline{B}_0. \qquad [2.3.3]$$

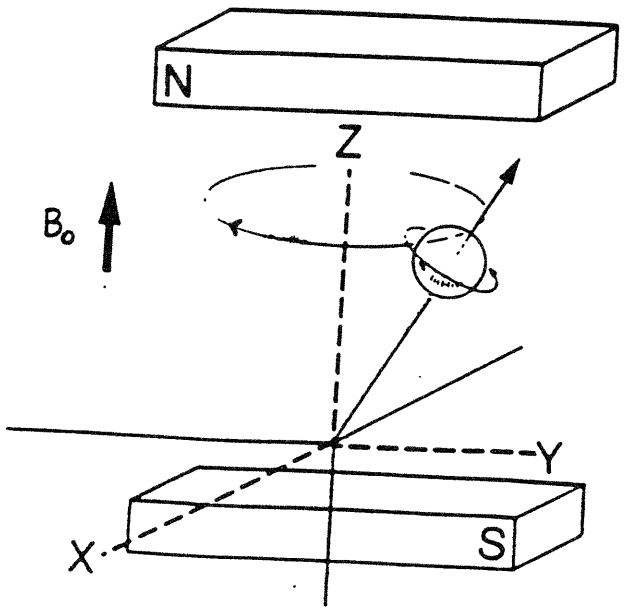

Figure 2.3.1 Nuclear precession in a static magnetic field.

Equation 2.3.3 is the Larmor equation which describes the precessional frequency $\omega_0 = -\gamma B_0$ where the minus sign indicates that the precession is anticlockwise. This equation is usually written without denoting the sense of rotation:

$$\omega_0 = \gamma B_0. \qquad [2.3.4]$$

The significance of Eq. 2.3.4 cannot be overemphasized; as seen throughout this text, it is the fundamental equation of MRI. For a magnetic moment in a field $\overline{B}_0$, the precessional frequency, called the Larmor frequency, and the magnitude of the field are linearly related with proportionality constant γ.

The quantum mechanical derivation of the Larmor equation appears in Pake[16] and emphasizes that for protons there are two possible spin orientations in a magnetic field. These orientations or states are called "up" and "down" corresponding to the alignment of the nuclei with the field. The "up" state is an alignment parallel to the field and is at a lower energy than the "down" state which is an alignment antiparallel to the field. In Figure 2.3.1, the spin is drawn in the up or parallel direction. For the purposes of imaging, a sample composed of many protons is adequately described by the net magnetic moment per unit volume $\overline{M}$ defined as the vector sum of the individual moments and divided by the volume as seen in Figure 2.3.2. When a uniform field $\overline{B}_0$ is applied to a sample, the equilibrium value of $\overline{M}$ points in the direction of $\overline{B}_0$. As mentioned earlier in this section, this is by convention the +z direction, and the component M_z is termed the "longitudinal magnetization".

Application of $\overline{B}_0$ to a proton sample at the resonance frequency stimulates the two possible transitions, (up)→ (down) and (down)→(up) with equal probability. Therefore, a net absorption or emission of energy from the sample requires a population difference between the two states. Defining the number of protons in the up state as N_{up} and the

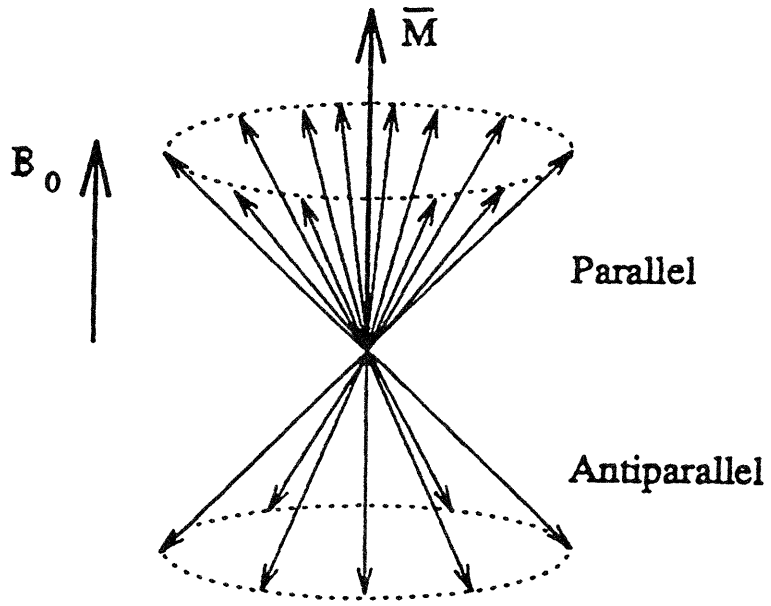

Figure 2.3.2 The net magnetic moment or magnetization vector.

number of protons in the down state as N_{down}, the ratio N_{up}/N_{down} follows the Boltzmann distribution[17]

$$\frac{N_{up}}{N_{down}} = \exp\left[\frac{2\,\mu\,B_0}{k\,T}\right] \qquad [2.3.5]$$

where k is Boltzmann's constant and T is temperature in degrees Kelvin. At 27° C and a field strength of 5 kGauss, this ratio equals $1 + 4 \times 10^{-6}$. This very small excess of protons in the lower energy state is responsible for generating the MRI signal as described in Section 2.9.

Section 2.4. Spinning nuclei in a magnetic field, magnetic field gradients

The previous two sections describe the fundamentals of MR and emphasize Eq. 2.3.4, the linear relationship between precessional frequency and magnetic field strength. At this stage of the discussion, MR remains an interesting phenomena, but the central question remains, "How can this phenomena be used for imaging?"

For a moment put aside the previous developments and make the following assumption: a method exists which converts spatial information, the unknown in medical imaging, into spatial frequency information. Furthermore, assume that this method provides a linear mapping between spatial information and spatial frequency information. Given this assumption, the desired spatial information would be related to the linearly mapped frequency information by an appropriately dimensioned FT. For example, a planar (2D) image could be reconstructed via the 2DFT of the 2D frequency information.

Now reconsider MR as the mechanical mapping between spatial information and spatial frequency information assumed above. The mapping is accomplished by applying a magnetic field to the region of the body which is being imaged. The magnetic field is called an encoding field because it encodes spatial data by the simple equation

$$\text{spatial frequency} = (\text{constant})(\text{field strength}). \qquad [2.4.1]$$

Equation 2.4.1 may look familiar; in fact, it is a written description of

$$\omega_0 = \gamma B_0. \qquad [2.3.4]$$

Now return to the ideas developed in the first three sections of this chapter: if the field strength is not uniform but has a constant slope, there will be a linear dependence between elements in space and their Larmor frequencies. This is the fundamental connection between MR and imaging: the ability to identify a spatial element by its frequency which in turn is determined by the field strength at that spatial element.

The next logical step is to demonstrate the material presented above with an example imaging experiment. Before the experiment, however, consider this brief historical note. The first experimental description of NMR appeared in 1938.[18] This one page communication by Rabi in Physical Review laid the groundwork for MR applications in physics, chemistry, and biochemistry. In 1944 Rabi received the Nobel prize in Physics. NMR was demonstrated in 1946 by Bloch[19] and Purcell[20] who shared the Nobel prize in Physics in 1952. Given the amount of attention to NMR, the Larmor equation was clearly etched in the minds of thousands of scientists by the 1950s. However, the concept of incorporating the notion of a spatial element into the Larmor equation and thus using MR for imaging was not proposed until 1973![21]

Given the above introduction, consider the following experiment which measures the density of proton magnetic moments in a sample. As mentioned in Section 2.3, in MRI jargon the density of proton magnetic moments is termed the "spin density" and is denoted by ρ. For this experiment, the sample consists of two tubes filled with water and aligned

in the x-dimension as shown in Figure 2.4.1. In addition, assume $\rho(x,y,z) = 1$ inside the tubes while $\rho(x,y,z) = 0$ outside the tubes. As seen in the figure, a constant magnetic field in the positive z direction with magnitude B_0 is applied to both tubes. What is the effect of this applied field? Since an identical magnetic field is applied to all the spins, they share the same behavior. Specifically, all the spins in the system precess about the positive z axis with a Larmor frequency given by Eq. 2.3.4.

The magnetic field in Figure 2.4.1 has mapped spatial information into frequency information, but since the magnetic field is constant, all of the spatial properties in the x-dimension are mapped to a single frequency. Consequently, the details of the properties along x are lost by the constant magnetic field. In order to retain these properties so they can be decoded by a FT, a 1-1 mapping between the spatial data and the frequency data is required; in standard MRI this 1-1 mapping (or encoding) is accomplished by exposing the system to the magnetic field

$$B_z = B_0 + G_x x \qquad [2.4.2]$$

where the spatial information along x is encoded by the linear magnetic field gradient G_x. (See Figure 2.4.2) Although the idea expressed by Eq. 2.4.2 is straightforward, the form of this expression often causes confusion. The gradient G_x varies over the x axis, but the variation occurs in B_z, the z-component of the field.

With the field in Eq. 2.4.2 applied to the system of two tubes, the resulting Larmor frequencies of the spins depend on the position of the spins along the x axis. Since the gradient G_x encodes the spatial information along x as frequencies, G_x is termed the frequency encoding gradient. A plot relating the positions and the Larmor frequencies would resemble Figure 2.4.3.

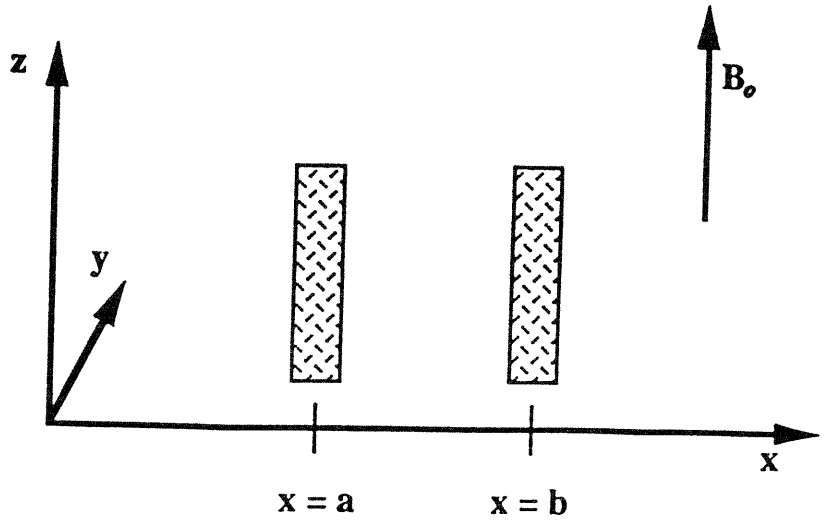

Figure 2.4.1 Two tubes filled with water aligned along x in the presence of the static magnetic field.

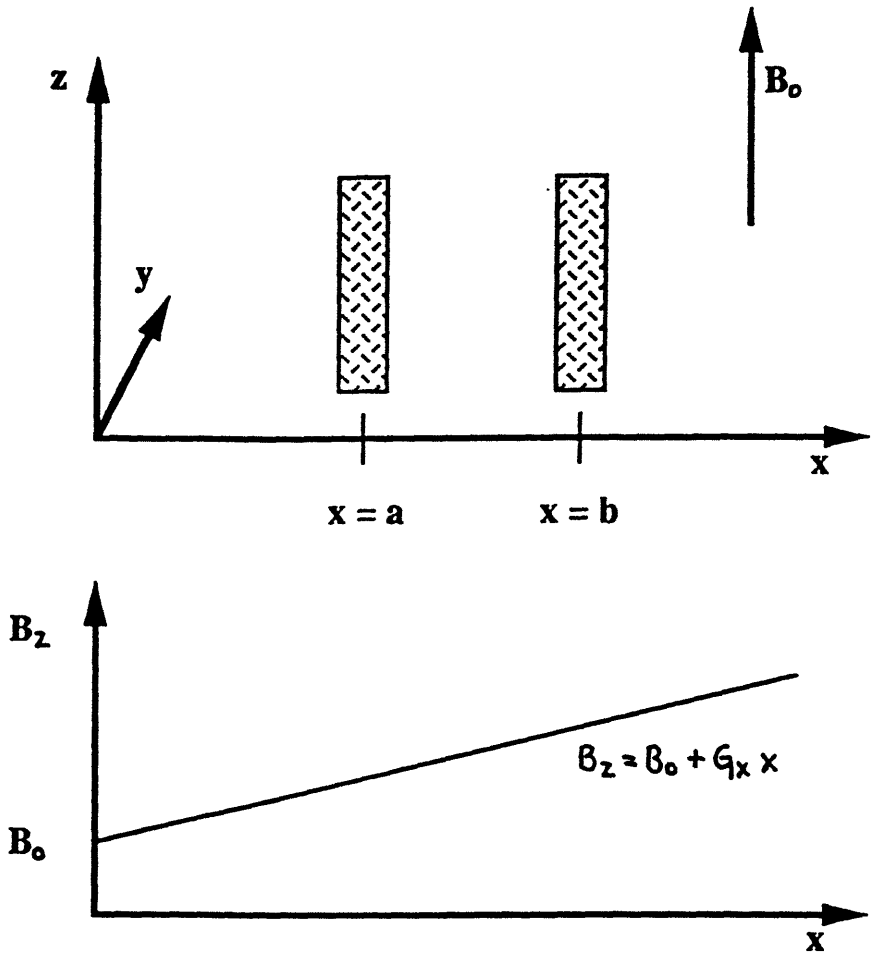

Figure 2.4.2 Two tubes filled with water aligned along x in the presence of the static field and a gradient along x.

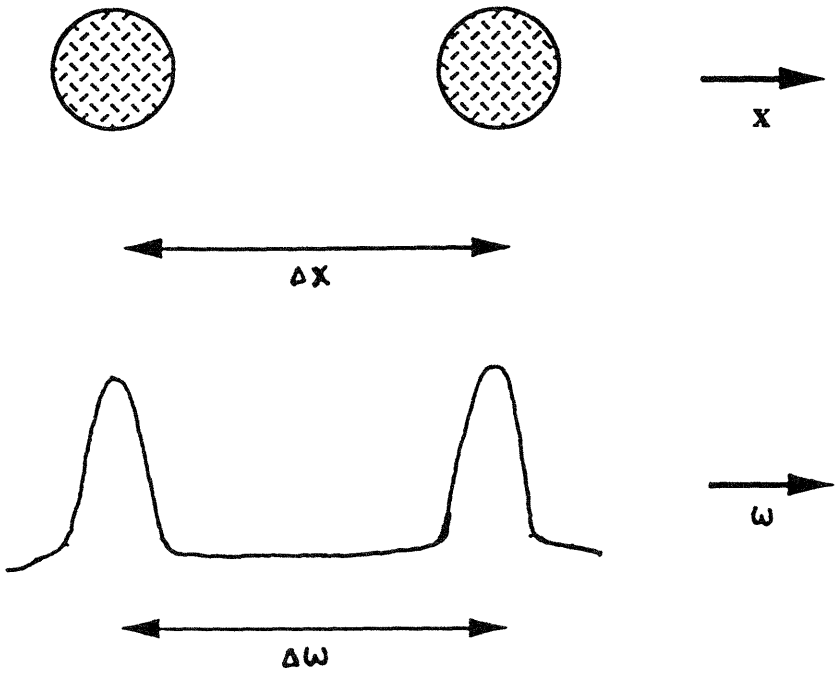

Figure 2.4.3 Plot relating the positions to the Larmor frequencies for the two tubes of water.

Since γ is known and G_x is fixed in the experiment, spatial information can be obtained by measuring the frequencies of the spins in the system. Defining the measured frequency separation between the tubes as $\Delta\omega$, then $\Delta\omega = \gamma \Delta B$, and since $\Delta B = G_x \Delta x$, the frequency separation can be expressed as $\Delta\omega = \gamma G_x \Delta x$. Solving for the spatial separation, the only unknown,

$$\Delta x = \frac{\Delta\omega}{\gamma G_x}, \qquad [2.4.3]$$

and the spacing between the tubes is determined. Thus, MR with a linear gradient along x is used to map the spatial separation between the two tubes.

To summarize, this section introduces magnetic field gradients with an experiment to describe 1D encoding of spatial information. The notion of encoding is fundamental to MRI in general and is the focus of this thesis, and the next two sections of this chapter are devoted to developing this concept.

Section 2.5. Phase encoding

The previous section uses an example of two tubes filled with water to introduce spatial encoding by varying the Larmor frequency of the sample in the x-dimension. As previously mentioned, this process is given the name frequency encoding. However, in the preliminary experiment just described, the sample was chosen with a high degree of symmetry. That is, the tubes were conveniently aligned along x, the direction of the magnetic field gradient. Because of this simplified case, the one-dimensional projection in Figure 2.4.3 provided a complete description of the spatial separation along x. In the more general situation of 2D imaging, there is no a priori symmetry between the sample and the magnetic field gradients. Suppose, for example, that the tubes were aligned as in Figure 2.5.1. In this situation, the frequency spectrum corresponding to the sample would not be able to distinguish between the two tubes.

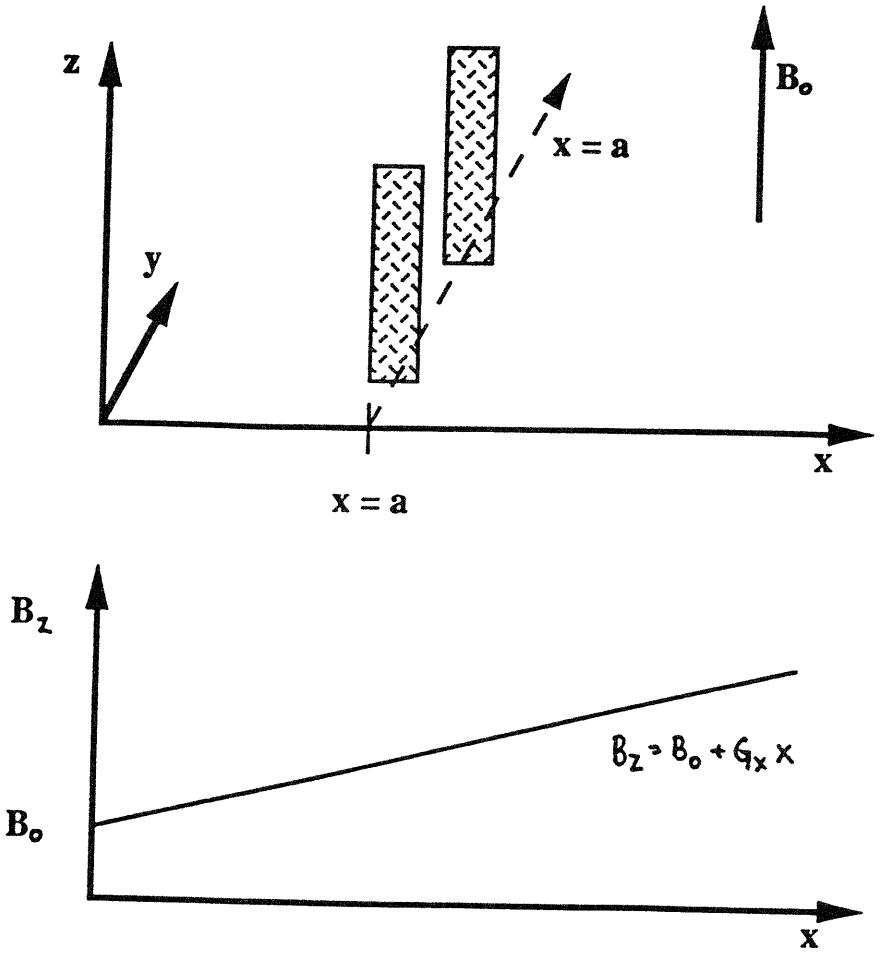

Figure 2.5.1 Two tubes filled with water with the same value of x but different values of y.

This second example illustrates the necessity for more information to accurately resolve 2D properties of the sample. The standard MRI method used to resolve two spatial dimensions is an extension of the experiment described above which uses 2D Fourier analysis. 2D Fourier techniques begin with the 1D procedure used to image the tubes of water. Assume that n data points are collected in the presence of a linear x gradient. The linear gradient encodes the sample along x, and a 1DFT produces a series of n spatially encoded data points. What about the y dimension? To obtain information along y, the y-axis is encoded by taking advantage of another property of the sample called phase.

The discussion of phase encoding begins by mathematically defining the phase of a spin created by an external field gradient applied to the sample. Consider the α-axis where α is an arbitrary direction in the sample, and a gradient in this direction is named G_α. (For example, the α-axis may be the x-axis, and the corresponding G_α gradient would be G_x, as in the case of the two water tubes.) Given these definitions, the phase of a spin in the α direction is defined as

$$\phi_\alpha \equiv \int_0^{t_\alpha} \omega_\alpha(t')\, dt' \qquad [2.5.1]$$

where ω_α is the precessional frequency caused by the gradient in the α direction which follows Eq. 2.3.4:

$$\omega_\alpha = \gamma B_\alpha. \qquad [2.5.2]$$

Replacing B_α with the field strength αG_α and substituting into Eq. 2.5.1,

$$\phi_\alpha \equiv \gamma \alpha \int_0^{t_\alpha} G_\alpha(t')\, dt' \qquad [2.5.3]$$

where t_α represents the duration that G_α is applied along the α-axis. Equation 2.5.3 is simplified by the assumptions that the gradient is time independent and has a constant magnitude equal to G_α during the time which it is applied. Then the phase in the alpha direction becomes

$$\phi_\alpha = \gamma\, \alpha\, G_\alpha\, t_\alpha. \qquad [2.5.4]$$

Now reconsider the problem of encoding spatial information along the y dimension. Equation 2.5.4 with the substitution $\alpha = y$ illustrates that a gradient G_y produces a phase along y

$$\phi_y \equiv \gamma\, y\, G_y\, t_y. \qquad [2.5.5]$$

As described in Section 2.6, this is precisely the method used in MRI to encode information along y, and since the gradient G_y encodes the phase of the spins, it is termed the phase encoding gradient.

The definition of phase in Eq. 2.5.1 suggests that there is not only a phase induced by the gradient G_y, but also a phase induced from G_x, the frequency encoding gradient. Thus, a total phase Φ is defined as the sum of the phases created by all gradients applied to the sample. For the two linear gradients G_x and G_y, it has the functional form

$$\begin{aligned} \text{total phase} \equiv \Phi &= \phi_x + \phi_y \\ &= \gamma\, x \int_0^{t_x} G_x(t)\, dt + \gamma\, y \int_0^{t_y} G_y(t)\, dt \\ &= \gamma (x\, G_x\, t_x + y\, G_y\, t_y). \end{aligned} \qquad [2.5.6]$$

The notion of the total phase containing components from both the frequency and phase encoding gradients is often confusing in the presentation of MRI. The key point to realize relates to the gradients: G_x and G_y are both linear gradients in orthogonal directions, and

they both alter the total phase. As seen in actual imaging experiments (Section 2.11), the gradients are applied at different times to conveniently organize the 2D encoding.

To summarize, this section introduces phase encoding as a method to extend 1D encoding to a second dimension and defines the total phase Φ. In a typical 2D encoding scheme, spatial data is "frequency" encoded along x as in Section 2.4 and "phase" encoded along y. Section 2.6 presents the algorithm for this technique, and the consequences of this encoding scheme are played out in the remainder of this chapter.

Section 2.6. Spatial encoding: the foundation of 2D MRI

The presence of both frequency and phase encoding gradients, G_x and G_y, suggests a procedure to encode 2D spatial information. Since 2D encoding often raises many questions, the next three steps in this chapter are briefly outlined before discussing spatial encoding. As suggested above, step 1 explains 2D encoding with two field gradients. This gives a 2D data set, but at present, the MRI data has not been discussed. Therefore, step 2 (Sections 2.7-10) covers the generation and detection of the MRI signal, including the free induction decay and the mechanisms of nuclear relaxation. Step 3 (Sections 2.11-12) then shows the actual techniques currently used to acquire MRI data and reconstruct images.

Two-dimensional spatial encoding is an expansion of the 1D example in Section 2.4 which encodes frequency along x. Now consider the effect of applying a phase encoding gradient G_y for a fixed time t_y prior to frequency encoding. The gradient G_y shifts the phase of the spins with respect to y, and after the phase shift, G_x is applied and the spins are frequency encoded along x. This is the principle underlying 2D spatial encoding: frequency encoding along x and phase encoding along y. In fact, when this two step sequence is repeated with incremental changes in the magnitude of G_y, 2D spatial

information can be mapped "line by line" into a matrix as depicted in Figure 2.6.1. At first glance it appears that the frequency encoding and phase encoding used in Figure 2.6.1 are two different schemes. In fact, it is shown below that by recasting the frequency and phase into the variables k_x and k_y, the two schemes are equivalent ways to encode each of the two dimensions x and y.

The axes in Figure 2.6.1 are labeled k_x and k_y, the two parameters mentioned above. Section 2.8 describes the MRI signal and shows that the data acquired from the present 2D encoding scheme spans a 2D vector space called "k-space". The two orthogonal variables of k-space are k_x and k_y which have the following forms:

$$k_x \equiv \frac{\phi_x}{x} = \gamma G_x t_x \qquad [2.6.1]$$

$$k_y \equiv \frac{\phi_y}{y} = \gamma G_y t_y. \qquad [2.6.2]$$

Equations 2.6.1 and 2.6.2 indicate that k-space data has units of spatial frequency. This may not appear as a striking advantage at present, but as a preview to Section 2.12, the 2D spatial frequency data in k-space is related to the original 2D spatial information by a 2DFT. (The FT relationship may be intuitive at the present since spatial data is mapped into spatial frequency data. The formal discussion appears in Section 2.12.)

As depicted in Figure 2.6.1, the two step process alone does not encode a 2D data set. It encodes only a 1D line in k-space and thus represents only a part of the overall imaging technique. Consider the effect of the first application of G_y at time $t = 1$; it induces a specific phase shift ϕ_y^1 which is a function of y. This corresponds to selecting a specific value of k_y which from the form of Eq. 2.6.2 is independent of y. The information along a line parallel to k_x axis is subsequently obtained by applying the frequency encoding gradient G_x in the time interval $2 < t < 3$. Thus, the 2 step process (phase shift, frequency encode) encodes a single line of k-space data in Figure 2.6.1. The core of 2D MRI lies in

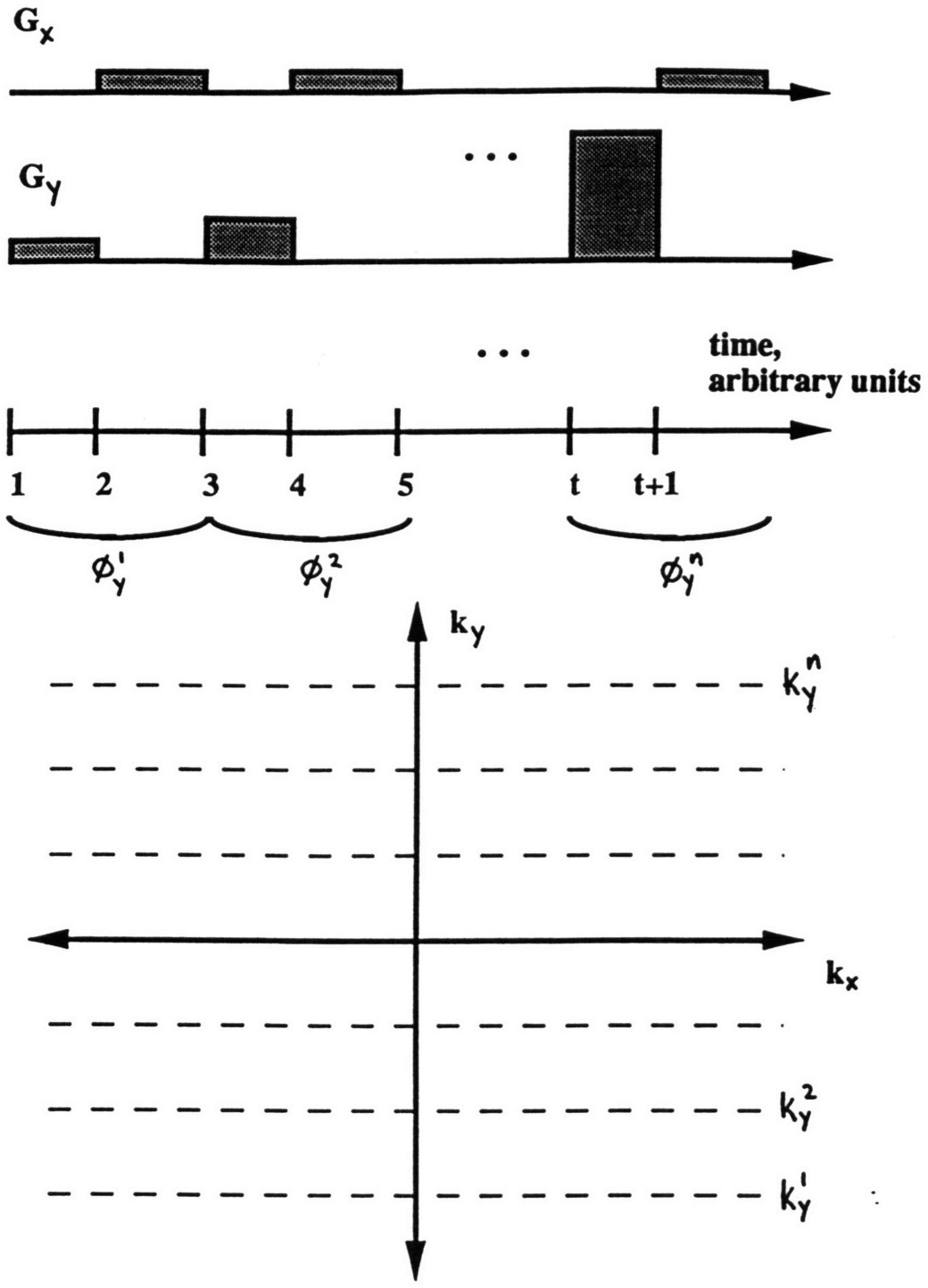

Figure 2.6.1 Simplified timing diagram for spatial encoding. The two step sequence, frequency encoding along x and phase encoding along y, is repeated. Each repetition maps a different line of k-space as described in the text. Actual MRI pulse sequences utilizing spatial encoding appear in Section 2.11.

incrementing the value of G_y: an increase in G_y increases the phase shift along ϕ_y. Thus, when the two step process is repeated, the new set of frequency encoded data is mathematically distinguishable from the prior set because the two data sets have different k_y values. The second application of the two-step process occurs at times $3 < t < 5$ in Figure 2.6.1. The phase encoding begins at $t = 3$ and produces a phase ϕ_y^2. The G_x gradient is then applied at $t = 4$ to frequency encode at the phase ϕ_y^2.

It is important to point out that the sequence of gradients in Figure 2.6.1 is not the timing diagram, or pulse sequence, to produce an image with MR. Instead, it is an illustration of the idea behind spatial encoding which is used in 2DFT MRI. In these techniques the two-step process is repeated n times, and each repetition has a unique k_y. In the second step of the two-step process, n frequency encoded data points are obtained, and the resultant two dimensional encoded spatial region has nxn symmetry.

While this section does not give details about the nature of the MRI signal, it describes a fundamental idea of MRI: encoding spatial information as spatial frequency information. Given that MR is a mechanical tool which converts spatial information into spatial frequency information, the question becomes, "How can MR physics as described in Sections 2.1-5 perform this mechanical function?" To answer this question, the discussion returns to MR physics to elucidate this mechanical mapping.

Section 2.7 The rotating reference frame and the RF field

The previous section concludes with the challenge of describing how MR physics functions as a mapping from spatial information into spatial frequency information. This explanation begins with a review from Section 2.3; the net magnetic moment per unit volume $\overline{M}$ has an equilibrium direction parallel to $\overline{B}_0$ which by convention is the +z direction. In general, $\overline{M}$ is described by two components. The component along z, or M_z,

is named the longitudinal magnetization. The component in the xy plane, or M_{xy}, is named the transverse magnetization. At equilibrium $M_{xy} = 0$ since the vector components of the spins are randomly but evenly oriented through the 360° of the xy plane in Figure 2.3.2.

The MRI signal (called "the signal") is obtained from investigating the properties of $\overline{M}$. $\overline{M}$ is disturbed from its equilibrium position by applying a torque to it. The maximal torque can be applied to $\overline{M}$ if a magnetic field is applied in a plane perpendicular to M_z. By convention, the field inducing the torque is written as the $\overline{B}_1$ field. For the present discussion, it is applied in the x-direction. (See. Fig. 2.7.1.[22]) In order for $\overline{B}_1$ to interact with spins exposed to $\overline{B}_0$, $\overline{B}_1$ is applied at the Larmor frequency. This frequency is in the radiofrequency (RF) range, and thus $\overline{B}_1$ is named the RF field.

When the RF field is applied to the sample, M_z tilts away from the +z axis and begins precessing at the Larmor frequency in the xy plane. As seen in Figure 2.7.1, the motion of $\overline{M}$ is complicated by the fact that the vector has two simultaneous components: it is spinning around the +z axis (precession), and it is tilting toward the xy plane (torque). The motion is simplified by removing its precessional component; this is accomplished by introducing the rotating reference frame denoted by (x', y', z). In the rotating reference frame, the x' and y' axes rotate about the stationary z axis at the Larmor frequency. Therefore, in the rotating reference frame, the motion of $\overline{M}$ is reduced to a rotation about the x' axis. The rotation about the x' axis is measured by the angle θ in Figure 2.7.2.[23] Theta is termed the flip angle and as described below, it is determined by A, the amplitude of the RF pulse and D, the duration of the RF pulse.

RF pulses are an essential component of MRI because they selectively reorient $\overline{M}$. The characteristics of RF pulses follow FT properties, and therefore RF pulses are

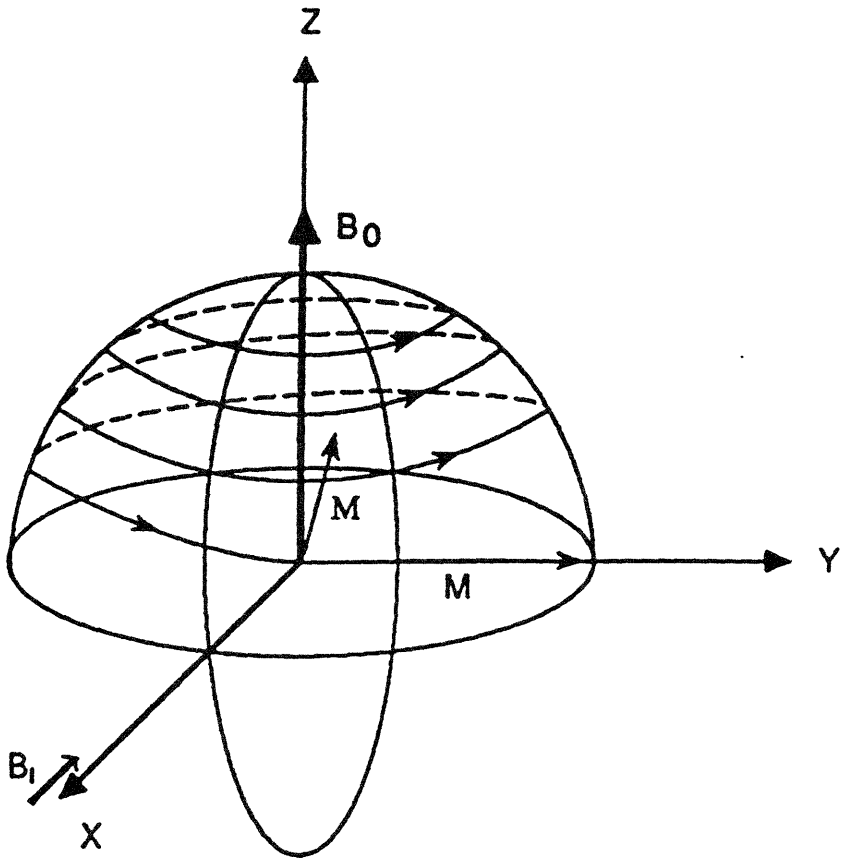

Figure 2.7.1 Motion of the magnetization vector in the laboratory frame.

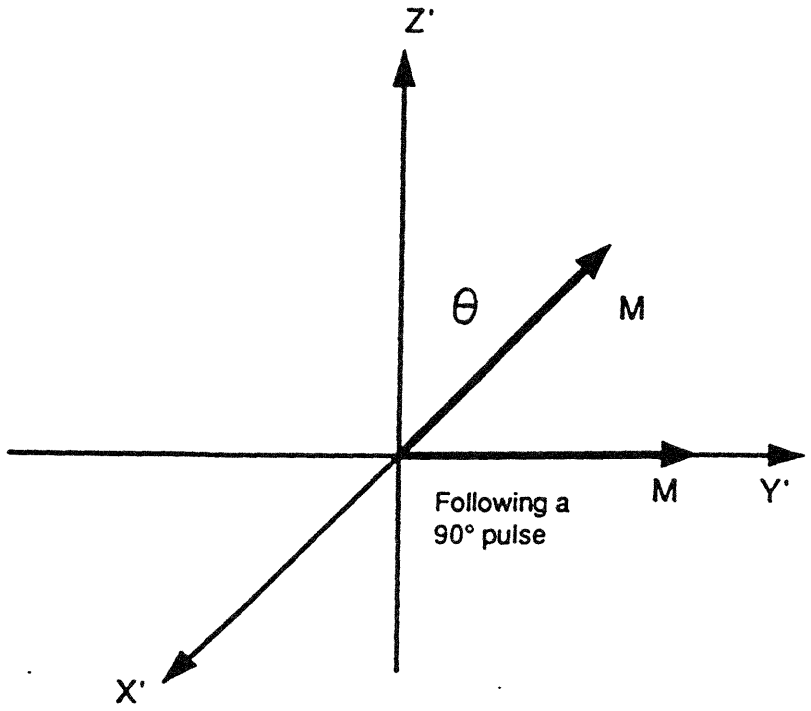

Figure 2.7.2 The flip angle θ.

discussed in terms of FT theorems. The value D, defined as the RF pulse duration, modulates the RF carrier frequency to produce an excitation bandwidth approximately equal to 1/D. In MRI jargon, RF pulses are usually lumped into two categories: "hard (or nonselective) pulses" and "soft (or selective) pulses". Hard pulses have a short duration D and therefore excite a broad range of frequencies. For example, a pulse with D = 1 μsec will excite spins resonating over a frequency bandwidth of 1 MHz centered about the carrier frequency. Thus, these pulses do not select a particular frequency for excitation and are also called nonselective pulses. The opposite is true for soft pulses which have a long duration and therefore selectively excite a narrow frequency range. An example of a soft pulse is D = 1 msec which excites a frequency bandwidth of 1 KHz.

The selective nature of soft pulses makes them useful for MRI. Recall from Section 2.6 that MR mechanically maps 2D spatial data into spatial frequency data. This presents the problem, "How is 2D spatial data selected from a 3D sample such as the human body?" In a method analogous to Section 2.6, phase encoding can be incorporated in the third dimension. However, it is more common to specify a slice with selective pulses. Consider the combination of a selective pulse and a linear gradient oriented along the z axis. The gradient linearly encodes spins with varying frequencies along z, and for the purposes of this discussion, assume a 10 KHz dispersion of resonant frequencies along z. Then, the addition of a soft pulse with D = 1 msec selectively excites spins over 1 KHz within the 10 KHz range. This 1 KHz region of activation forms a slice perpendicular to the z axis which can then be used as 2D sample for imaging. This process is called "slice selection" and is a function of the strength of the linear field gradient and the duration of the pulse D.

The final position of $\overline{M}$ after the RF pulse is a function of A and D. The two excitations most frequently used in MRI have flip angles θ which equal 90° and 180°, and these two pulses are colloquially called "a ninety" and "a one-eighty".

Section 2.8 The MRI signal

The MRI signal results from exciting spins with an RF pulse at the Larmor frequency. Recall from Section 2.7 that irradiation at the Larmor frequency induces an energy absorption. The $\overline{B}_1$ field excites the sample via a RF transmitter antenna at a frequency equal to the precessional frequency of the protons. This absorption displaces the spins from equilibrium and creates an excited system. As the system returns to equilibrium, the signal emitted is proportional to the number of excited spins. The gradients are then applied and the signal contains the spatial frequency information used to fill the k-space matrix in Figure 2.6.1.

First consider the simplest form of the signal called the free induction decay (FID) illustrated in Figure 2.8.1.[24] The sample is placed in the static field $\overline{B}_0$, and a 90° $\overline{B}_1$ pulse is applied perpendicular to the z axis. For simplicity assume the pulse is applied along the x axis. Consider the effect of the RF pulse on the magnetization vector $\overline{M}$. As described in Section 2.7, the 90° pulse rotates the spins to create a maximal M_{xy}, or a combined magnetic moment in the transverse plane. After $\overline{B}_1$ is removed, the individual spins contributing to M_{xy} rotate at their individual Larmor frequencies and the precessing vector $\overline{M}$ induces a voltage in the receiver coil. This voltage is the MRI signal. It is "free" because it occurs in the absence of the $\overline{B}_1$ field and "induced" in the receiver coil by the precessing magnetization vector as it "decays" to equilibrium, hence the name free induction decay. The sinusoidal shape of the FID is explained by the difference between the rotational frequency of the reference frame and the Larmor frequencies of spins. That is, there is precession of the spins in the sample relative to the frame of reference of the detector. As explained below, the signal is proportional to M_{xy}, and the motion of M_{xy} is illustrated in Figure 2.8.2.[25] The decay envelope is caused by a type of nuclear relaxation called T2 as explained in Section 2.10. The FID in Figure 2.8.1 contains a wealth of

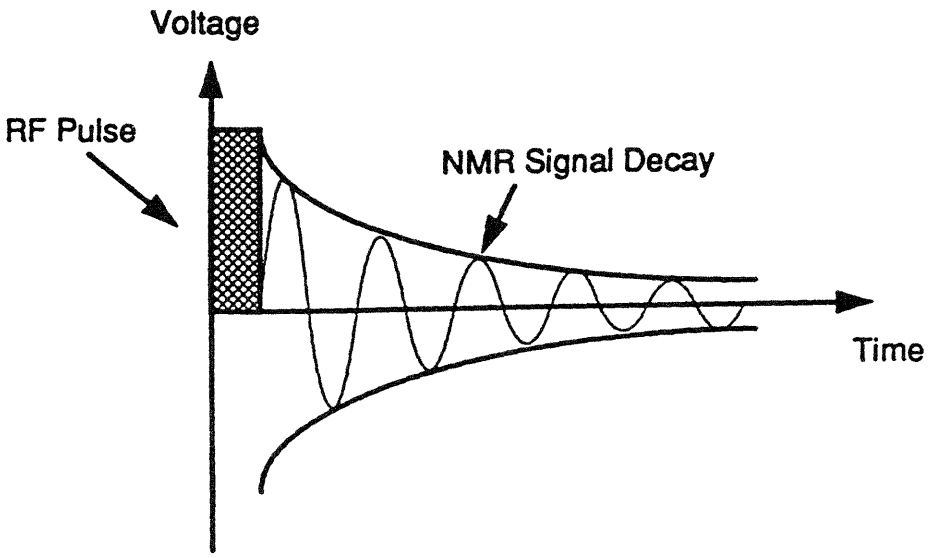

Figure 2.8.1 The free induction decay (FID).

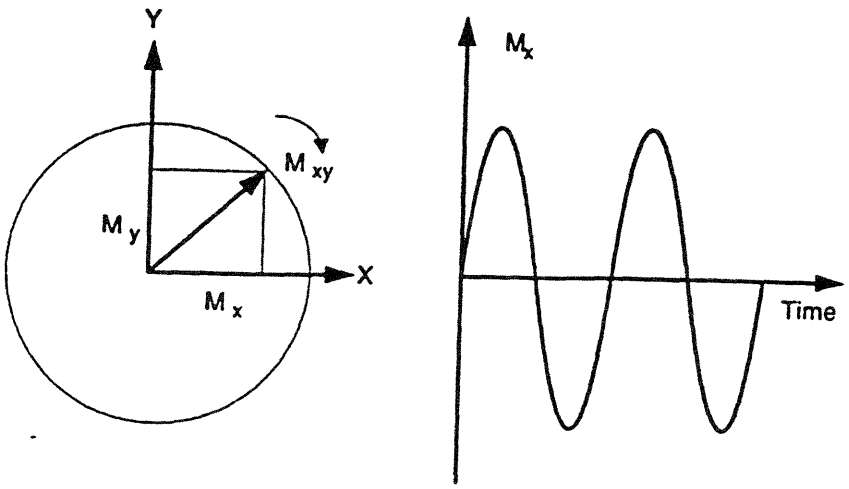

Figure 2.8.2 The induced voltage in a coil aligned along the y axis as a function of time.

information about the sample including amplitude, frequency, and phase data, but since it is acquired in the time domain, this information is difficult to appreciate. However, the time domain FID is related to the frequency domain spectrum by a Fourier transform as shown in Figure 2.8.3. (The Fourier transform is defined in Section 2.12 where its utility for image reconstruction is described.)

As mentioned above the signal is sensed by a receiver antenna coil in the transverse plane. This is a critical point in developing an intuition about the signal: the receiver senses the signal in the transverse plane by the magnetic induction caused by the rotating field. Therefore, the magnitude of the signal is proportional to M_{xy}, and a signal is generated only when $M_{xy} \neq 0$ and the spins maintain phase coherence. Experimentally, it is only possible to obtain M_{xy} information because the voltage measured in the receiver coil is proportional to dB/dt. In the transverse plane dB/dt includes the Larmor frequency which is typically $(2\pi)\,60$ MHz. This factor is not present in dB/dt for longitudinal magnetization, thus the voltage from the time dependent M_{xy} is generally five orders of magnitude greater than that from M_z.

Typical MRI scanners use spatial encoding as described in Section 2.6 for imaging and therefore apply gradients to the sample during the scan time. Since the spins are exposed to gradients, their precessional frequency is determined by their spatial position in the sample. Consequently, the spins accumulate phase incoherence in the transverse plane; that is, the spins have different phases because of their spatial position in the gradient. This is described either physically or mathematically. Physically, the gradient G_x induces the spins to dephase over time, and hence M_{xy} decreases since it is the sum of the spin vectors in the xy plane. The mathematical description of the phase appears in Section 2.5, the spins accumulate a total phase Φ over time given by Eq. 2.5.4.

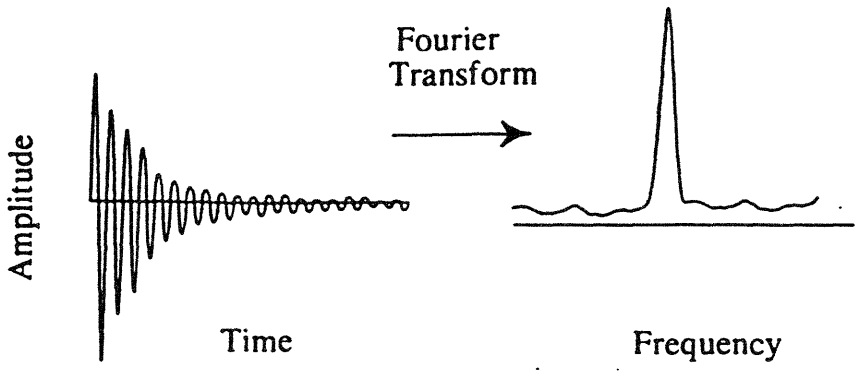

Figure 2.8.3 The FID is a time domain signal which can be converted to the frequency domain by a Fourier transform.

The timing diagram for an imaging technique is thus a combination of RF pulses and gradients. This diagram is called a pulse sequence. The most important pulse sequence is called the spin echo (SE) sequence and is described in Section 2.11. In each of these methods, $M_{xy} \neq 0$ and thus a signal is produced. The true beauty of the signal lies in the simplicity of its mathematical description. To explain the mathematical form of the signal, the discussion returns to the familiar 2D imaging experiment of spatial information in the xy plane. The density of spins in this plane, or the "spin density", has the symbol ρ. The signal depends on the distribution of ρ; hence it is written as $\rho(x,y)$. In this chapter, as in the entire thesis, the 2D spin density $\rho(x,y)$ is assumed to be the unknown.

To understand how ρ is incorporated into the equation for the signal, consider a single spin at the point (x_0,y_0). Regardless of the complexity of the pulse sequence, this spin accumulates a total phase shift $\Phi(t)$ over time, and the contribution of this spin to the signal is weighted by its phase accumulation. If the transverse magnetization M_{xy} is written in complex form $M_{xy}=M_x+iM_y$, then the weighting factor is a complex exponential and the signal from the single spin at (x_0,y_0) is

$$\rho(x_0,y_0)\exp[i\Phi(t)]. \qquad [2.8.1]$$

The total signal is obtained by summing the contributions from all spins over the xy plane. This is mathematically equivalent to integrating Eq. 2.8.1 over x and y, and the form of the signal S then becomes

$$S(t)=\int_{x,y}\rho(x,y)\exp[i\Phi(t)]\,dx\,dy. \qquad [2.8.2]$$

Given the functional form of Eq. 2.8.2, the attenuation of the signal is now introduced. The first form of attenuation is induced by application of a gradient. For example, consider the gradient G_x; it creates a spectrum of Larmor frequencies in the sample. Since the signal

is proportional to M_{xy}, it attenuates as the gradient causes the components of the spins to dephase in the xy plane.

In addition to this first loss of signal, a second attenuation occurs by the process called relaxation. Physically, the signal decays because magnetic field variations not associated with the gradients induce a loss of phase coherence of the individual spins over time. This relaxation is caused by a variety of factors described in Section 2.10. (The natural decay of the FID in Figure 2.8.1 is caused by relaxation since gradients are not applied.) The mathematical consequence of relaxation is that Eq. 2.8.2 is only an approximation of the time evolution of the signal; the complete form is given in Section 2.10 (Eq. 2.10.4) and includes additional terms describing these signal losses.

Section 2.9 Acquisition of the MRI signal and imaging parameters

This section briefly considers the MRI signal acquisition.[26] As the signal emerges from the coil it is amplified by a preamplifier before reaching the receiver. At the preamplifier the signal has a frequency at or near the Larmor frequency which is typically near (2π) 60 MHz, and the first step in the receiver is to remove the carrier frequency of the signal by the process of demodulation.[27] Demodulation is a signal processing technique, but it is physically analogous to moving from the stationary reference frame to the rotating reference frame when observing precessing nuclei. The result of demodulation is a low frequency signal (KHz range), and the second step in the receiver is to remove unwanted noise outside a bandwidth with a low-pass filter. (The bandwidth is chosen by the gradient strength and the field of view as explained below.) The third step in the receiver is detection. The signal is split and passed through a pair a phase-sensitive detectors. The output of these detectors is sensitive to the difference between the measured signal and a reference signal. This method of detection is termed quadrature detection because the two detectors have a phase shift of 90° required to sense the direction of precession.

The two analog signals are then sampled according to the Nyquist criteria.[28] With quadrature detection the sampling rate is effectively doubled and Nyquist criteria becomes

$$t_d = 1/\omega_{max} \qquad [2.9.1]$$

where t_d is the dwell time or time between samples and ω_{max} is the highest frequency allowed by the low pass filter. Typical sampling rates range from 10-50 KHz.

Given the relationship between the bandwidth and the sampling interval, expressions can be derived for the image field of view (FOV) and resolution. This leads naturally to a discussion of signal to noise (SNR) and several of the tradeoffs which are fundamental to developing an intuitive sense of practical MRI.

From the Larmor equation written in terms of the x direction, the bandwidth along x is

$$\Delta\omega_x = \gamma \Delta B = \gamma G_x \Delta x \qquad [2.9.2]$$

where G_x is the gradient along x and Δx is the distance in the x dimension spanned by the gradient. This distance Δx corresponds to the region of body along x which is included in the image, or the FOV along x. This is written FOV_x, and thus Eq. 2.9.2 becomes

$$\Delta\omega_x = \gamma G_x FOV_x \qquad [2.9.3]$$

Substituting Eq. 2.9.1 and solving for the FOV,

$$FOV_x = \frac{1}{t_d \gamma G_x}. \qquad [2.9.4]$$

Equation 2.9.4 is justified intuitively as follows. First consider the effect of t_d on the FOV. Increasing t_d for a fixed number of samples decreases the total bandwidth sampled which will decrease the FOV. The effect of gradient strength is explained by considering the

domain of x spanned by the gradient. A steeper gradient requires a smaller domain along x for the same bandwidth and thus decreases the FOV.

Although there are several ways to define the system resolution, denoted by R, the simplest is to interpret resolution in one dimension as the distance between spatial points sampled. Thus, the resolution is written

$$R_x = \frac{FOV_x}{N_x}, \qquad [2.9.5]$$

where N_x is the number of points along x. Substituting for the FOV,

$$R_x = \frac{1}{\gamma G_x t_d N_x}. \qquad [2.9.6]$$

This equation for resolution is further simplified by noting that the product of the sampling interval in x and the number of points sampled along x is the total time for data collection in the x dimension, written T_x^{col}. Substituting into Eq. 2.9.6,

$$R_x = \frac{1}{\gamma G_x T_x^{col}}. \qquad [2.9.7]$$

At first glance, Eq. 2.9.7 may appear as a prescription for improving (i.e. decreasing) the resolution for MRI. However, there are tradeoffs associated with varying the MRI parameters. Before the discussion of some of these tradeoffs, it is essential to review the factors determining the signal strength and the magnitude of the noise in MRI. The ratio of these values,

$$\frac{\text{signal amplitude}}{\text{noise amplitude}}, \qquad [2.9.8]$$

is called the signal to noise ratio and is abbreviated SNR.

The SNR is fundamental to MRI because it proves to be the limiting factor in almost all imaging techniques. The take-home message is the following: in MRI the signal is fixed by the tissues being imaged, and the signal is relatively weak in comparison with other imaging modalities such as x-ray computed tomography. Why? Recall from Section 2.3 that for protons in a magnetic field, the population difference between the two possible states is minuscule. Specifically, at 27° C and a field strength of 5 kGauss, the ratio N_{up}/N_{down} defined in Section 2.3 equals $1 + 4 \times 10^{-6}$. Now consider the consequences for the signal. If the ratio N_{up}/N_{down} were unity, the net magnetization vector $\overline{M}$ would be zero, and since the signal is proportional to M_{xy}, there would be no signal. ($\overline{M}$ is defined in Section 2.3 as the vector sum of the individual moments, and the relationship between the signal and M_{xy} is discussed in Section 2.8.) Therefore, the excess of protons in the lower energy state generates the MRI signal, and since this excess is slight, the signal is weak and in almost all scenarios limits the imaging technology. As a rough estimate, images with a SNR per pixel of less than 4 have very limited utility, and medically diagnostic MR images require a SNR per pixel of about 20.

With the exception of introducing paramagnetic substances called contrast agents[29] into the sample to increase the signal strength, the most common way to increase the signal is to increase the magnitude of the main field $\overline{B}_0$ since

$$\frac{N_{up}}{N_{down}} = \exp\left[\frac{2\,\mu\,B_0}{k\,T}\right]. \qquad [2.3.5]$$

Thus, increasing the main field strength increases the ratio N_{up}/N_{down} which in turn increases the magnitude of $\overline{M}$. Increasing B_0 corresponds to increasing the Larmor frequency, but since this frequency becomes the carrier frequency which is removed by demodulation, there is no effect on signal processing. However, there are limitations to increasing B_0. For example, the cost of the magnet increases as greater than the square of the field strength. Second, RF power deposition increases as the square of the Larmor

frequency, and therefore increasing the field strength has the potential for adverse physiological effects such as heating.

In a typical clinical protocol, each line of k-space is acquired several times, and the results are averaged to improve the SNR. The number of acquisitions is written as N_{aq}, and the signal is proportional to N_{aq}. With averaging, the signal increases as N_{aq} and the noise, since it is random, increases as $\sqrt{N_{aq}}$. Thus, the SNR is proportional $\sqrt{N_{aq}}$.

The definitions for sampling interval, field of view, resolution, and signal to noise ratio introduce the discussion of MRI tradeoffs. This section does not attempt to compile a complete set of tradeoffs, but instead emphasizes with a few examples that practical MRI is dictated by tradeoffs, and they must be considered in virtually all imaging applications.

Since the goal of all imaging modalities is to measure and resolve spatial information, resolution is essential for any system to have clinical utility. As mentioned earlier, the form of Eq. 2.9.6 may appear as a prescription for decreasing R_x by increasing G_x. However, for a fixed FOV, the product $G_x t_d$ must remain constant by Eq. 2.9.4. (The FOV is bounded from below by the anatomical region being imaged and bounded from above by the product of the number of samples and the resolution.) Thus, for a particular FOV, the only method to decrease R_x is to increase N_x which in turn increases the total scan time. If G_x is increased for a fixed FOV, t_d must be decreased. From the properties of Fourier transforms, the decreased t_d corresponds to a larger bandwidth allowing more noise to be acquired. Thus, the signal is acquired more rapidly at the expense of the SNR.

Now consider decreasing G_x to obtain the smallest bandwidth which increases the SNR. The problem which arises in this case is the natural linewidth of the sample and the

imperfections in the magnet. As G_x is lowered, the inhomogeneities in the main field and the linewidth of the sample become comparable to the gradient strength. Recall from Section 2.4 that the entire concept of spatial encoding is founded on the notion that spins at different spatial locations have distinct Larmor frequencies which are created by the application of a field gradient. When the gradient is not strong enough to maintain spatial encoding in the presence of field inhomogeneities and the sample linewidth, as suggested above by decreasing G_x, the resulting image contains geometric distortions. These distortions are induced by the fact that two spatially distinct regions can have identical Larmor frequencies and thus be mistakenly identified as a single region.

The goal of this section is to briefly describe signal acquisition and introduce the field of view (FOV), resolution (R), signal-to-noise ratio (SNR), and some of the tradeoffs between these parameters. These are the parameters which are most often discussed in the MRI literature, and they are described here to assist in the discussion of imaging with the PERL encoding field.

Section 2.10 Relaxation

Section 2.8 describes the signal (Eq. 2.8.2) as an integral of the spin density weighted by a complex exponential including a phase term. This section describes the two relaxation properties of spins in a field. They are named T1 and T2, and as emphasized in this section, they are properties of spin-lattice and spin-spin systems respectively.

First consider the field observed by a spin which is created by its neighboring spins. This "local" field fluctuates in time due to random thermal motion. The distribution of the field at any given instant over the ensemble of spins in the system is statistically identical to the distribution of the individual spin over time. The decay process from this "spin-spin" interactions is exponential, and the relaxation of $\overline{M}$ is called T2 relaxation or T2

decay. Defining M_0 as the transverse magnetization at time $t=0$, the loss of phase coherence from T2 decay is:

$$M_{xy} = M_0 \exp[-t/T2]. \qquad [2.10.1]$$

The phase difference induced by T2 decay is primarily due to the low frequency or slow components of the local field.[30] Since the signal is proportional to M_{xy}, the form of the signal accounting for T2 relaxation includes the term $\exp[-t/T2]$.

T2 decay is related to the molecular structure of the excited sample. The present discussion approaches this relationship informally; more formal treatments appear elsewhere.[31] To get a feel for T2 decay, first consider very mobile small molecules in liquids. Samples of this nature have long T2s because the phase accumulations from intrinsic inhomogeneities in the sample are averaged out by fast, rapidly changing motions. However, as the molecular size of the sample increases, the motions become less mobile, and phase dispersion builds more rapidly. For large, nonmoving structures, the inhomogeneities are more stationary, and very short T2 values are observed.

In addition to the intrinsic dephasing described above, inhomogeneities in B_0 arising from imperfections in the magnet also dephase the transverse signal. This is not T2 decay because it is not intrinsic to the system; it also includes extrinsic factors and is therefore called T2*. Since the dephasing rates from intrinsic and extrinsic factors are additive, the relationship between them is

$$\frac{1}{T2^*} = \frac{1}{T2} + \gamma \pi \Delta B_0, \qquad [2.10.2]$$

where ΔB_0 represents the field inhomogeneities across a single voxel in the image. In practice, the FID form of the signal decays as $\exp[-t/T2^*]$, but there are pulse sequences,

in particular the spin echo sequence described in Section 2.11, for which the signal follows pure T2 decay.

While transverse magnetization is lost rapidly (a typical T2 value for white matter in the brain is 90 msec), the return of $\overline{M}$ to its equilibrium position is a longer process representing the loss of energy of individual spins to their environment. This exchange of energy is termed "spin lattice" relaxation, and the relaxation time constant is named T1. The regrowth of the magnetization to the equilibrium position is governed by

$$M_z = M_0(1 - \exp[-t/T1]) \qquad [2.10.3]$$

where M_0 now represents the longitudinal magnetization at time $t = 0$.

T1 relaxation is characteristic for specific tissue types and pathologic states.[32] It depends on the interaction of excited spins and the molecular lattice surrounding the spins. The quantum approach to T1 relaxation is described elsewhere.[33] The idea behind these discussions is that T1 measures the conversion rate between antiparallel and parallel spins discussed in Section 2.3. A sample containing a lattice which can easily accept energy of these transitions (at the Larmor frequency) will have a short T1. Otherwise, a longer time is required for the transition between energy states and the T1 is increased.

Considering T1 from a simpler perspective,[34] it depends on the tumbling frequency of the molecules in the sample. If the tumbling frequency matches the Larmor frequency, energy is rapidly exchanged and T1 is short. Following this argument, the T1 of solids is long; another way to describe the same phenomenon is to say solids have limited energy coupling to their lattice. The story for liquids is less straightforward. A mobile liquid has more tumbling than a solid, but the requirement for rapid exchange of energy is tumbling at the Larmor frequency. If the tumbling spans a large domain of frequencies, little energy

coupling between the lattice and the spins occurs since only a small number of molecules actually tumble at the Larmor frequency. Hence the T1 is long. Now consider a liquid containing biomacromolecules, or large biological molecules. This addition to the liquid tends to decrease the overall tumbling frequency and increase the number of molecules tumbling at the Larmor frequency. This enhances a more rapid release of energy to the lattice, and T1 decreases. For example, T1 values for soft tissues range from 0.1 to 1.0 seconds, whereas values for aqueous solutions (e.g. CSF) and water vary between 1 and 4 seconds. It is also critical to note that in general the number of spin-lattice interactions are a function of frequency, T1 values increase as the magnitude of the main field increases.

Representative values for T1 and T2 in various tissues appear in the references.[35] It is important to realize that the difference between T1, T2, and T2* values in tissues provides the contrast in MRI. (The other significant contributors are the proton spin density and blood flow.) Incorporating T1 and T2 relaxation into the expression for signal and assuming a 90° flip angle, Eq. 2.8.2 becomes

$$S(t) = \int_{x,y} \rho(x,y) \exp[i\Phi(t)] \exp[-t/T2] (1- \exp[-t/T1]) \, dx \, dy. \qquad [2.10.4]$$

This section introduces the relaxation terms T1 and T2 and concludes with Eq. 2.10.4, the expression for the signal incorporating these terms. Although relaxation is fundamental to understanding MRI, the T1 and T2 terms are often omitted in the mathematics; this is the case for the PERL technology. However, in practice T2 values are critical because they limit the time for signal acquisition and determine the tissue contrast.

Section 2.11 The spin echo (SE) pulse sequence for MRI

Present MRI uses two major groups of pulse sequences: gradient echo and spin echo. Gradient echo (GRE) sequences are covered in Chapter 3, and the present

discussion focuses on the spin echo (SE) sequence which is by far the most used sequence for clinical imaging. (Additional pulse sequences such as inversion recovery can be found in the references.[36])

The description of the SE sequence in this section is modified from the Bushberg text[37] and course notes from MIT.[38] The sequence consists of a series of 90° pulses separated by a time called the time of repetition (TR). Regardless of the imaging sequence, the 90° pulse excites the spins by placing the longitudinal magnetization in the transverse plane. In SE sequences additional 90° pulses are applied after each TR, and since TR is typically not long enough for complete longitudinal (T1) recovery, the transverse magnetization obtained from the later excitation pulses is decreased. For excitation pulses repeated every TR where TR < T1, the spin system reaches an equilibrium in which the longitudinal magnetization is less than maximal. This is called "saturation"; that is, spins exposed to multiple 90° pulses reach a steady state,[39] and tissues in the sample with short T1 values will produce more signal since they are less saturated.

M_{xy}, and hence the signal, decays by both T2 and T2* relaxation. However, in the SE sequence a 180° pulse is applied after the time called TE/2. During the time interval TE/2, each spin precesses through some angle accumulating a phase shift due to constant field inhomogeneities (T2* dephasing). The 180° pulse inverts the phase of each spin. After an additional time TE/2, the same phase shift which accumulated in the original TE/2 is produced, and because the 180° pulse reverses the initial phase shift, the total phase due to the constant field inhomogeneities is zero at time TE. This rephasing produces a strong signal called a spin echo centered at the time TE as depicted in the rotating reference frame in Figure 2.11.1. There are many physical analogies used to describe the spin echo; one of the best appears in the references.[40]

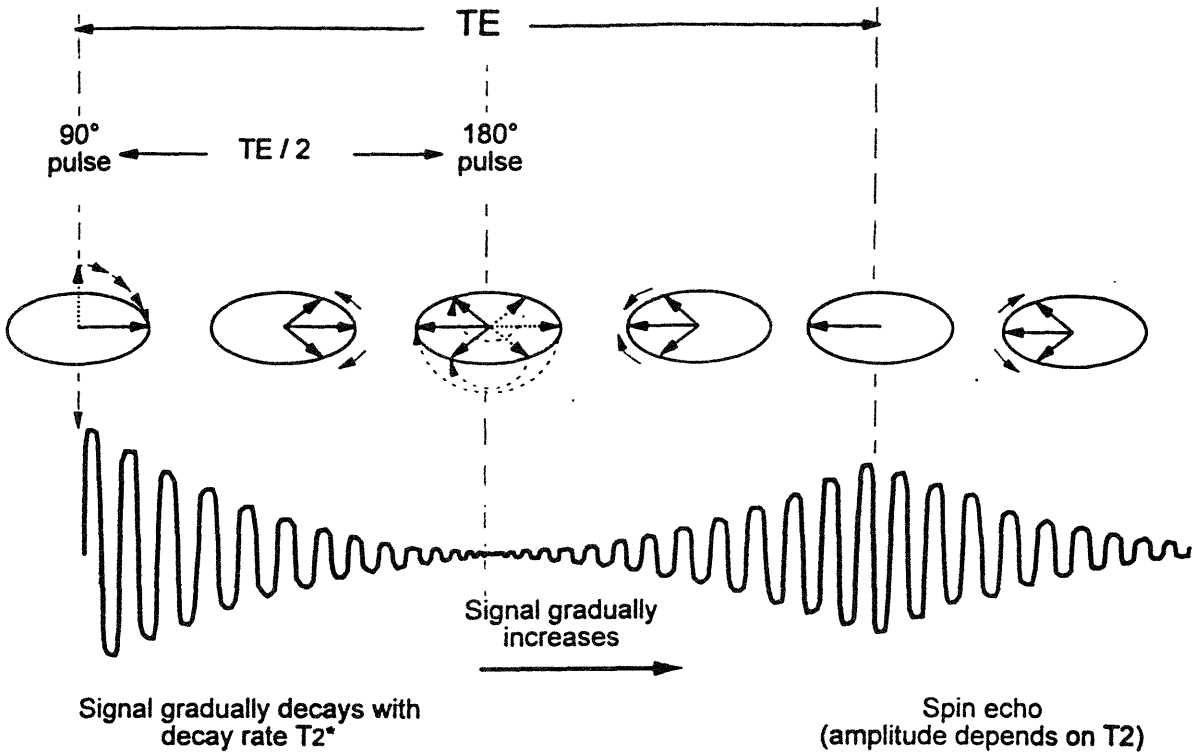

Figure 2.11.1 Formation of the spin echo. See text for details.

Given this discussion on the formation of the spin echo, the generic SE pulse sequence is illustrated in Figure 2.11.2. Assume in this figure that the slice selection gradient as described in Section 2.7 is performed in the z-direction, frequency encoding performed along x, and phase encoding is performed on y. The stacked appearance of the phase encoding gradient is commonly used to indicate that this timing diagram is repeated for multiple excitations, and for each excitation the magnitude of the phase encoding gradient is incremented. This is exactly the process described in Section 2.6; G_y is incremented to obtain a new horizontal line of k-space, and this line of data is obtained with the frequency encoding gradient G_x.

The features of 2DFT SE imaging are captured in Figure 2.11.3 which includes the basic features of the SE sequence in Figure 2.11.2. The eight key steps of the process outlined below correspond to the numbers which appear in Figure 2.11.3.

1. As described in Section 2.7, a slice is selected by applying a 90° RF pulse tuned to a narrow frequency bandwidth in the presence of a slice selective gradient. The 90° pulse also performs its duty of converting longitudinal magnetization into transverse magnetization. The negative lobe which appears in the slice selective gradient serves to reverse the dephasing accumulated during the excitation and is called a compensatory or rephasing gradient.
2. Phase encoding is performed as described in Section 2.5. One phase encode step is applied per excitation, and the difference in these steps correspond to incremental values of k_y.
3. The 180° pulse is applied at the time TE/2 to invert the phase of individual spins so that phase coherence from constant field inhomogeneities will be reestablished at time TE in the transverse plane. For this reason the 180° pulse is sometimes called the refocusing pulse.

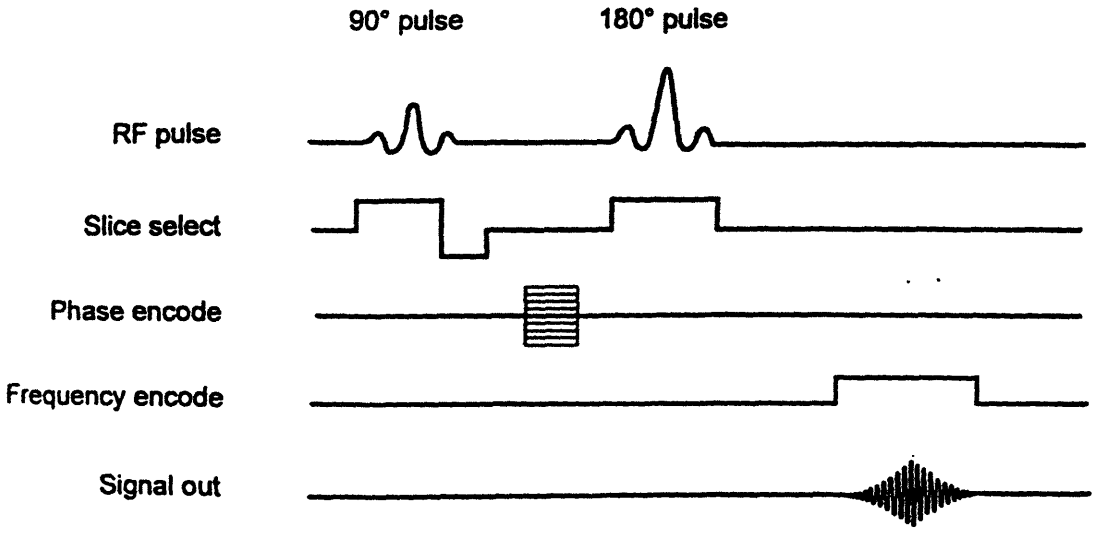

Figure 2.11.2 Generic spin echo pulse sequence illustrating the timing of the RF pulses, the gradient applications, and the signal.

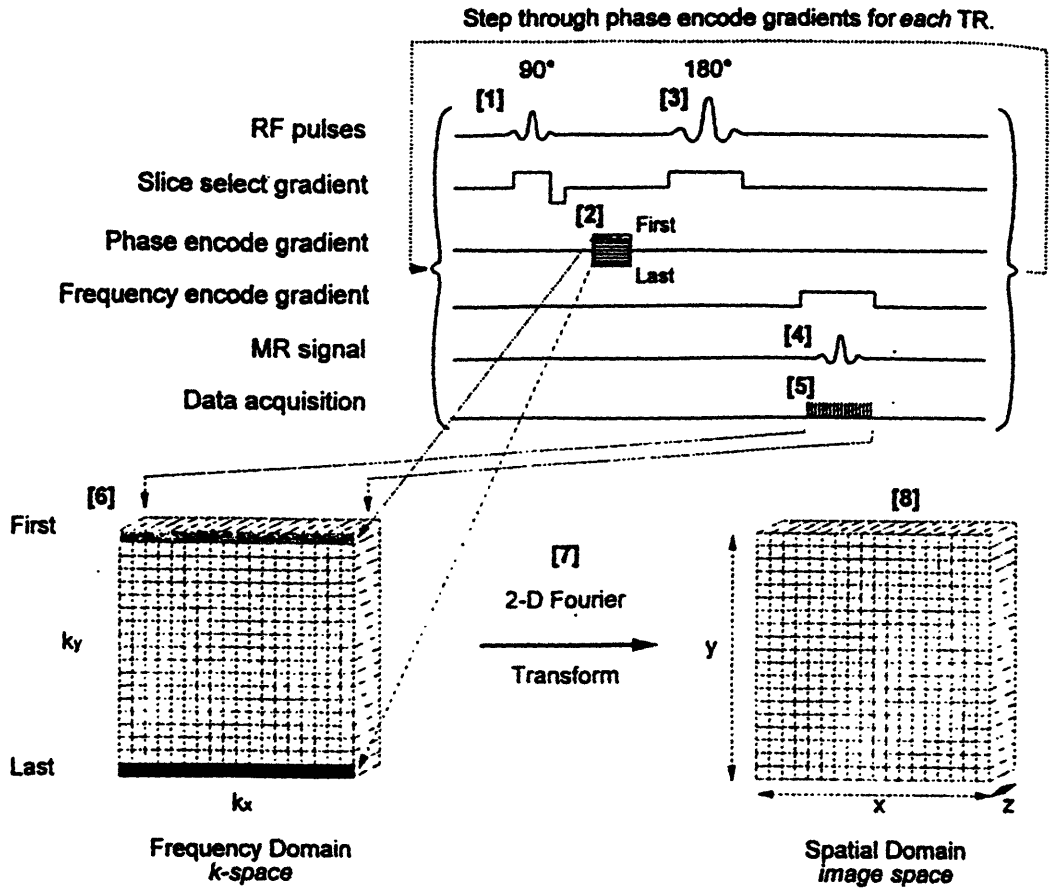

Figure 2.11.3 Graphical representation of the spin echo pulse sequence. See text for details.

4. The echo created by the two RF pulses forms at time TE. In the time interval in which data is acquired, the frequency encode or "readout" gradient is applied while the lines of k-space are read as described in Section 2.6.

5. During application of the frequency encode gradient, the composite multifrequency signal is sampled with an analog-to-digital converter. As mentioned above, each excitation produces a line of k-space data.

6. As discussed in the following section, the k-space matrix is a 2D mapping of the spatial frequency information in the sample. This should come as no surprise: Section 2.4 described MR as a mapping between spatial information and spatial frequency information, Eq. 2.4.3 gives the 1D relationship between spatial coordinates and spatial frequency coordinates along x, and Section 2.5 emphasizes that the two encoding gradients, frequency and phase, produce equivalent phase shifts in their respective dimensions. The origin of k-space is the zero frequency or DC component, and the other spatial frequency components appear at their respective coordinates (k_x,k_y).

7. Without introducing the mathematical detail, spatial information and spatial frequency information are Fourier transform pairs. Thus, the spatial information is decoded from the k-space information by a 2DFT, or a 1DFT along each of the image dimensions: x and y. The mathematics are described in Section 2.12, but the intuitive picture cannot be overemphasized. MR performs a mechanical FT on spatial information to convert it to spatial frequency information, and the spatial information is therefore reconstructed by FT mathematics.

8. The resulting image represents several characteristics of the sample including but not restricted to the spin density and the relaxation times. There are a large number of variations on the SE sequence which are designed to emphasize particular characteristics of the spin sample. For example, clinical images which emphasizes differences in either T1 or T2 between tissues are called T1 or T2 weighted images.[41]

The SE pulse sequence gives excellent tissue contrast and can easily be modified for specific clinical imaging applications. It is thus the sequence of choice for most clinical scanners. However, the drawback of the SE sequence is its long scan times. From the SE sequence, the total scan time is estimated as

$$T_{total} = (TR)(N_{aq})(N_{pe}) \qquad [2.11.1]$$

where N_{pe} is the number of phase encodes and N_{aq} is the number of acquisitions per line of k-space obtained for averaging which improves the image signal-to-noise ratio (SNR). As discussed in Section 3.1, typical values for a generic SE sequence are $(TR) = 0.5$ sec, $(N_{aq}) = 2$, and $(N_{pe}) = 256$ leading to a scan time greater than four minutes for a single slice. Since clinical applications generally require multiples slices, the SE sequences requires modifications discussed in Chapter 3 to reduce the scan time.

Section 2.12 The 2DFT and image reconstruction

Section 2.11 concludes with a description of the SE sequence and a calculation of the total scan time per slice. In this description and throughout this chapter MRI is introduced as a mechanical Fourier transform, and this principle is again emphasized in this section. Recall that with MRI spatial information encoded by field gradients is converted to spatial frequency data in k-space. The final piece of the story is the relationship between the 2D data set and the unknown 2D spin density $\rho(x,y)$. That is, a method is required to decode the k-space data. In imaging, the process of decoding is termed reconstruction, and as suggested by the name of this imaging technique, 2D Fourier imaging, the image reconstruction uses FT mathematics. To begin, the definition of the 2DFT of the spin density is given as

$$2DFT[\rho(x,y)] \equiv F(f_x,f_y) = \int_{x,y} \rho(x,y) \exp[i(f_x x + f_y y)]\, dx\, dy \qquad [2.12.1]$$

where the integral sign represents a 2D integration over all values of x and y and the terms f_x and f_y are the spatial frequencies in x and y.

Equation 2.12.1 resembles Eq. 2.8.2, the expression for the signal in terms of the total phase Φ, and the remainder of this section shows that these equations are identical if f_x and f_y are identical to k_x and k_y respectively. The derivation of the relationship between the k-space data and the spin density begins with Eq. 2.8.2, the form of the signal in which the T1 and T2 relaxation terms are omitted. Writing the signal as a function of the k-space parameters,

$$S(k_x,k_y) = \int_{x,y} \rho(x,y)\exp[i\,\Phi]\,dx\,dy. \qquad [2.12.2]$$

Substituting for the total phase Φ from Eq. 2.5.6,

$$S(k_x,k_y) = \int_{x,y} \rho(x,y)\exp\left[i\,\gamma(x\,G_x\,t_x + y\,G_y\,t_y)\right]\,dx\,dy, \qquad [2.12.3]$$

and this form begins to look like the 2DFT of the spin density in Eq. 2.12.1. In fact, the two equations are identical if $f_x = \gamma G_x t_x$ and $f_y = \gamma G_y t_y$. However, these are precisely the definitions for k_x and k_y in Eqs. 2.6.1-2, and the expression for the signal becomes

$$S(k_x,k_y) = \int_{x,y} \rho(x,y)\exp[i\,(k_x x + k_y y]\,dx\,dy. \qquad [2.12.4]$$

Equation 2.12.4 is the mathematical proof of the intuitive notion that MR is a mechanical Fourier transform, and it gives the prescription for reconstructing the spin density from the k-space data. This expression is also fundamental to the original work in this thesis. The FT relationship between the signal and the spin density is a direct consequence of the linear encoding gradient. If the gradient is not linear, the total phase Φ calculated from Eqs. 2.5.1 does not have the form in Eq. 2.5.6, and the expression for the signal does not match

the definition of the 2DFT. This is precisely the case when the PERL field is used for spatial encoding: the signal is no longer related to the spin density by a 2DFT. One main objective of this thesis is to define the relationship which does exist between the signal and the spin density and use this relationship to develop a reconstruction algorithm for PERL field encoding.

Section 2.13 Conclusions

This chapter begins with MR physics to introduce MRI. The approach in this text leads quickly to simple MR experiments and a description of k-space. After a description of the MRI signal, special emphasis is given to the spin echo pulse sequence for two reasons. First, it is the most important sequence for clinical imaging, and second, the PERL imaging sequences acquire spin echo data. Emphasis is also placed on the role of Fourier transform mathematics in MRI, particularly in the description of the reconstruction. The significance of this formalism becomes apparent in Chapters 5 and 6. When the PERL field is used for encoding, the spin density and the data vector space are no longer related by a 2DFT. In fact, the relationship is Fourier along one dimension, but the second dimension requires the development of a new transform called the PERL transform. Thus, understanding the rapid PERL sequences requires an intuition about Fourier mathematics. Chapter 3 continues to review MRI but focuses on current pulse sequences for rapid imaging, all of which are based on Fourier mathematics.

Chapter 2 References

[1] R Schmacher, *Introduction to Magnetic Resonance*, W.A. Benjamin, Inc., 1970.
[2] PG Morris, *Nuclear Magnetic Resonance Imaging in Medicine and Biology*, Oxford University Press, New York. 1990.
[3] S Webb (ed.) *The physics of medical imaging*, IOP Publishing Ltd. Bristol, England, 1990.
[4] KK Shung, MB Smith, and BMW Tsui, *Principles of Medical Imaging*. Academic Press, San Diego, 1992.
[5] JT Bushberg et al. *The Essential Physics of Medical Imaging*. Williams and Wilkins, Baltimore, 1994.
[6] S Patz. Basic physics of nuclear magnetic resonance. Cardiovascular Interventional Radiology 8:225, 1986.
[7] Pykett IL et at. Radiology 143:157, 1982
[8] Pykett IL et at. Current Problems in Cancer 7:3, 1982
[9] Fullerton GD. Magnetic Resonance Imaging 1:39, 1982
[10] C von Jako. MIT Master of Science Thesis, 1993
[11] Halliday D and Resnick R. *Fundamentals of Physics*, 2nd Edition Extended, John Wiley and Sons, New York. 1981.
[12] PG Morris, *Nuclear Magnetic Resonance Imaging in Medicine and Biology*, Oxford University Press, New York. 1990. (Ch. 2)
[13] C von Jako. MIT Master of Science Thesis, 1993. (p. 22)
[14] C von Jako. MIT Master of Science Thesis, 1993. (p. 19)
[15] W Bradley and H Tosteson. *Nuclear magnetic resonance imaging in medicine*. Igaku-Shoin, 1982.
[16] GE Pake. Fundamentals of nuclear magnetic resonance absorption. American Journal of Physics 18:428, 1950.
[17] GE Pake. Fundamentals of nuclear magnetic resonance absorption. American Journal of Physics 18:428, 1950.
[18] Rabi et al. Phys Rev 53:318, 1938.
[19] Bloch et al. Physical Review 69:127, 1946.
[20] Purcell et al. Physical Review 69: 37, 1946.
[21] PC Lauterbur. Nature 242:190, 1973.
[22] KK Shung, MB Smith, and BMW Tsui, *Principles of Medical Imaging*. Academic Press, San Diego, 1992.
[23] KK Shung, MB Smith, and BMW Tsui, *Principles of Medical Imaging*. Academic Press, San Diego, 1992.
[24] KK Shung, MB Smith, and BMW Tsui, *Principles of Medical Imaging*. Academic Press, San Diego, 1992.
[25] KK Shung, MB Smith, and BMW Tsui. *Principles of Medical Imaging*. Academic Press, San Diego, 1992.
[26] B Rosen, MIT 22.561 course notes, 1994.
[27] AV Oppenheim and AS Wilksy. *Signals and Systems*. Prentice-Halls Inc, 1983..
[28] WM Seibert. *Circuits, Signals, and Systems*. The MIT PRess, Cambridge, MA 1989.
[29] AD Watson et al. Contrast agents in nagnetic resonance imaging. In *Margnetic Resonance Imaging Vol 1*. (DD Stark, ed.) Mosby Year Book, St.Louis, 1992.
[30] S Patz. Basic physics of nuclear magnetic resonance. Cardiovascular Interventional Radiology 8:225, 1986.
[31] N Bloembergen et al. Relaxation effects in nuclear magnetic resonance absorption. Physical Review 73:679, 1948.
[32] R Damadian. Tumor detection by nuclear magnetic resonance. Science 171:1151, 1971.

[33] N Bloembergen et al. Relaxation effects in nuclear magnetic resonance absorption. Physical Review 73:679, 1948.
[34] JT Bushberg et al. *The Essential Physics of Medical Imaging*. Williams and Wilkins, Baltimore, 1994.
[35] JT Bushberg et al. *The Essential Physics of Medical Imaging*. Williams and Wilkins, Baltimore, 1994.
[36] WR Hendee and R Ritenour. *Medical Imaging Physics*, 3rd Edition. Mosby Year Book, St.Louis, 1992.
[37] JT Bushberg et al. *The Essential Physics of Medical Imaging*. Williams and Wilkins, Baltimore, 1994.
[38] B Rosen. MIT course 22.561, 1994.
[39] S Patz. Steady state free precession: an overview of basic concepts and applications. In *Advances in Magnetic Resonance Imaging, Vol.1*. (E Feig, ed.) Ablex Publishing, 1989.
[40] HH Schild. *MRI made easy...well almost*. Berlex Laboratories, 1992.
[41] RB Lufkin. *The MRI manual*. Year Book Publishers, 1990.

Chapter 3. Introduction to Rapid MRI.

Section 3.1 Introduction

Since the development of MRI there has been significant motivation for increasing its speed.[1,2] The initial impetus began from clinicians who desired shorter scan times to improve patient comfort and patient throughput. However, there are additional technical merits associated with increasing the speed of MRI. These merits include reducing image artifacts and expanding the range of MRI applications. As noted in Chapter 2, the spin echo (SE) sequence is the most common MRI technique used for clinical imaging. The total scan time for the SE sequence is given by

$$T_{total} = (TR)(N_{aq})(N_{pe})/n \qquad [3.1.1]$$

where TR is the time between excitations, N_{pe} is the number of phase encodes, N_{aq} is the number of acquisitions per line of k-space obtained for averaging, and n is the number of phase encode steps per excitation. For SE imaging, n = 1; that is, the number of excitations equals the number of k-space lines. In this case, Eq. 3.1.1 reduces to Eq. 2.11.1. To repeat the example time calculation in Section 2.11, in a SE sequence for a 256 x 256 image matrix and 2 averages per phase encode step with a TR of 500 msec, the image time per slice is 0.5 x 2 x 256 = 256 sec or 4.27 minutes. One simple way to reduce this time is to reduce the number of phase encode steps by eliminating the high spatial frequencies in this direction, i.e. zero filling the image matrix for these frequencies.

As second technique in common practice to decrease T_{total} per slice is to use multiple slice acquisition techniques in which a volume of tissue representing several slices is excited during TR to optimally utilize the waiting time for longitudinal recovery. This technique involves the excitation of one slice and the readout of the spin echo. After

this acquisition, a second slice is selectively excited while the longitudinal relaxation from the first slice recovers.

The third standard technique to reduce imaging time is called "Half-Fourier imaging". It is based on the FT property of conjugate symmetry which (in one-dimension) states that if $\rho(x)$ and $S(k_x)$ are FT pairs and $\rho(x)$ is a real function, then $S(k_x) = S^*(-k_x)$ where the asterisk "*" represents complex conjugate. Consequently, since all images are real (i.e. $Im[\rho(x,y)] = 0$), the MRI signals at $\pm k_{x,y}$ are in theory complex conjugates of one another, and it is possible to use only one-half of k-space data to reconstruct a complete image.

In practice, k-space data contains some distortions from patient motion, magnetic field inhomogeneities, imperfect timing, and nonuniform RF penetration. Thus, slightly greater than one-half of k-space is acquired; the additional information is used to correct for errors in phase. The result is a time reduction approaching two-fold for any pulse sequence which acquires data in k-space with no loss in contrast. However, the tradeoff of this technique is a SNR reduction because of the decreased number of excitations of the sample volume.

Despite these improvements, spin echo imaging is limited because even with these three techniques, the required imaging time exceeds the duration of several events in human physiology. These include respiration, pulsation, and peristalsis, all of which challenge technology to develop rapid imaging schemes. Each of the following three sections of this chapter outlines a scheme: 1) the Carr-Purcell-Meiboom-Gill (CPMG) sequence with imaging times per slice of less than one minute; 2) Gradient-Echo Imaging (GRE) with imaging times less than half a minute; and 3) Echo-planar imaging (EPI) which regularly produces images in less than 1 second. Each section briefly describes the

principle underlying the technique and its associated tradeoffs, estimates the imaging speed, and provides the corporate names of the sequences with appropriate references.

Section 3.2. The Carr-Purcell-Meiboom-Gill (CPMG) sequence

The CPMG sequence[3,4] illustrated in Figure 3.2.1 is a straightforward modification of the spin-echo sequence which decreases the total scan time by increasing n, the number of phase encodes per excitation, in Eq. 3.1.1. The notion behind the CPMG sequence is that multiple spin echoes are collected after the 90° pulse by refocusing the spins with a series of 180° pulses. The number of echoes acquired per TR equals the number of 180° pulses applied per RF excitation.

The total scan time for the CPMG sequence is given by Eq. 3.1.1. As discussed below, n is limited by the tradeoffs of using multiple 180° pulses per excitation. Typical values of n are 2-4, resulting in total scan times decreased by this factor. However, there are even more rapid CPMG sequences such as RARE (Rapid Acquisition with Relaxation Enhancement)[5,6,7] and Fast Spin Echo[8] techniques for which n can be as large as 64.

The advantage in speed in the CPMG sequence comes with three tradeoffs. First, each echo acquired per excitation has a different T2 weighting, and consequently, the T2 contrast is not definitive. Second, multiple 180° pulses in the CPMG sequence induce steady state effects because the repetition time of the 180° pulses is less than T2.[9] The third tradeoff is common to all rapid imaging techniques which acquire multiple echoes within a short TR. In these techniques, the sampling rate during the readout gradient is increased. This corresponds to a larger bandwidth, and more noise is acquired with the signal.

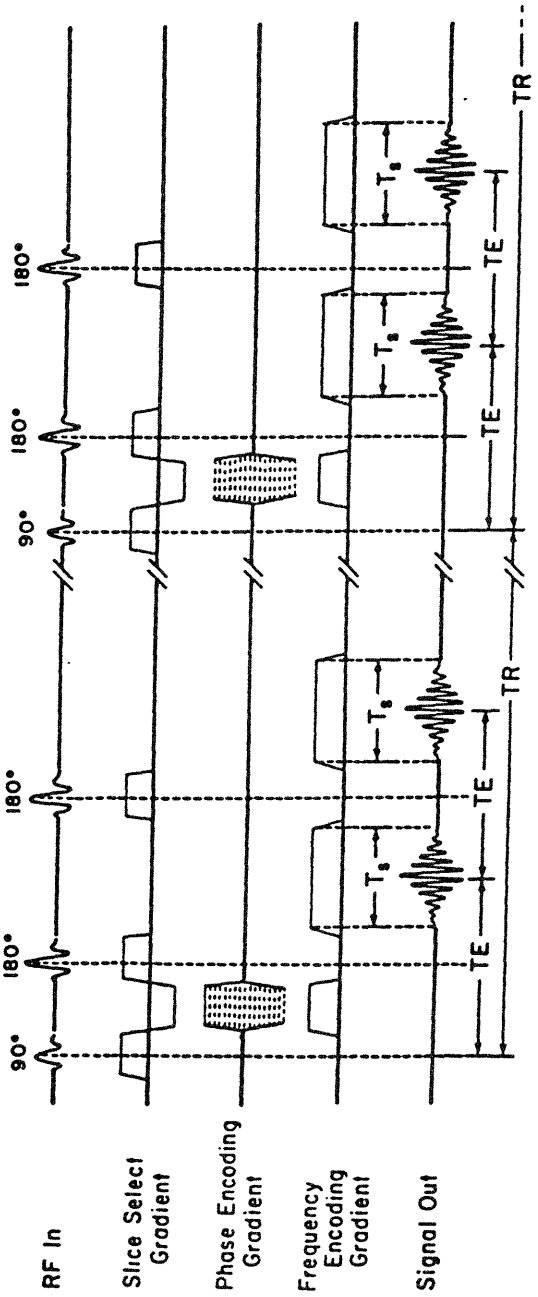

Figure 3.2.1 The Carr-Purcell-Meiboom-Gill (CPMG) pulse sequence drawn with two echoes per excitation.

Section 3.3 Gradient-Echo Imaging (GRE)

Gradient echo imaging[10] (GRE) was the first rapid scanning technique with adequate SNR to study dynamic processes. Examples of GRE sequences include FLASH (Fast Low-Angle SHot imaging), GRASS (Gradient Recalled Acquisition in the Steady State), and SSFP (Steady-State Free Precession).[11,12,13] Early applications of GRE included contrast agent perfusion, and these applications ushered in MRI applications yielding noninvasive insights in areas formerly believed inaccessible with MRI.

The fundamental difference between gradient-echo imaging and spin-echo imaging is instead of using a 180° pulses to obtain an echo, the echo is formed by reversing the direction of the frequency encoding gradient. As in SE imaging, the basic GRE pulse sequence must be repeated a large number of times (e.g. 256) with each RF excitation corresponding to a phase encoding step. However, GRE has a speed advantage over SE sequences since reversing the gradient is accomplished more quickly than a frequency selective 180° pulse. Typical values for TR with GRE sequences are 20-100 msec. The pulse sequence for gradient-echo imaging is illustrated in Figure 3.3.1, and the first important point to note is the initial trough in the frequency encoding gradient during the initial time TE/2.

During the trough in this time interval, the transverse magnetization dephases, but the subsequent plateau in which the gradient is reversed induces a rephasing which forms an echo at time TE. The general idea of oscillations of the amplitude in the gradient coils is colloquially termed "field switching" and plays an important role in the present GRE sequences, echo-planar imaging (EPI) sequences, and imaging with the PERL technology developed in this thesis.

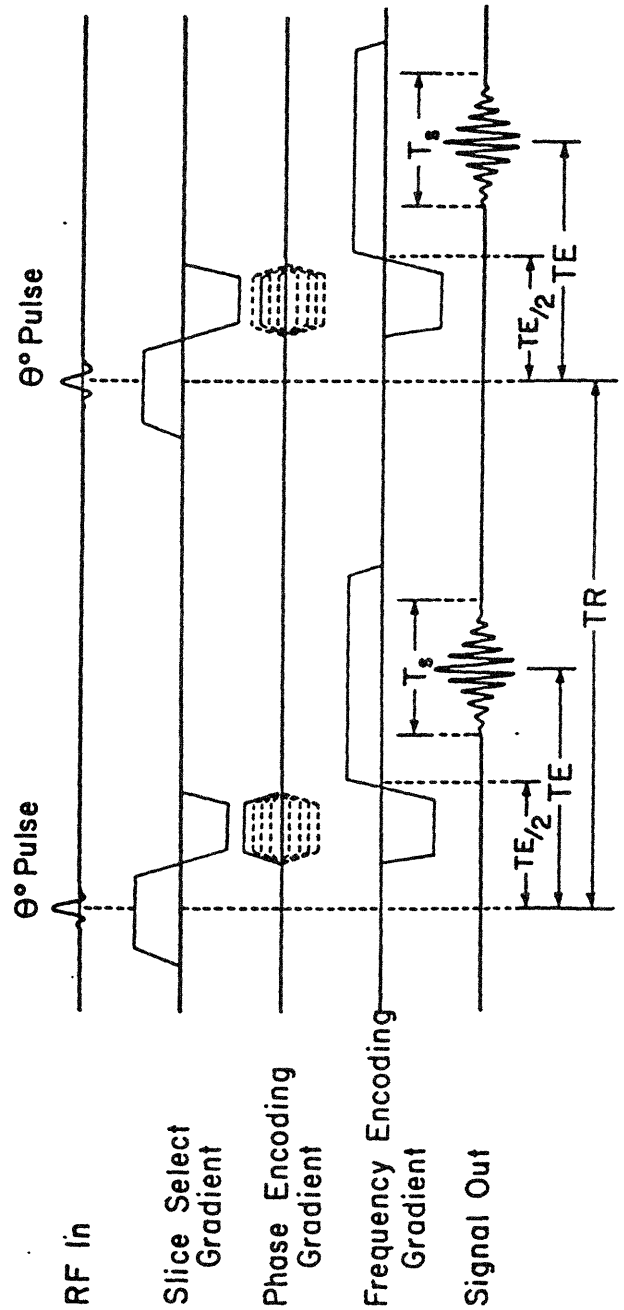

Figure 3.3.1 A generic gradient echo pulse sequence.

Comparing the sketches of the echoes created in the spin echo sequence (Figure 2.11.2) and the gradient echo sequence (Figure 3.3.1) suggests that these two echoes are identical. However, there are important differences between the echoes. These differences originate from the actual process of spin dephasing. There are two types of dephasing which occur after any excitation. (In the gradient echo experiment, the gradient reversal produces the echo, and in the spin echo experiment, the 180° pulse produces the echo.) The first dephasing is induced by the gradient which causes a spatial distribution of Larmor frequencies in the sample. The second type of dephasing is caused by local field inhomogeneities and can be divided into two subtypes. The first subtype arises from inhomogeneities in the main field, and the second subtype occurs because of magnetic susceptibility differences between anatomical tissues in the image. An example of susceptibility differences is the air/water interface typically seen in human nasal passages.

As discussed in Chapter 2, the spin echo reverses both types of dephasing described above because the total accumulated phase is reversed in time by the 180° pulse. However, the gradient echo technique only reverses the first type of dephasing, i.e. that from the gradient. Practically, the field inhomogeneities are minimized by the improving magnet technologies and the ability to correct (or "shim") the inhomogeneities. On the other hand, there is no correction for the susceptibility differences, and the quality of gradient echo images suffers in these anatomical regions.

Typically, GRE is practiced with low flip angles because of two competing effects. On one hand, the transverse magnetization obtained from a flip angle θ is proportional to $\sin\theta$, resulting in a maximal signal for $\theta = 90°$. On the other hand, large flip angles introduce saturation effects due to incomplete longitudinal relaxation for short

TR. Hence, there is a tradeoff between effects, and commercial systems for clinical imaging choose a compromise, typically $\theta = 30°$.

Like the SE and CPMG sequences, the total scan time for GRE follows Eq. 3.1.1. For GRE n = 1, and as hinted above, the speed advantage is obtained by decreasing TR. Assuming a TR of 50 msec, a GRE sequence for a 256 x 256 image matrix and 2 averages per phase encode step has an image time per slice of 0.05 x 2 x 256 = 25.6 sec. This is a ten-fold decrease in time as compared to the SE sequence described in Section 3.1. In addition, the fastest GRE methods such as snapshot FLASH[14] and TurboFLASH[15] have TR values of 10 msec which produce images in approximately 1 second. This creates new applications such as "breath hold" images of the abdomen.[16] These sequences which have low TR values take advantage of improved gradient switching hardware developed for echo-planar imaging (EPI), the subject of the following section.

Section 3.4 Echo-planar imaging (EPI)

EPI is currently the fastest imaging MRI method. In EPI a complete planar image is obtained from one selective excitation pulse. There are several permutations of the original EPI technique; this section presents the original pulse sequence[17,18] and a "blipped" echo-planar technique[19] called spin-echo MBEST (Modulus Blipped Echo-Planar Single-pulse Technique).[20] After the two sequences are described, the total scan time is estimated by a simple calculation, and the present limitations of EPI are discussed.

The original EPI sequence and its associated k-space diagram are illustrated in Figure 3.4.1. The sequence begins at $t < T_A$ with a selective excitation pulse to define a slice and produce a maximal M_{xy} as in the SE sequence. This is followed ($t > T_A$) by the strong frequency encoding gradient G_x oscillating in polarity as often as possible and a

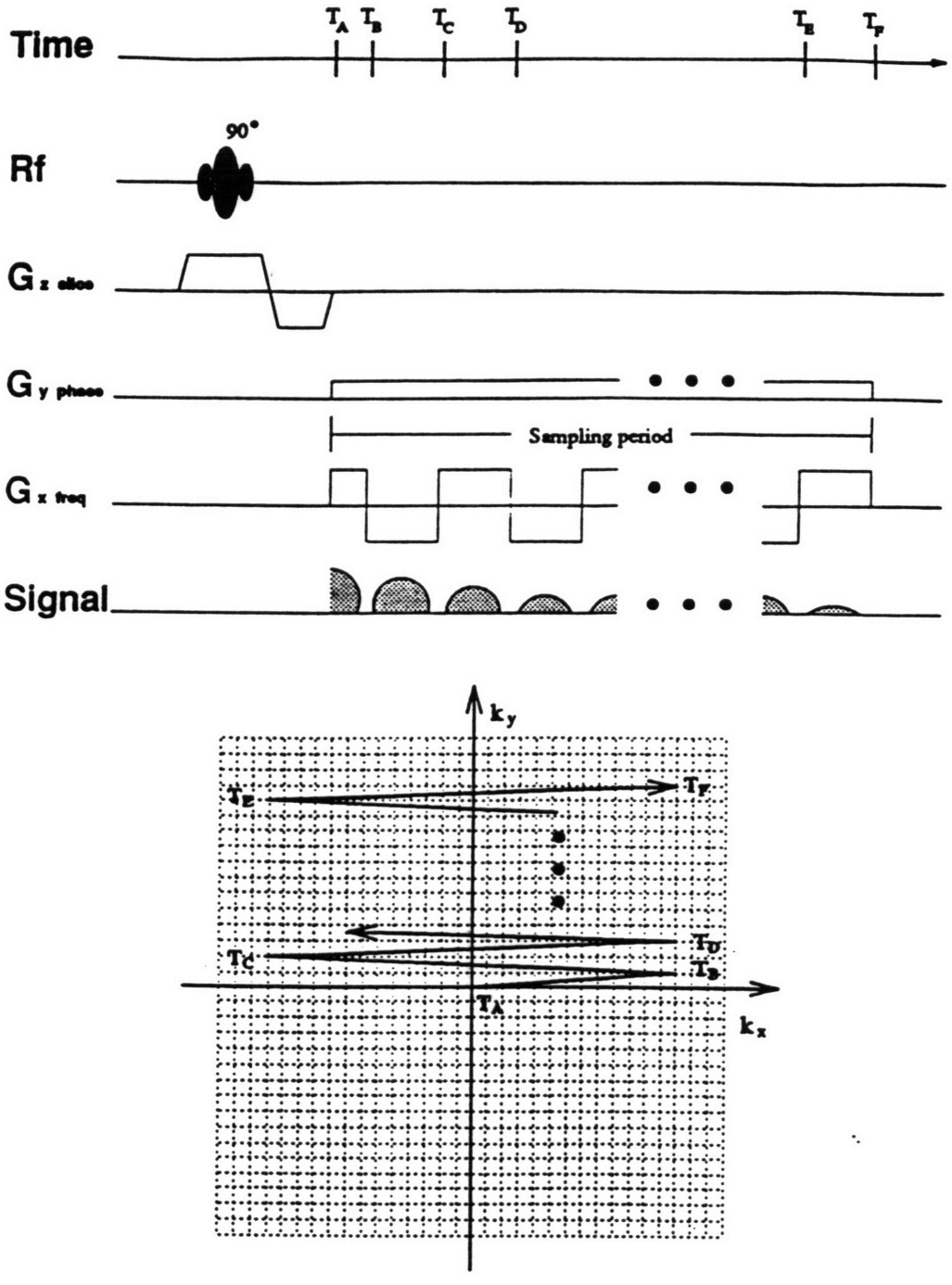

Figure 3.4.1 The original 2D EPI pulse sequence and it associated k-space diagram.

much smaller constant phase encoding gradient G_y. The result is a rapid frequency dephasing and rephasing which produces a gradient echo train yielding information along k_x while G_y gradually increases the phase as in the k-space diagram. Thus, a single excitation covers one-half of k-space with a "zig-zag" trajectory.

Since the original EPI trajectory does not sample the data on a rectilinear grid, a new generation of EPI related techniques were designed to alleviate this problem. One example is the spin-echo MBEST illustrated in Figure 3.4.2. As its name suggests, this sequence differs from the original EPI sequence in two ways. First, spin-echo MBEST uses a spin echo technique at $t < T_C$ to minimize the T2* signal loss associated with the gradient echoes in the original sequence. The second difference is the nature of the phase encoding gradient G_y. Instead of a small amplitude constant gradient, the spin-echo MBEST sequence uses a series of G_y pulses which correspond in time with the zero crossing of the oscillating G_x gradient. These pulses are called "blips" and have the effect of rapidly incrementing the phase immediately prior to the readout or data acquisition time. The result is twofold: k-space is covered on a rectilinear grid, and the technique allows k-space to be completely acquired with a single excitation.

Chapter 2 considers several of the tradeoffs in MRI and emphasizes that virtually all improvements in MRI technology have a price. The same holds true for EPI. Since EPI requires rapid switching in the gradient coils, eddy currents are induced in the conducting structure.[21,22] Consequently, data acquisition is delayed by a waiting time during which the eddy currents decay. Typical eddy currents in a superconducting magnet may require 10-20 msec to decay, and assuming a T2 relaxation of 250 msec, a maximum of perhaps 20 lines of k-space could be obtained in a single excitation. To alleviate this limitation, manufacturers typically make what is known as an actively shielded gradient coil set. This consists of at least two coils: the inner coil creates the

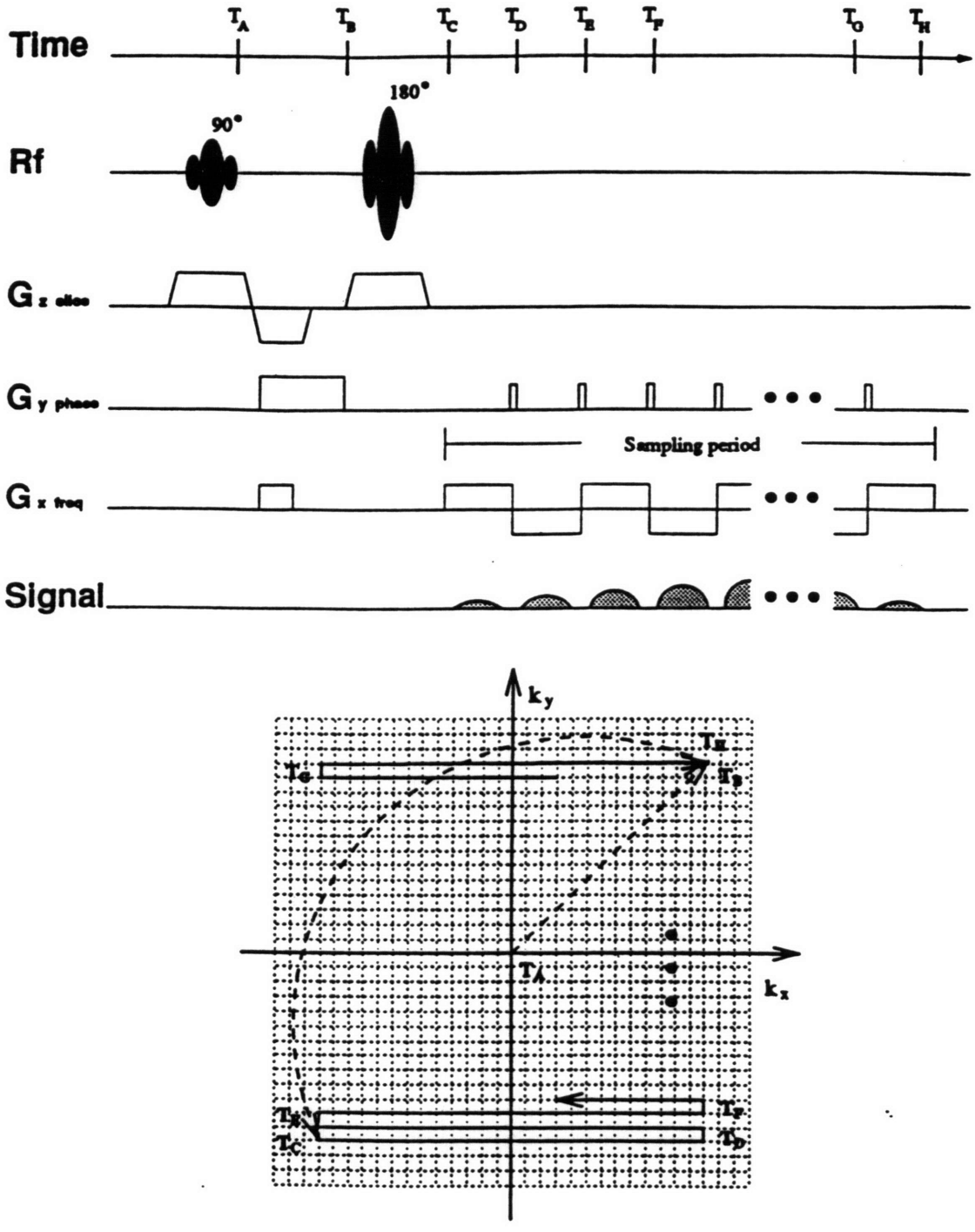

Figure 3.4.2 Pulse sequence for the spin echo MBEST technique and its associated k-space diagram.

gradient, and the outer coil cancels the gradient field from the first coil outside the second coil. By canceling the field outside the second coil, the magnetic flux linkage between the gradient coils and any of the conducting structures of the magnet is substantially reduced. Thus, gradient switching is possible with minimal eddy currents in the conducting structure, and a typical gradient coil set can accomplish field switching in less than 1 msec. There are two prices for this hardware. First, additional radial space is required in the bore tube of the magnet for the second coil. The second price is financial. In addition to the cost of the coil set, EPI requires additional and stronger power supplies.

Given this introduction to EPI, the discussion turns to the speed of the technique. As seen from the pulse sequences, the overall imaging time is strongly dependent on the speed of the field switching. Present technology allows for switching at a maximal rate of 1 per several hundred μsec. (The problems associated with this rapid switching are described above.) For simplicity assume a 100 μsec switch time and 128 lines of k-space. As seen in the pulse sequence, each line of k-space requires two field switches. Thus, the time spent switching the gradients is twice the product of the switching time and the number of lines of k-space, or 25.6 msec. For this example, the total acquisition time (for all k-space data) is the sum of the switching time (25.6 msec) and the time to collect the k-space data. The time to collect k-space data is the product of the number of k-space lines (128) and the collection time per line which is approximately 100 μsec. This gives a total of about 13 msec for collecting the data and a total acquisition time near 40 msec.

Section 3.5 Conclusions

The goal of this chapter is to introduce fast imaging and give a flavor of current techniques which reduce the overall scan time for MRI. In addition to the techniques which speed up conventional SE imaging such as restricting the number of phase encode steps, multiple slice acquisition, and Half-Fourier imaging, this chapter reviews three

rapid imaging pulse sequences: the Carr-Purcell-Meiboom-Gill sequence, gradient-echo imaging, and echo-planar imaging. Special emphasis is given to the echo-planar technique since this thesis introduces two new pulse sequences based on the PERL technology which can create subsecond images. In fact, one of the two pulse sequences collects an entire set of 2D spatial information in a single excitation without field switching! As expected, the tradeoffs for this sequence are large, and these tradeoffs are discussed in Chapter 4. Since there is no field switching, eddy currents are not produced, and actively shielded gradient coil sets are not required. The second of the two pulse sequences incorporates limited field switching and resembles the blipped technique in spin echo MBEST (Figure 3.4.2), except that it uses the novel PERL field instead of standard linear gradients for encoding. The consequences of incorporating this new method of spatial encoding to MRI is the subject of the remainder of this work.

Chapter 3 References

[1] MS Cohen and RM Weisskoff. Ultrafast Imaging. Magnetic Resonance Imaging 9:1, 1991.
[2] MS Cohen and J Fordham. Developments in Magnetic Resonance Imaging. Invest Radiol 28 Supp 4, S32, 1993.
[3] HY Carr and EM Purcell. Effects of dissusion on free precession in nuclear magnetic resonance experiments. Physiol Rev 94:630, 1954.
[4] S Meiboom and D Gill. Modified spin-echo method for measuring nuclear relaxation times. Rev Sci Instrum 29: 688, 1958.
[5] J Hennig et al. Magnetic Resonance in Medicine 3:823, 1986.
[6] J Hennig et al. J Comput Assist Tomogr 10:375, 1986.
[7] J Hennig. Magnetic Resonance Imaging 78:397, 1988.
[8] PS Melki et al. Journal of Magnetic Resonance Imaging 1:319, 1991.
[9] S Patz. Steady state free precession: an overview of basic concepts and applications. In *Advances in Magnetic Resonance Imaging, Vol.1* (E Feig, ed.) Ablex Publishing, 1989.
[10]A Hasse et al. FLASH imaging: rapid NMR imaging using low flip angle pulses. Journal of Magntic Resonance 67:217, 1986.
[11] J Frahm et al. German patent 3504734, Feb. 12, 1985.
[12] J Frahm et al. Magnetic Resonance in Medicine 3:321, 1986
[13] RC Hawkes and S Patz. Rapid Fourier imaging using steady state free precession. Magnetic Resonance in Medicine 3:9, 1987.
[14] A Hasse. Snapshot FLASH MRI: applications ot T1, T2, and chemical shift imaging. Magnetic Resonance in Medicine 13:77, 1990.
[15] M Deimling et al. Diffusion-weighted imaging with TurboFLASH with reordered phase encoding. Journal of Magnetic Resonance Imaging 1:202, 1991.
[16] RR Edelman et al. Segmented TurboFLASH: method for breath-hold MR imaging of the liver with flexible contrast. Radiology Vol 177, No 2, 515, Nov 1990.
[17] P Mansfield. Journal Physics C 10:L55, 1977.
[18] P Mansfield and IL Pykett. Journal of Magnetic Resonance 29:355, 1978.
[19] IL Pykett and RR Rzedzian. Magnetic Resonance in Medicine 5: 563, 1987.
[20] R Turner and D Le Bihan. Journal of Magnetic Resonance 86:445, 1990
[21] CB Ahn and ZH Cho. Analysis of eddy currents in NMR imaging. Magnetic Resonance in Medicine 17:149, 1991.
[22] MA Morich et al. Exact temporal eddy current compensation in MRI systems. IEEE Transactions on Medical Imaging Vol 7, No 3, Sep 1988, p. 247.

CHAPTER 4. The PERL encoding field.

Section 4.1 Introduction and goals

This chapter describes the PERL field and shows its utility for encoding spatial information for MRI. A pulse sequence is presented to image static spins using both the PERL field and the standard set of linear gradient encoding fields. Theoretical expressions for the signal are derived and limitations on parameters imposed by experimental considerations are discussed. These limitations lead to the development of a second pulse sequence and shed insight on the spectrum of imaging techniques created by the PERL encoding field. To introduce the novel reconstruction, the reconstruction mathematics is outlined and an initial reconstruction is proposed. The shortcomings of this preliminary method illustrate several of the fundamental differences between the PERL encoding field and standard linear gradients. (The reconstruction problem is solved in detail in Chapters 5 and 6.)

Section 4.2 Pulse sequence utilizing the PERL field

As discussed in Chapter 2, MRI uses magnetic field gradients to encode spatial position, and the most common MRI pulse sequence is the 2DFT spin echo sequence shown in Figure 2.11.2. As described in Section 2.11, this technique obtains different lines of k-space by multiple excitations and varying the magnitude of the phase encoding gradient G_y.

In order to decrease the overall imaging time, 2D k-space data can be acquired with a single excitation; this is the idea underlying EPI shown in Figure 3.4.2. In review, the 2D k-space data is obtained by blipping the phase encoding gradient G_y in the presence of an oscillating readout gradient, and each blip of G_y corresponds to a different line of k-space. Although the echo-planar technique dramatically decreases the overall

imaging time, it requires expensive hardware such as actively shielded gradient coils to compensate for the eddy currents produced by a rapidly changing magnetic field.

This thesis proposes a novel encoding technology which in theory allows the acquisition of 2D spatial data without the burden of gradient switching. The field is called PERL since it is PERiodic in one dimension and Linear in an orthogonal dimension. The periodic component is chosen in the z-dimension, and the linear component is chosen in the x-dimension as illustrated in Figure 4.2.1. As described in the introduction, the functional form of the PERL field is

$$B_z(x,z) = g_x x \cos(q_z z). \qquad [1.1.1]$$

The proposed pulse sequence which yields 2D spatial data without gradient switching appears in Figure 4.2.2. It is a simple variant of the spin echo experiment in which the PERL field is applied for time T as a "pre-encode" field between the 90° and 180° pulses. The entire 2D data set is acquired in the xz plane with a constant amplitude linear gradient along z. If slice selection in the y-coordinate is desired, either the 90° or 180° or both pulses can be made slice selective and a gradient in the y-dimension applied during these RF pulses to select a slice. Since the PERL field is applied for a time T, the phase shift just prior to the 180° pulse is

$$\Phi = \gamma g_x x T \cos(q_z z). \qquad [4.2.1]$$

The 180° pulse inverts the sign of the phase shift. After the 180° pulse, the linear gradient G_z is applied. Defining time $t=0$ as the point at which G_z is applied, the accumulated phase at time $t>0$ is

$$\Phi(t) = \gamma[G_z z t - g_x x T \cos(q_z z)]. \qquad [4.2.2]$$

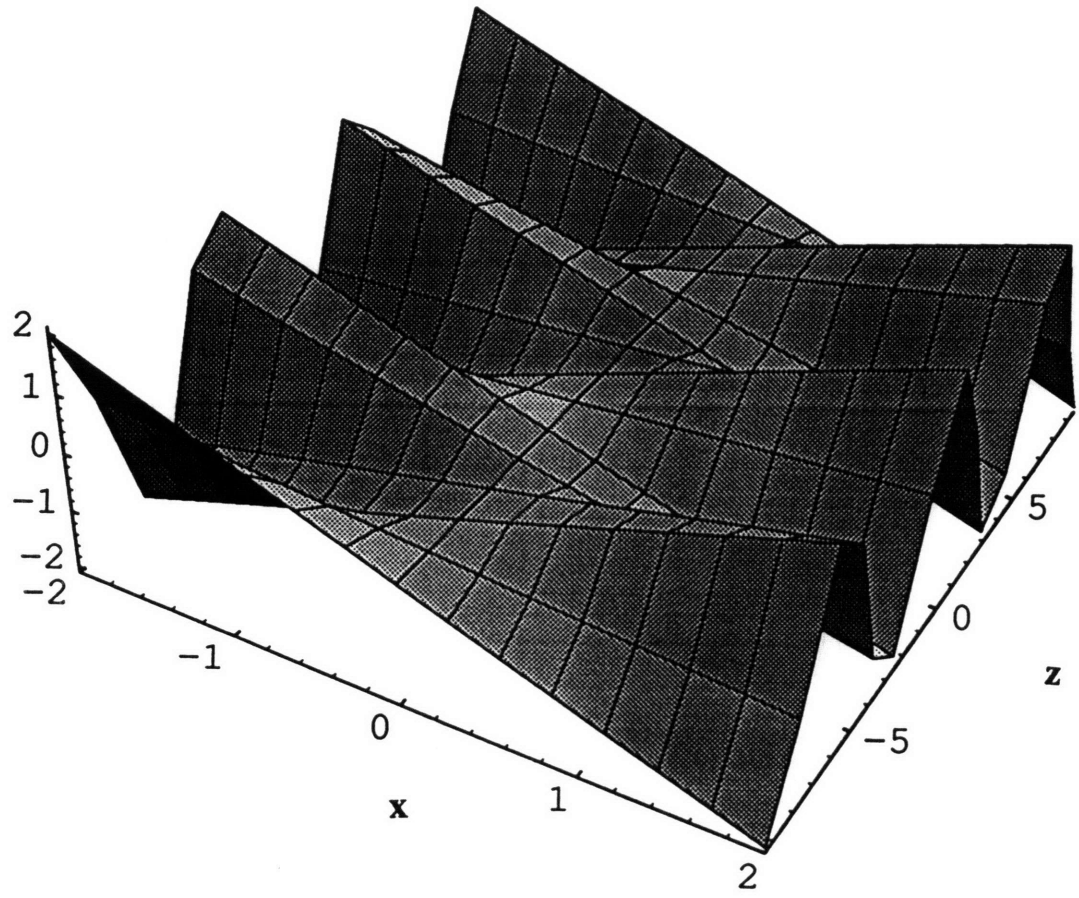

Figure 4.2.1 The PERL encoding field, $B_z(x,z) = g_x x \cos(q_z z)$.

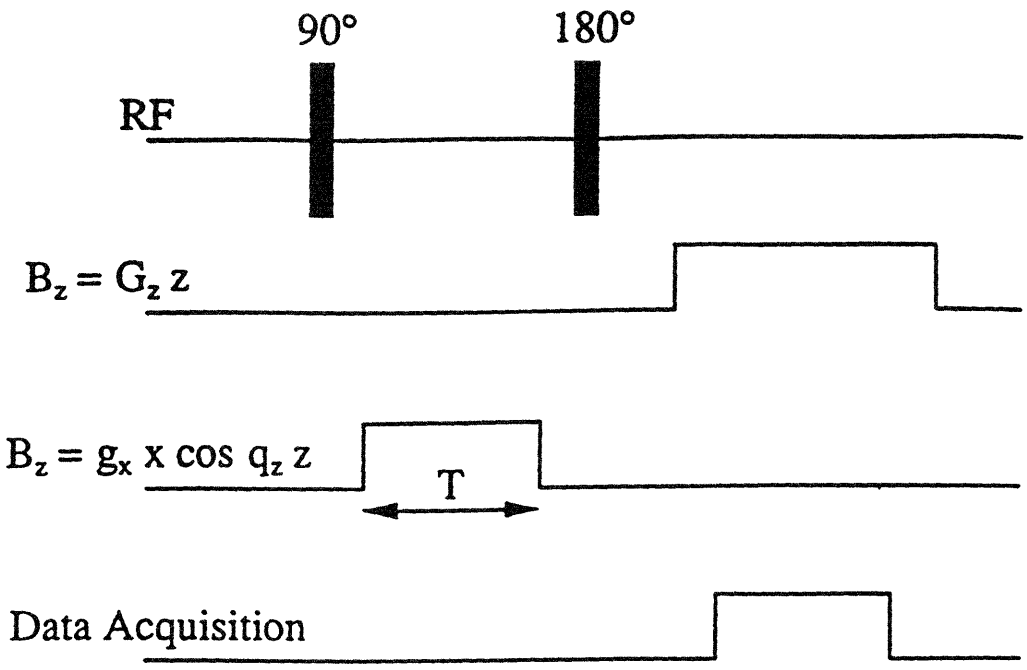

Figure 4.2.2 Pulse sequence utilizing the PERL field. Data is acquired in the xz plane with a single excitation.

Section 4.3 Derivation of the PERL signal

The generalized expression for the MRI signal described in Section 2.8 is

$$S(t) = \int_{\alpha,\,\beta} \rho(\alpha,\beta) \exp[i\,\Phi(t)]\, d\alpha\, d\beta \qquad [4.3.1]$$

where α and β are the independent orthogonal spatial variables of the image spin density ρ. Note that Eq. 4.3.1 ignores the effects of T1 and T2 relaxation which would introduce multiplicative factors according to the standard formulae. (See Eq. 2.10.4) The weighting of the signal from the relaxation of the transverse magnetization results in the multiplicative factor exp [-TE / T2] where TE is the time of a particular spin echo. The weighting from longitudinal relaxation includes the factor 1 - exp [-TR / T1] where TR is the repetition time of the 90° excitation pulses. For simplicity in the mathematics, these two multiplicative factors are removed from the equations.

Defining the 2D spin density as $\rho(x,z)$ and substituting Eq. 4.2.2 into Eq. 4.3.1, the signal S(t), termed the PERL signal, becomes

$$S(t) = \int \int \rho(x,z) \exp\{i\,\gamma[G_z z t - g_x x T \cos(q_z z)]\}\, dx\, dz\,. \qquad [4.3.2]$$

Equation 4.3.2 is important for two reasons. First, it explicitly proves that the PERL signal S(t) is not related to the image spin density $\rho(x,z)$ by a 2DFT. Second, it marks the point mathematically at which this imaging technology departs from the standard MRI techniques described in Chapter 2.

The mathematical departure begins with an expansion of a plane wave in a series of cylindrical waves:

$$e^{ia\cos\theta} = \sum_{n=-\infty}^{\infty} i^n J_n(a)\, e^{in\theta}, \qquad [4.3.3]$$

where $J_n(a)$ is the Bessel function (first kind) of integral order n defined by

$$J_n(a) \equiv \sum_{k=0}^{\infty} \frac{(-1)^k (a/2)^{2k+n}}{k!\,(k+n)!}. \qquad [4.3.4]$$

The function $J_n(a)$ is a solution to the second order linear differential equation $x^2y'' + xy'' + (x^2 - n^2)y = 0$ which is termed Bessel's equation. It is interesting to note that Bessel's equation was first studied by Bernoulli who in 1703 was investigating the oscillatory behavior of a hanging chain. Moreover, it was Bernoulli who solved Bessel's equation in the series form of Eq. 4.3.4. Nevertheless, in 1824 Bessel completed his systematic study of the properties of the function $J_n(a)$ which now bears his name.[1] Figure 4.3.1 illustrates the function $J_n(a)$ for several orders n.[2]

Equation 4.3.3 was first noted by Jacobi[3] in 1836; similar results and additional properties were obtained in 1855 by Anger.[4] Thus, Eq. 4.3.3 is known as the Jacobi-Anger expansion theorem for a complex exponential with a cosinusoidal argument. The proof of Eq. 4.3.3 given below derives and uses the generating function for the Bessel coefficients. This approach leads to an elegant solution and establishes a foundation on which to derive other theorems used later in the text.

Consider the function

$$f(a,t) = \exp\left[\frac{a}{2}\left(t - \frac{1}{t}\right)\right] \qquad [4.3.5]$$

which can be expressed as the product of the two exponentials $\exp\left[\frac{at}{2}\right]$ and $\exp\left[\frac{-a}{2t}\right]$. Note that $\exp\left[\frac{at}{2}\right]$ may be expanded into an absolutely convergent Maclaurin series of ascending powers of the variable t while $\exp\left[\frac{-a}{2t}\right]$ may be expanded into an absolutely convergent Laurent series of descending powers of t, with the exception of $t = 0$. Thus,

$$f(a,t) = \sum_{j=0}^{\infty} \frac{(at/2)^j}{j!} \sum_{k=0}^{\infty} \frac{(-a/2t)^k}{k!} = \sum_{j=0}^{\infty} \sum_{k=0}^{\infty} \frac{(-1)^k (a/2)^{j+k}}{j!\,k!} t^{j-k}. \qquad [4.3.6]$$

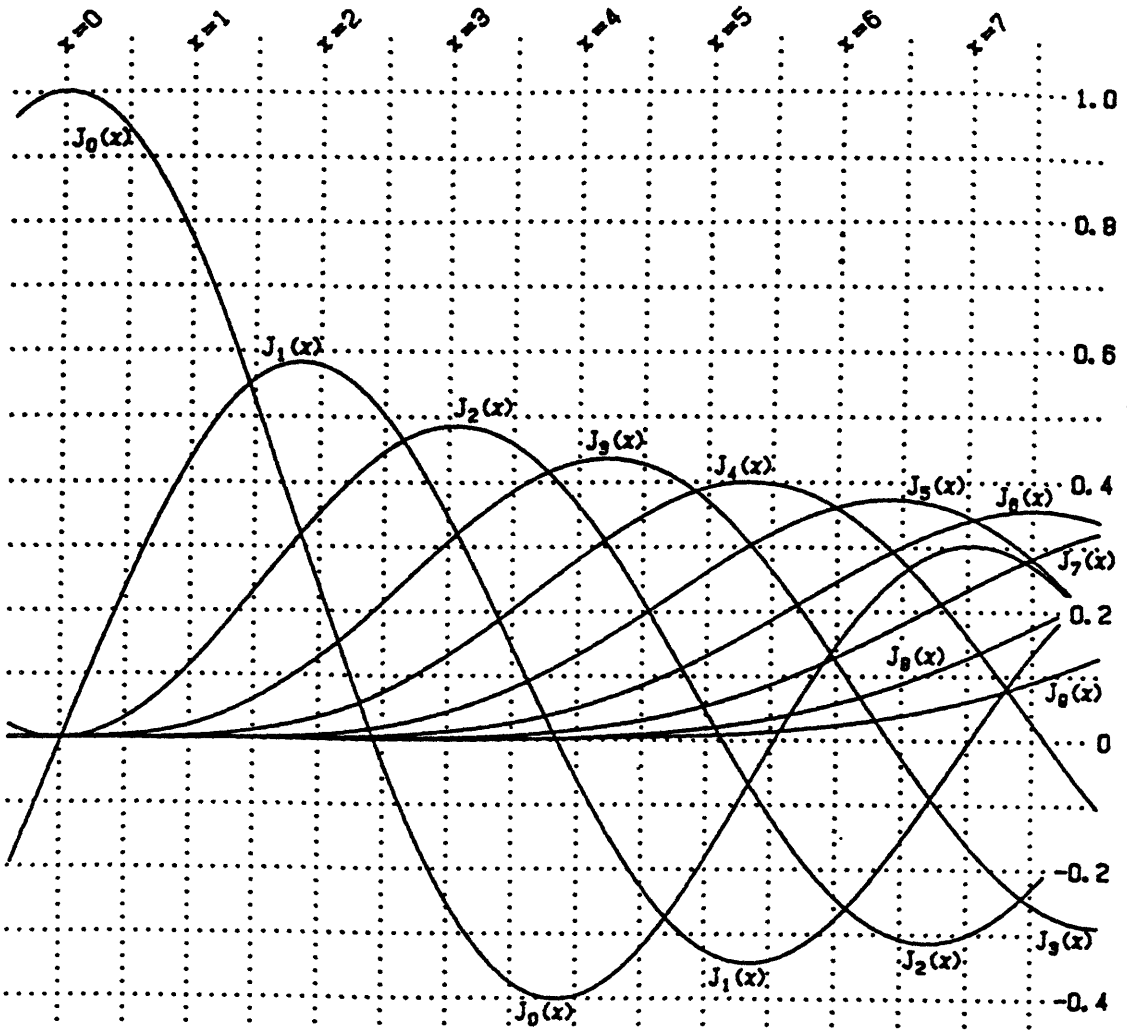

Figure 4.3.1.a Plot of the Bessel function $J_n(x)$ for several orders of n.

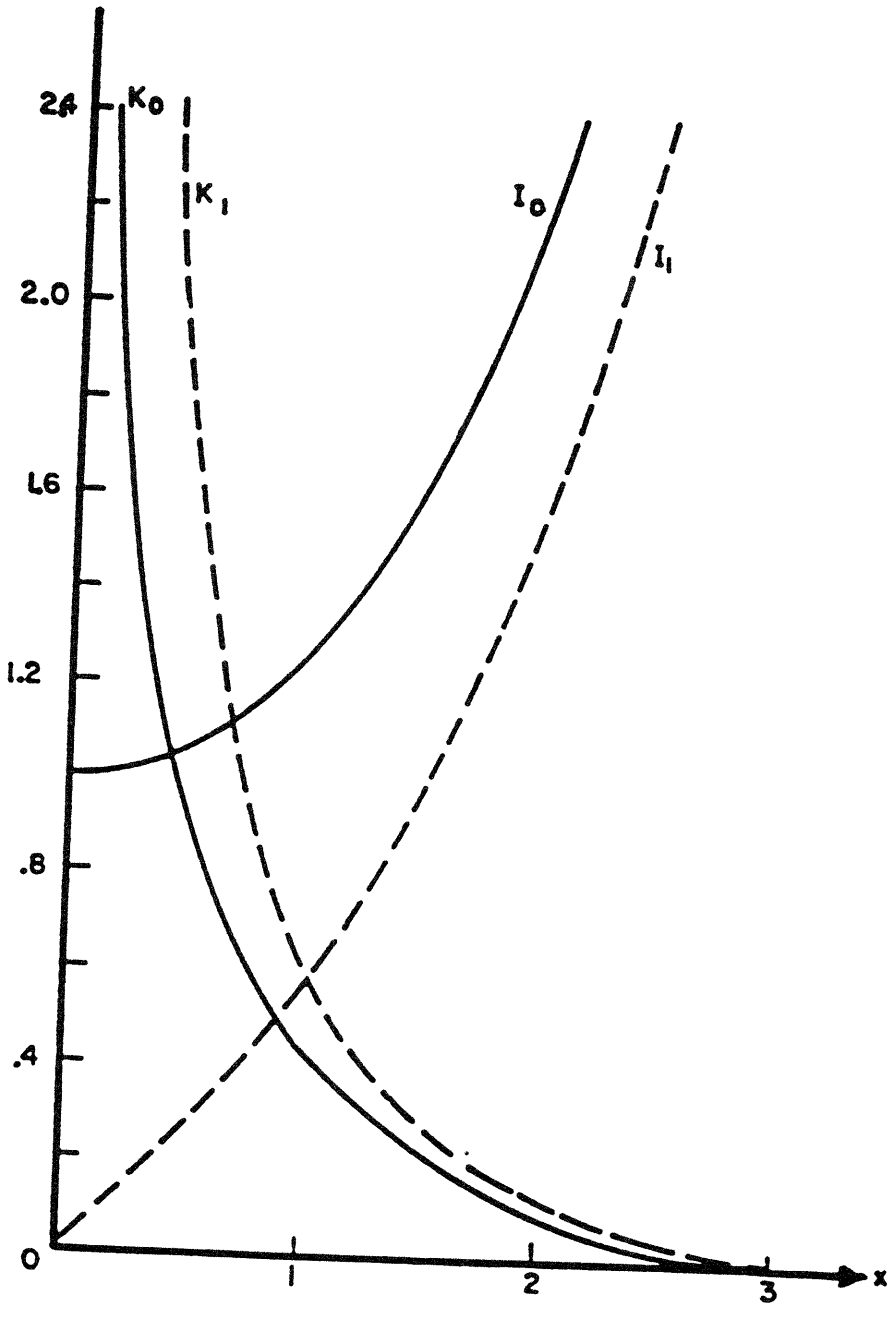

Figure 4.3.1.b Plot of selected modified Bessel functions.

Defining $n \equiv j - k$, Eq. 4.3.6 is recast as a double sum over n and k where $-\infty < n < \infty$.

$$f(a,t) = \sum_{n=-\infty}^{\infty} \sum_{k=0}^{\infty} \frac{(-1)^k (a/2)^{2k+n}}{k!\,(k+n)!} t^n \qquad [4.3.7]$$

and comparison with the definition in Eq. 4.3.4 shows that $f(a,t)$ is the desired generating function

$$f(a,t) = \exp\left[\frac{a}{2}\left(t - \frac{1}{t}\right)\right] = \sum_{n=-\infty}^{\infty} J_n(a)\, t^n \qquad [4.3.8]$$

for $t \neq 0$.

Replacing t with $(-t)^{-1}$ in Eq. 4.3.8 gives

$$\exp\left[\frac{a}{2}\left(\frac{-1}{t} + t\right)\right] = \sum_{n=-\infty}^{\infty} J_n(a)\,(-t)^{-n}, \qquad [4.3.9]$$

and replacing n with -n in Eq. 4.3.9 gives

$$\exp\left[\frac{a}{2}\left(\frac{-1}{t} + t\right)\right] = \sum_{n=-\infty}^{\infty} J_{-n}(a)\,(-t)^{n}. \qquad [4.3.10]$$

Since the power series expansion proposed in Eq. 4.3.6 is unique, Eqs. 4.3.9 and 4.3.10 prove an important lemma for the discussion of PERL signal acquired from the pulse sequence in Figure 4.2.2:

$$J_{-n}(a) = (-1)^n J_n(a) \text{ for integral n.} \qquad [4.3.11]$$

The generating function is now utilized to verify the Jacobi-Anger expansion. The substitution $t = e^{i\sigma}$ into Eq. 4.3.8 gives

$$\exp[ia \sin\sigma] = \sum_{n=-\infty}^{\infty} J_n(a)\, e^{in\sigma} \qquad [4.3.12]$$

after application of the equality $(e^{i\sigma} - e^{-i\sigma}) = 2i \sin\sigma$. The final substitution $\sigma = \theta + \pi/2$ yields Eq. 4.3.3.

Applying the Jacobi-Anger expansion (Eq. 4.3.3) to the PERL signal (Eq. 4.3.2) with $a = -\gamma g_x T x$ and $\theta = q_z z$:

$$S(t) = \sum_{n=-\infty}^{\infty} i^n \int \int \rho(x,z) \exp\{i z(\gamma G_z t + n q_z z)\} J_n(-\gamma g_x T x)\, dx\, dz. \quad [4.3.13]$$

The substitution $m = -n$ in Eq. 4.3.13 and the theorem

$$J_{-n}(-a) = J_n(a) \text{ for integral } n \quad [4.3.14]$$

allows the PERL signal to assume the following series of equations:

$$S(t) = \sum_m i^{-m} S_m(t), \quad [4.3.15]$$

$$S_m(t) = \int \rho'_m(z) \exp\{iz[\gamma G_z t - m q_z]\}\, dz, \quad [4.3.16]$$

and

$$\rho'_m(z) = \int_{x=-\infty}^{\infty} \rho(x,z) J_m(k_x x)\, dx \quad [4.3.17]$$

where

$$k_x = \gamma g_x T. \quad [4.3.18]$$

One derivation of Eq. 4.3.14 returns to the generating function for the Bessel coefficients and performs an analysis similar to the arguments leading to Eq. 4.3.11 from Eq. 4.3.5. However, the series definition in Eq. 4.3.4 leads to a more straightforward proof.

$$J_n(-a) = \sum_{k=0}^{\infty} \frac{(-1)^k (-a/2)^{2k+n}}{k!\,(k+n)!} = \sum_{k=0}^{\infty} \frac{(-1)^k (a/2)^{2k+n} (-1)^n}{k!\,(k+n)!} = (-1)^n J_n(a), \quad [4.3.19]$$

and since $J_{-n}(a) = (-1)^n J_n(a)$, Eq. 4.3.14 is verified.

Section 4.4 Physical interpretation of the PERL signal

The physical interpretation of Eqs. 4.3.15-18 is essential in understanding the PERL imaging technology. The PERL signal can be interpreted as a series of spin echoes $S_m(t)$ which form at times

$$t = \frac{mq_z}{\gamma G_z} \qquad [4.4.1]$$

at which the phase is zero. Thus, for the pulse sequence in Figure 4.2.2, an entire 2D data set is collected without switching the driving current to the encoding coil to different values during the data acquisition. Even with the best systems available today, the finite duration of the gradient switching time imposes limitations on the overall imaging speed. Hence, the PERL technology is theoretically faster than the fastest methods available to date. In theory, actively shielded gradient coils are not required for this system, and the costs of implementing this method are expected to be substantially less than those for EPI. In practice, this claim cannot be experimentally realized for most applications, and the method requires modifications described in Section 6 of this chapter. The modifications require the encoding field to be switched, however the number of switches is still significantly less than what is presently required for EPI.

The spin echo $S_m(t)$ and its associated function $\rho'_m(z)$, termed the partial spin density, are related by a 1DFT. Thus the z-component of the spin density is reconstructed by standard Fourier analysis. This is an expected result since the z-component of the spin density is linearly encoded. Because the 2D reconstruction of $\rho(x,z)$ is separable in x and z, the x-component reconstruction problem reduces to Eq. 4.3.17, a 1D integral in which the kernel is a Bessel function with an order corresponding to a specific number of the spin echo in the PERL signal. As described in Chapter 5, the calculation of the x-component of $\rho(x,z)$ from the known values of $\rho'_m(z)$ in Eq. 4.3.17 is the definition of the PERL transform.

Section 4.5 Conditions and constraints on the PERL technology

There are several constraints on parameters which influence the PERL signal, and these constraints govern the extent of the modifications required in the pulse sequence illustrated in Figure 4.2.2.

First, as noted above, a particular spin echo $S_m(t)$ forms when the phase in Eq. 4.3.16 is zero:

$$TE(m) = \frac{mq_z}{\gamma G_z}, \qquad [4.5.1]$$

where $\gamma = (2\pi)4257\,\mathrm{rad}/(\mathrm{G\,sec})$ and the spacing between successive spin echoes is calculated by setting $\Delta m = 1$:

$$\Delta TE(\Delta m = 1) = \frac{q_z}{\gamma G_z}. \qquad [4.5.2]$$

Second, each echo $S_m(t)$ must be identifiable; for the imaging technique illustrated in Figure 4.2.2, this is accomplished by forming echoes which are separable in time. That is, the spacing between successive spin echoes $\Delta TE(\Delta m = 1)$ is equal to or greater than the length of time t_{se} over which the spin echo is finite, or

$$t_{se} \le \frac{q_z}{\gamma G_z}. \qquad [4.5.3]$$

A third condition is dictated by the Nyquist criteria which states that the maximum measurable frequency during data acquisition equals one half the data sampling rate. However, the sampling rate is effectively doubled from quadrature detection. The inverse of the sampling rate, or the dwell time between sampling, is denoted by t_d. Thus, the Nyquist criteria is

$$\gamma G_z z_{res} N t_d = 2\pi \qquad [4.5.4]$$

where N is the number of data samples and z_{res} is the image resolution in the z-dimension. The quantity N t_d represents the total sampling time which is set equal to t_{se}, the time between successive spin echo peaks:

$$\gamma G_z z_{res} t_{se} = 2\pi. \qquad [4.5.5]$$

The second condition, the requirement that the spin echoes are separable in time, requires that each echo dephases before the next echo begins to rephase. This is assured for large values of N, because for each dwell time, the spins across the field of view accumulate a phase difference of 2π.

A simple example illustrates the conditions of Eqs. 4.5.1, 4.5.3, and 4.5.5 and introduces the constraint on the imaging technology. Consider the spin density $\rho(x,z)$ equal to one in the square region between 0 and 2 in both the x and z dimensions and equal to zero otherwise. (See Figure 4.5.1) Assume also that protons are being imaged; that is, $\gamma = (2\pi)$ 4257.6 rad/G s. Three successive spin echoes from the PERL signal calculated from this spin density appear in Figure 4.5.2.

In this example, $\Delta TE\ (\Delta m = 1) = t_{se} = 1$ ms . Hence, to achieve 1mm resolution in the z-dimension, z_{res} = 1 mm, Eq. 4.5.5 requires that $G_z = 1.2$ G/cm Substituting this value into Eq. 4.5.2 gives the result $q_z = (2\pi)10.2$ cycles/cm where the value of q_z determines the spatial frequency of the periodic component of the PERL field. In this example Eq. 4.5.3 is satisfied; that is, the echoes are separable in time. If a 128 x 128 image is desired, each m echo is sampled 128 times at the Nyquist sampling rate, and 128 different m echoes are sampled. Since each echo is separated by 1msec, the dwell time t_d for quadrature detection is 7.81 μsec. The effective field of view (FOV) in the z-dimension is

$$FOV_z = (SI\ \gamma G_z)^{-1} = 12.5\,\text{cm}. \qquad [4.5.6]$$

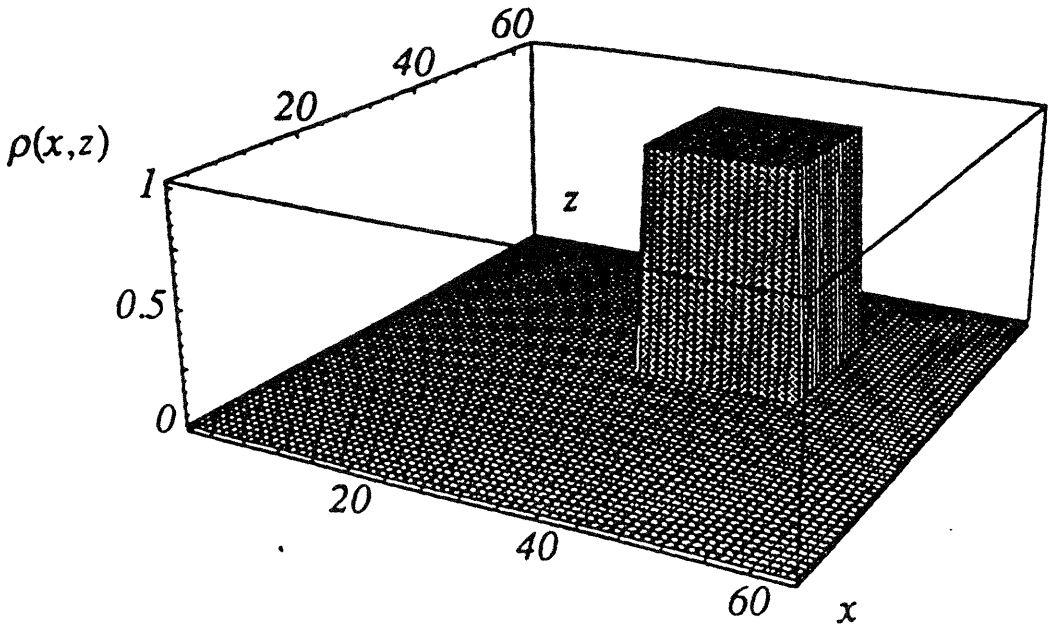

Figure 4.5.1 Assumed spin density equal to one in the square region between zero and two in both the x and z dimensions. The axes are labeled by pixel number. The origin is at pixel (33,33), and the pixel dimensions are 0.12 cm square.

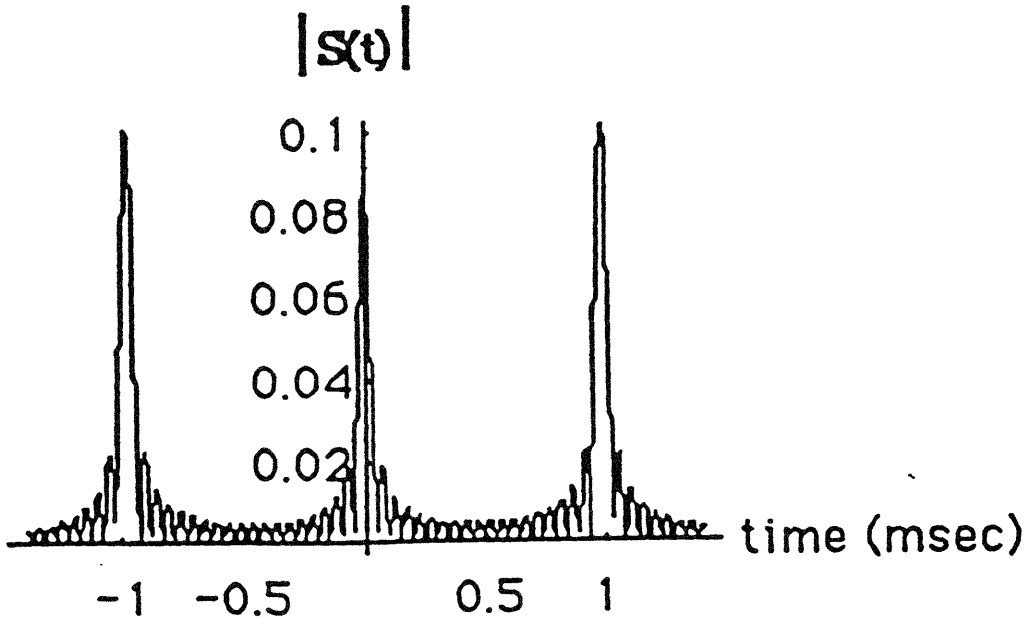

Figure 4.5.2 Calculated PERL signal from the spin density equal to one in the square region between zero and two in both the x and z dimensions.

The mathematics of this simulation lend considerable insight to the PERL signal are therefore are described in detail. Using Eqs. 4.3.16-18 to write the m^{th} echo $S_m(t)$,

$$S_m(t) = \int_{z=-\infty}^{\infty} \int_{x=-\infty}^{\infty} \rho(x,z) \exp\{i z(\gamma G_z t - m q_z z)\} J_m(\gamma g_x T x)\, dx\, dz . \quad [4.5.7]$$

When $\rho(x,z)$ is constant, it may be removed from the integrand. Consequently, the double integral in Eq. 4.5.7 becomes separable. Using the condition $\rho(x,z) = 1$ and the fact that x and z are nonzero only in the interval [0, 2]:

$$S_m(t) = \int_{z=0}^{z=2} \exp\{i z(\gamma G_z t - m q_z z)\} dz \int_{x=0}^{x=2} J_m(\gamma g_x T x)\, dx . \quad [4.5.8]$$

The integral over z yields a sinc function; this is an expected result since the Fourier transform of a box function is a sinc function. Therefore,

$$S_m(t) = \frac{-i}{(m q_z - \gamma G_z t)} [\exp\{2i(m q_z - \gamma G_z t)\} - 1] \int_{x=0}^{x=2} J_m(\gamma g_x T x)\, dx \quad [4.5.9]$$

The sinc function is positioned in time at $t = \frac{m q_z}{\gamma G_z}$ as predicted by Eq. 4.5.1. Equation 4.5.9 illustrates that the PERL signal is a series of spin echoes, and when the spin density is a box, the m^{th} spin echo is a sinc function whose amplitude is modulated by the integral of a Bessel function of order m. In the echoes presented in Figure 4.5.2, the integrals are computed numerically.

The constraint on the PERL imaging technology mentioned above is appreciated by combining Eqs. 4.5.3 and 4.5.5 to yield

$$z_{res}\, q_z = 2\pi. \quad [4.5.10]$$

Since q_z determines the spatial frequency of the periodic component of the PERL field, Eq. 4.5.10 links the spatial resolution along z to the wavelength of the PERL field oscillations, and this relationship is independent of the other parameters in the pulse

sequence. A typical value for spatial resolution in a useful clinical image is 1mm. This is the value used in the example above, and substituting $z_{res} = 1\,\text{mm}$ in Eq. 4.5.10 gives $q_z \approx (2\pi)\,10\,\text{cycles/cm}$. To appreciate the problem this creates, consider the coil designs in Figures 4.5.3-4.

While these designs are preliminary in that they do not produce the PERL field as described in Eq. 1.1.1, they create a periodicity in the z-dimension with the same strategy as the final coil designs in Chapter 7. The periodicity is produced by altering the current direction in neighboring current elements; the field created by the rectangular coil (Figure 4.5.4) is illustrated in Figure 4.5.5 where a is the distance between the current sheets and d is the spacing between the current elements with currents in opposite directions.

As seen in Figure 4.5.6, the periodicity in the z-dimension is satisfying. (In this plot, $x = 0.125\,a$ and $y = 0$.) The problem created by Eq. 4.5.10 is seen in Figure 4.5.7 which plots the magnitude of B_z vs. d. (In this plot $x = 0.25\,a$, $y = 0$, and $z = 0.125\,a$, but the problem exists for all coordinates.) As the spacing between the current elements decreases, the magnitude of the field falls off rapidly. Recall from Eq. 4.5.10 that $q_z \approx (2\pi)\,10\,\text{cycles/cm}$ when $z_{res} = 1\,\text{mm}$. For the rectangular coil in Figure 4.5.4 and the PERL coil design in Chapter 7, when the distance x from the surface of the current elements (this corresponds to the xy plane in Figure 4.5.4) becomes larger than the spacing d between current elements, the field dies off rapidly. This is a consequence of the neighboring coil elements with currents in opposite directions. The fields created by these currents cancel each other when the distance is greater than d, and therefore, the useful region for imaging approximately equals the spacing between the opposing current elements. For $q_z \approx (2\pi)\,10\,\text{cycles/cm}$, this spacing is 1 mm, and thus the field penetrates approximately 1 mm into the sample.

TOP OF FIGURE

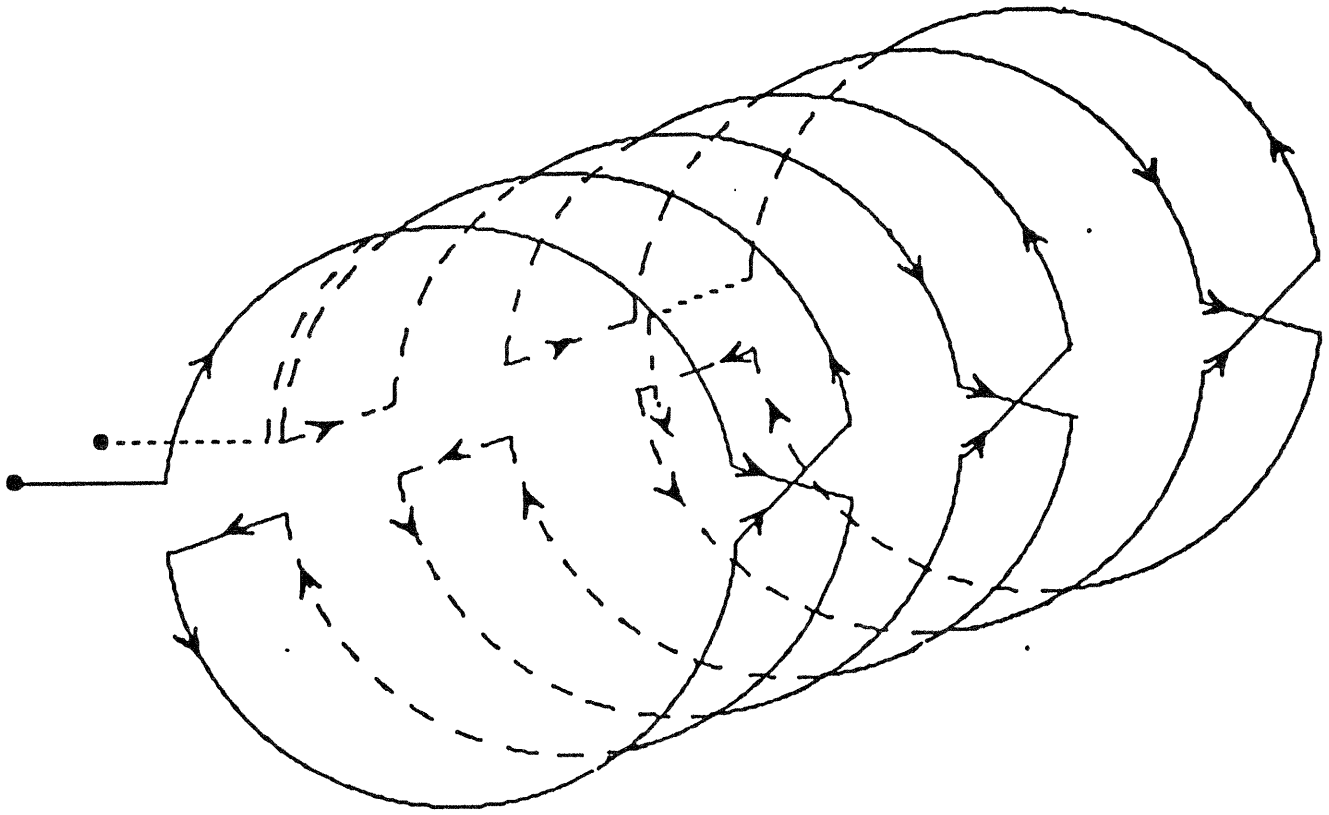

Figure 4.5.3 Preliminary coil design with cylindrical geometry to produce a periodic field in the z dimension.

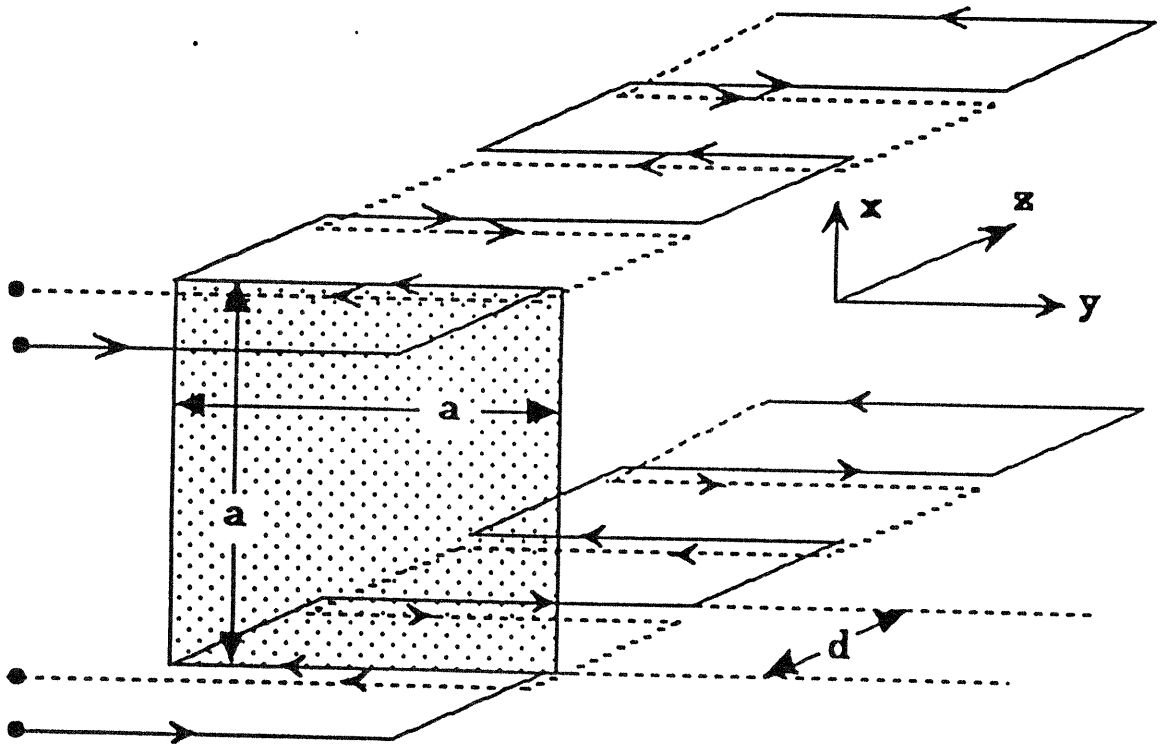

Figure 4.5.4 Preliminary coil design with rectangular geometry to produce a periodic field in the z dimension.

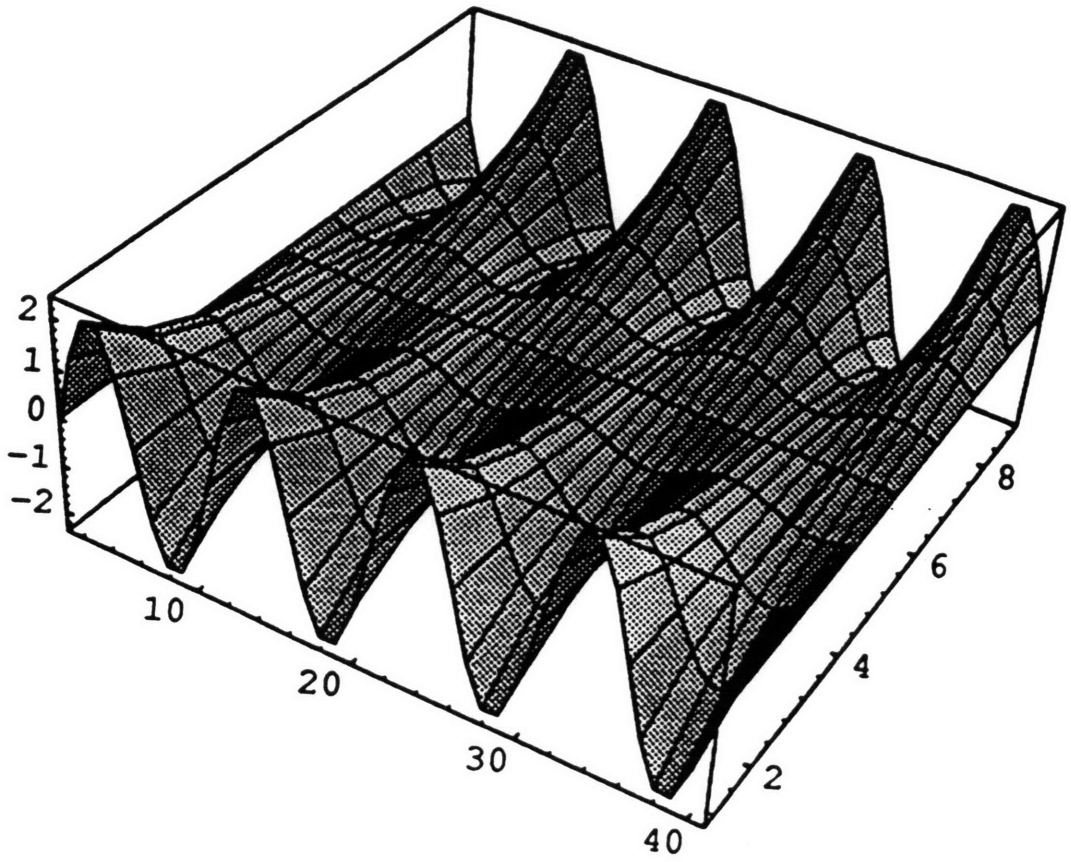

Figure 4.5.5 Three dimensional plot of the field generated by the preliminary rectangular coil design.

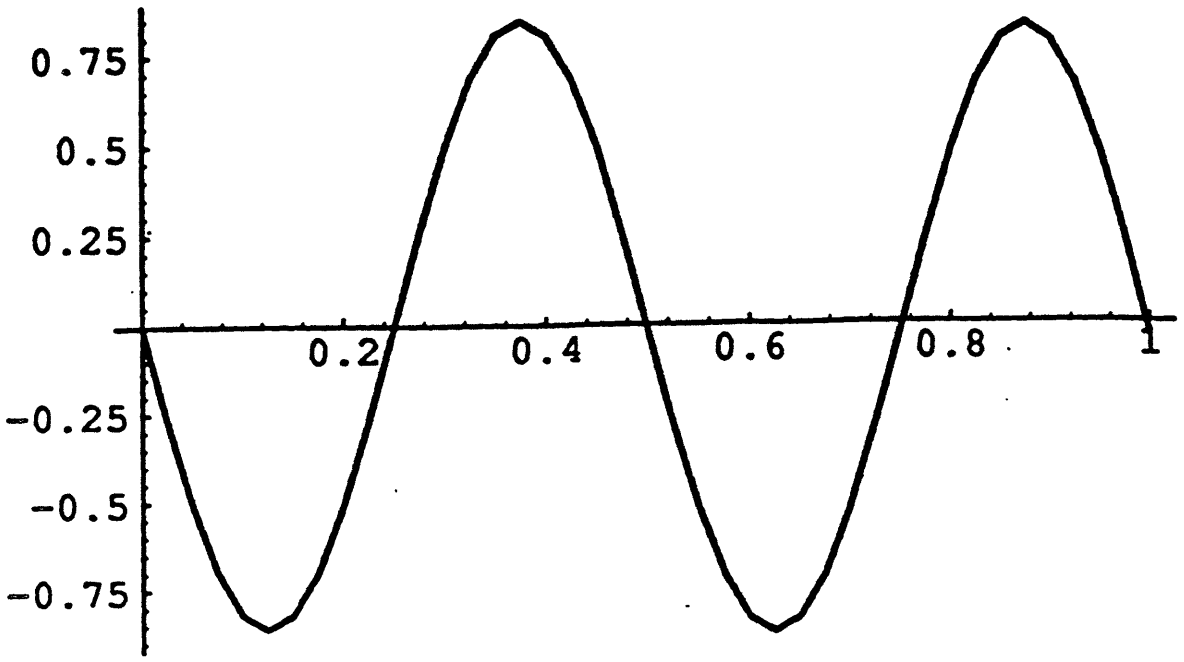

Figure 4.5.6 Plot of B_z vs. z illustrating the periodicity along z for the rectangular geometry. In this plot, x = 0.125 a and y = 0.

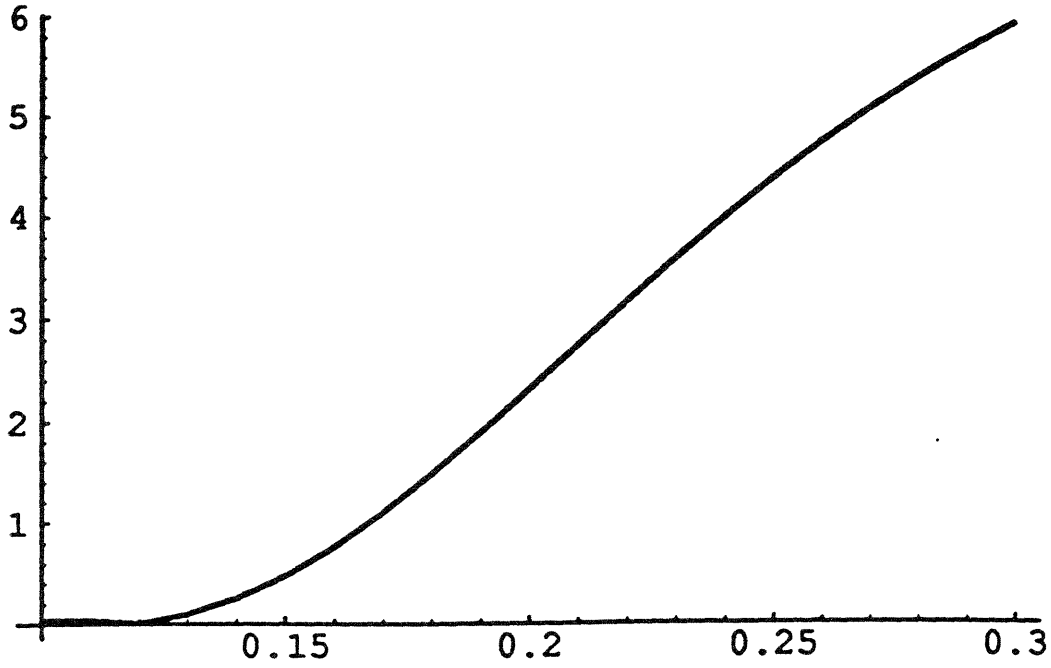

Figure 4.5.7 Plot of B_z vs. d illustrating the penetration problem as the spacing between current elements decreases. In this plot x = 0.25 a, y = 0, and z = 0.125 a.

This constraint is termed the "penetration problem" which exists for all periodic coils. Although the problem is discussed in detail above, it remains useful to briefly formalize the mathematics before discussing the solution in the following section. Consider the simplest form of a periodic field

$$B_z = \cos(q_z z) \qquad [4.5.11]$$

The restriction on B_z imposed by Laplace's equation is

$$-\frac{\partial^2 B_z}{\partial z^2} = \frac{\partial^2 B_z}{\partial s^2} \qquad [4.5.12]$$

where s is an orthogonal direction to z. In addition, taking the two partial derivatives of B_z with respect to z gives

$$-\frac{\partial^2 B_z}{\partial z^2} = q_z^2 B_z, \qquad [4.5.13]$$

and Eqs. 4.5.12-13 are combined to yield

$$-\frac{\partial^2 B_z}{\partial z^2} = \frac{\partial^2 B_z}{\partial s^2} = q_z^2 B_z. \qquad [4.5.14]$$

Equation 4.5.14 shows that the periodic dependence of z is coupled to the exponential dependence along s. The solution to Eq. 4.5.13 gives the periodicity in z, and the solution to Eq. 4.5.12 gives the exponential behavior along s. Thus, any periodic field in one direction will exhibit an exponential-like character along an orthogonal direction, and the behavior is characterized by the same parameter q_z.

Section 4.6 Modification of PERL imaging to allow deeper field penetration.

To image a region deeper than the spacing between the current elements, the pulse sequence in Figure 4.2.2 requires modifications to allow deeper penetration of the PERL field. The solution to this problem is to relax the wavelength of the field along z which is $\lambda = q_z/2\pi$. Thus, from Eq. 4.5.3 the spin echoes from the experiment are allowed to overlap. This is expressed mathematically as

$$t_{se} > \frac{q_z}{\gamma G_z}; \qquad [4.6.1]$$

that is, the separation between consecutive $S_m(t)$ spin echoes, $\Delta TE\,(\Delta m = 1)$, is less than t_{se}. To separate the different overlapping echoes, another encoding scheme similar to phase encoding is introduced. In this scheme the PERL field is modified by a controllable phase shift θ_n,

$$B_z = g_x x \cos(q_z z + \theta_n)\,. \qquad [4.6.2]$$

The modified PERL field is obtained by constructing two PERL coils with field profiles offset by a quarter wavelength, and varying the amplitude of the current driving each coil. Since $\cos(A+B) = \cos A \cos B - \sin A \sin B$, Eq. 4.6.2 is equivalent to

$$B_z = g_x x \left[\cos(q_z z)\cos\theta_n - \sin(q_z z)\sin\theta_n\right]. \qquad [4.6.3]$$

Thus, two PERL coils with functional forms

$$B_1 = g_x x \cos(q_z z) \qquad [4.6.4]$$

$$B_2 = g_x x \sin(q_z z) \qquad [4.6.5]$$

can create the desired phase shift θ_n by varying the amplitude of the current in the coils by $\cos\theta_n$ and $\sin\theta_n$ respectively. The signal produced by the modified PERL field has the same form as Eq. 4.3.15 with the added phase shift:

$$S_n(t) = \sum_m i^{-m} \exp(-i m \theta_n) S_m(t)\,, \qquad [4.6.6]$$

where $n = 1,...,N$. Hence, the number of required excitations and overlapping echoes equals N with each echo corresponding to a different value of θ_n.

As hinted above, to allow penetration of the PERL field into the sample, the pulse sequence requires phase encoding to a certain extent, and the N overlapping spin echoes

are resolved by a discrete FT. Since each signal has an associated θ_n, the encoding field requires different driving currents, and field switching is required. At first glance, the introduction of field switching appears to completely neutralize the speed advantage of the PERL technology. However, the following discussion shows that for many applications the number of required field switches is significantly less than with EPI. To appreciate the tradeoff between switches and penetration, consider an imaging application with cylindrical geometry requiring 3.2 cm of penetration. If the coil parameters are chosen as in Section 4.5, the separation between current elements is approximately 1 mm. Thus, each field switch yields 1mm of penetration, and 32 switches are required as opposed to 64 or greater which are required in EPI. In the resulting PERL signal, 32 echoes $S_m(t)$ overlap and are separated by their individual phase shifts. If an implementation required a penetration of only 8 mm, such as in surface imaging, only 8 switches of the encoding field are required.

Since the echoes overlap, the length of time for each θ_n acquisition is reduced by the overlap factor, and the entire acquisition is performed with a single excitation as shown in Figure 4.6.1. In some ways, this pulse sequence resembles the EPI sequence in Figure 3.4.2, and before analyzing the sequence, it is useful to step back and develop an intuition about the spectrum of encoding created by the PERL field. On one end of the spectrum is the pulse sequence in Figure 4.2.2 with zero field switching and $q_z \approx (2\pi)\,10\,\text{cycles/cm}$. This field has very little penetration since the wavelength of the PERL field is very small. On the other end of the spectrum, the penetration problem is completely alleviated by allowing a large number of field switches. This is mathematically equivalent to decreasing q_z and increasing the corresponding wavelength of the PERL field. In the limit, the wavelength becomes larger than the FOV, and the periodic component of the PERL field becomes linear. This is simply EPI: a single excitation technique with linear gradients in two orthogonal directions. Thus, the

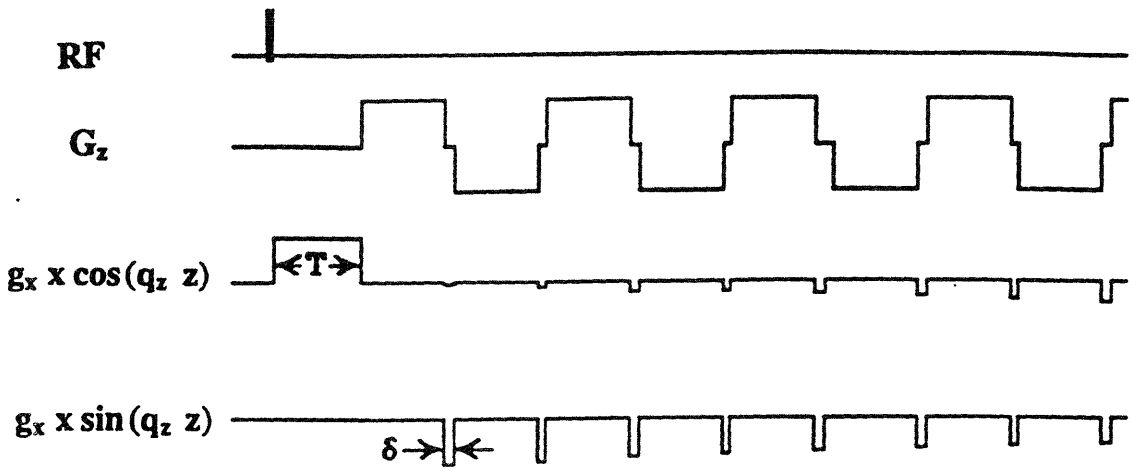

Figure 4.6.1 Modified pulse sequence using two PERL coils. See text for details.

fundamental principle underlying the PERL field is a new opportunity to image over a spectrum in which the image FOV is coupled to the number of field switches.

Returning to the pulse sequence in Figure 4.6.1, data is acquired at times where G_z is constant. The duration of the constant G_z interval before reversal is calculated for the case $N=32$ and $t_{se}=1$msec, that is, 32 overlapping echoes are acquired per msec. For a 128 x 128 image, the 128 echoes are obtained in a period of $4t_{se}=4$msec. The gradient G_z is reversed for each data acquisition with phase shift θ_n, and the pulse sequence uses a blipped technique using two PERL fields to increment θ_n. The initial cosine PERL field is applied for time T as in Figure 4.2.2 and creates the phase given in Eq. 4.2.1,

$$\Phi = \gamma\, g_x \,x\, T \cos(q_z z). \qquad [4.2.1]$$

To calculate the amplitude of the sine and cosine PERL fields required to change the phase shift from $\theta_{n-1}=(n-1)\theta_n$ to $\theta_n = n\,\theta_0$ where θ_0 is the incremental value of the phase shift equal to π/N, the change in phase $\Delta\Phi$ associated with the phase shift is written as

$$\Delta\Phi = \gamma g_x x T\cos[q_z z + n\theta_0] - \gamma g_x x T\cos[q_z z + (n-1)\theta_0] \qquad [4.6.7]$$

and

$$\Delta\Phi = \gamma B_1 \delta g_x x \cos(q_z z) + \gamma B_2 \delta g_x x \sin(q_z z) \qquad [4.6.8]$$

where δ is the blip time. Setting these two equations for $\Delta\Phi$ equal to one another and solving for B_1 and B_2 yields

$$B_1 = \frac{T}{\delta}\left[\cos(n\theta_0) - \cos\left\{(n-1)\theta_0\right\}\right] = B_{PERL}\cos(n\theta_0+\alpha) \qquad [4.6.9]$$

$$B_2 = -\frac{T}{\delta}\left[\sin(n\theta_0) - \sin\left\{(n-1)\theta_0\right\}\right] = -B_{PERL}\sin(n\theta_0+\alpha), \qquad [4.6.10]$$

where

$$\alpha = \tan^{-1}\left[\frac{\sin\theta_0}{1-\cos\theta_0}\right]. \qquad [4.6.11]$$

and the rms amplitude of the cosine and sine terms B_{PERL} is

$$B_{PERL} = \sqrt{B_1 + B_2} = \frac{T}{\delta}\sqrt{2(1-\cos\theta_0} \qquad [4.6.12]$$

and is independent of n. As expected, smaller phase increments θ_0 have smaller values of B_{PERL} since a small θ_0 corresponds to a small change in $\Delta\Phi$, and the phase shift is created with a small amplitude of the blip. For the case $N=32$, $B_{PERL} \approx 0.1\,T/\delta$. In the pulse sequence shown in Figure 4.6.1, the amplitude of the blips is qualitatively sketched using $\delta/T=0.1$, thus minimizing the time during which data is not acquired.

Section 4.7 Introduction to image reconstruction

The discussion of image reconstruction begins with the individual spin echoes $S_m(t)$. As described in the previous section, these echoes are obtained by a 1DFT of the phase encoded signal $S_n(t)$ which is sampled according to the Nyquist criteria. The first step of the reconstruction is based on Eq. 4.3.16; the partial spin density $\rho'_m(z)$ is obtained by an inverse Fourier transform of its associated spin echo $S_m(t)$. Thus, the z-component of the spin density is reconstructed by standard Fourier analysis.

Now consider the functions $\rho'_m(z)$. If an experiment using Fourier encoding were performed, an inverse Fourier transform in the z-dimension would reconstruct the complete spin density $\rho(x,z)$. (As detailed in Chapter 2, the k-space data and the spin density are related by a 2DFT in Fourier encoding.) However, the PERL signal does not have a simple and well-known relationship for the reconstruction in the z-dimension. Upon first inspection, this appears as not only a significant obstacle, but also an additional tradeoff for implementing the PERL imaging technology. Fortunately, this is not the case, and the remainder of this chapter, along with Chapters 5 and 6, derives the

full relationship between the PERL signal and the spin density. Chapter 6 also demonstrates the quality of image reconstruction by computer simulation.

Since it has been established that the 1DFT is not the correct operation to obtain the image spin density from $\rho'_m(z)$, the question becomes, "What is the correct operation?", or "What needs to be done to the functions $\rho'_m(z)$ to obtain $\rho(x,z)$?" One approach to the reconstruction uses the addition theorem for Bessel coefficients:

$$J_\nu(\alpha+\beta) = \sum_{m=-\infty}^{\infty} J_m(\alpha)\, J_{\nu-m}(\beta). \qquad [4.7.1]$$

The proof of Eq. 4.7.1 returns to the generating function for the Bessel coefficients. Substituting $\alpha + \beta$ for the variable a in Eq. 4.3.8 yields

$$\exp\left[\frac{1}{2}(\alpha+\beta)\left(t-\frac{1}{t}\right)\right] = \sum_{m=-\infty}^{\infty} J_m(\alpha+\beta)\, t^m \ . \qquad [4.7.2]$$

Writing the left-hand side as the product of exponentials

$$\exp\left[\frac{\alpha}{2}\left(t-\frac{1}{t}\right)\right]\exp\left[\frac{\beta}{2}\left(t-\frac{1}{t}\right)\right], \qquad [4.7.3]$$

and again applying Eq. 4.3.8,

$$\sum_{\nu=-\infty}^{\infty} J_\nu(\alpha+\beta)\, t^\nu = \sum_{m=-\infty}^{\infty}\sum_{m'=-\infty}^{\infty} J_m(\alpha)\, J_{m'}(\beta)\, t^{m+m'}. \qquad [4.7.4]$$

Equation 4.7.1 is then obtained from Eq. 4.7.4 by equating coefficients of t^ν.

The algorithm based on the addition theorem results in an approximate solution for $\rho(x,z)$ denoted $\tilde{\rho}(x,z)$. The relationship between the calculated spin density $\tilde{\rho}(x,z)$ and the actual spin density $\rho(x,z)$ is a convolution with the point spread function h(x):

$$\tilde{\rho}(x,z) = \int \rho(x,z)\, h(x-x')\, dx' \ . \qquad [4.7.5]$$

Note that a reconstruction algorithm for which the calculated spin density is identical to the actual spin density occurs if and only if the point spread function h(x) is a delta function $\delta(x)$.

The equation describing the algorithm based on the addition theorem is:

$$\tilde{\rho}(x',z) = \sum_{m=-\infty}^{\infty} (-1)^m \rho'_m(z)\, J_m(k_x x') . \qquad [4.7.6]$$

In words, this algorithm reconstructs the spin density by first multiplying the individual partial spin densities by $(-1)^m J_m(k_x x')$ and then summing this product over all the acquired echoes. The evaluation of Eq. 4.7.6 begins by multiplying both sides of Eq. 4.3.17 by $(-1)^m J_m(k_x x')$ and summing over m,

$$\sum_{m=-\infty}^{\infty} (-1)^m \rho'_m(z)\, J_m(k_x x') = \sum_{m=-\infty}^{\infty} (-1)^m J_m(k_x x') \int_{x=-\infty}^{\infty} \rho(x,z)\, J_m(k_x x)\, dx . \qquad [4.7.7]$$

The left-hand side of Eq. 4.7.7 is $\tilde{\rho}(x',z)$; pulling the integral and the spin density out of the sum on the right-hand side,

$$\tilde{\rho}(x',z) = \int_{x=-\infty}^{\infty} \rho(x,z) \sum_{m=-\infty}^{\infty} J_m(k_x x)\, J_{-m}(k_x x')\, dx. \qquad [4.7.8]$$

Using Eq. 4.7.4 with $\nu = 0$,

$$\tilde{\rho}(x',z) = \int_{x=-\infty}^{\infty} \rho(x,z)\, J_0(\, k_x\, [x + x']\,)\, dx . \qquad [4.7.9]$$

Thus, the point-spread function for this reconstruction is $J_0(k_x x)$. (Recall that the Bessel function of order zero appears in Figure 4.3.1.) As an example, this algorithm is applied to determine $\tilde{\rho}(x,z)$ for the spin density of the square box in Figure 4.5.1. The infinite summation is approximated by summing over 128 acquired echoes. The ringing along x

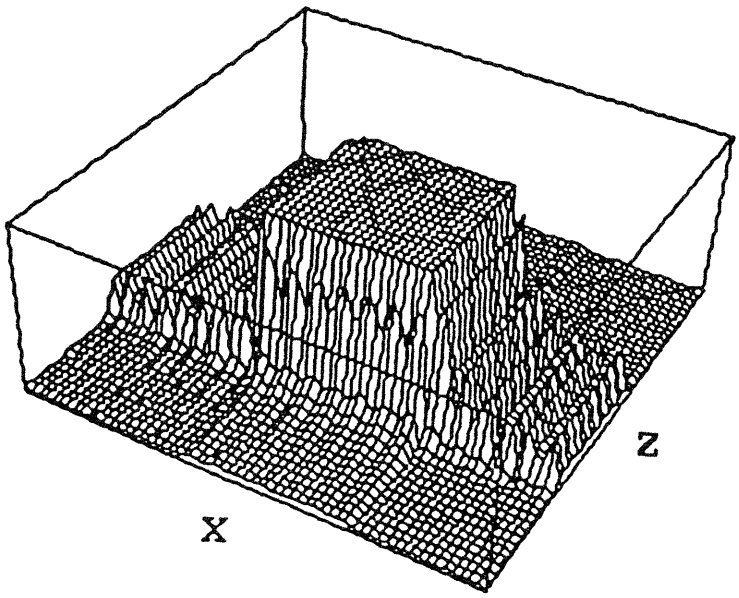

Figure 4.7.1 Preliminary reconstruction based on the addition theorem for Bessel functions. Note the severe ringing which makes this reconstruction algorithm unsatisfactory.

introduced by the point-spread function is illustrated in Figure 4.7.1. It is important to note that point-spread function includes the variable $k_x = \gamma g_x T$ and therefore depends on the parameters of the PERL field. Specifically, the point-spread function improves as the product $g_x T$ increases. Nevertheless, as seen in Eq. 4.7.9 the function $J_0(k_x x)$ is an unsatisfactory result, and Chapters 5 and 6 are devoted to dramatically improving the image reconstruction.

Section 4.8 Conclusions

This chapter introduces the PERL field and a pulse sequence implementing it to encode spatial information for MRI. The theoretical expression for the PERL signal is derived for this pulse sequence, and the limitations on image parameters imposed by experimental considerations are discussed. The most significant constraint links the penetration of the PERL field with the spacing between current elements required to create the field. This constraint leads to a second pulse sequence which incorporates phase encoding to relax the wavelength of the PERL field. Consequently, a relationship is established between penetration of the PERL field and the number of switches required in the pulse sequence. This relationship creates a new opportunity for MRI with the PERL encoding technology. Specifically, the relationship between the number of switches and the field of view offers a spectrum of pulse sequences which can be optimized for a particular imaging application. The image reconstruction is then introduced by illustrating the fundamental differences between Fourier encoding and the encoding using the PERL field. Finally, the reconstruction mathematics is outlined and an initial reconstruction is proposed. This example shows several of the fundamental differences between standard linear encoding gradients and the PERL encoding field.

Chapter 4 References

[1]Andrews, LC. *Special Functions for Engineers and Applied Mathematics*, Macmillan Publishing Company, New York, 1984, p. 195.
[2] J Spanier and KB Oldham, *An Atlas of Functions*, Harper and Row Publishers, Washington, 1987.
[3] Journal fur Math. XV. (1836), p.12.
[4] Neueste Schriften der Naturf. Ges. in Danzig, V. (1855), p.2.

CHAPTER 5. The PERL transform.

Section 5.1 Introduction and review

Chapter 4 introduced the new MRI technology using the PERL encoding field and began the discussion of image reconstruction. To elaborate on the reconstruction, three points must be emphasized.

1. The PERL signal S(t) is not related to the image spin density $\rho(x,z)$ by a 2DFT.
2. The spin echoes $S_m(t)$ and the partial spin densities $\rho'_m(z)$ are related by a 1DFT; thus, the z-component of the spin density is reconstructed by standard Fourier analysis.
3. The 2D reconstruction of $\rho(x,z)$ is separable in x and z. The x-component reconstruction reduces to Eq. 4.3.17, a one-dimensional integral in which the kernel is a Bessel function with an order corresponding to a specific number of the spin echo in the PERL signal.

Section 5.2 Derivation of the PERL transform

This chapter presents the 1D transform used to reconstruct the x-component of the spin density $\rho(x,z)$. Since the z-dependence is reconstructed by Fourier analysis, it can be removed from Eq. 4.3.17 leaving

$$\rho'_m = \int_{x=-\infty}^{\infty} \rho(x)\, J_m(k_x\, x)\, dx\,. \qquad [5.2.1]$$

Equation 5.2.1 is instrumental in understanding the PERL transform between the variables m and x. The goal of the reconstruction is to extract the unknown $\rho(x)$ from the known ρ'_m. Following the notation in Chapter 4, $\rho(x)$ represents the true x-component of the spin density, and $\tilde{\rho}(x)$ represents the calculated value of $\rho(x)$.

Extraction of $\rho(x)$ from Eq. 5.2.1 requires a set of functions which has the property of orthogonality with the function $J_m(k_x\, x)$ over m, the order of a Bessel

function. It is a common misconception that two Bessel functions $J_m(x)$ with different values of m are orthogonal.[1] This is not the case, as the orthogonality of Bessel functions is

$$\int_{x=0}^{1} x\, J_m(ax)\, J_m(bx)\, dx = 0 \qquad [5.2.2]$$

where a and b are zeros of $J_m(x)$ and $a \neq b$.

The proof of Eq. 5.2.2 begins with Bessel's equation,

$$x^2y'' + xy' + (x^2 - m^2)y = 0. \qquad [5.2.3]$$

Since $x(xy')' = x^2y'' + xy'$, Eq. 5.2.3 can be expressed as

$$x(xy')' + (x^2 - m^2)y = 0. \qquad [5.2.4]$$

Equation 5.2.4 is satisfied by $y = J_m(x)$, and replacing the argument x with ax yields

$$x(xy')' + (a^2x^2 - m^2)y = 0 \qquad [5.2.5]$$

since $x\frac{dy}{dx}$ becomes $ax\frac{dy}{d(ax)} = x\frac{dy}{dx}$ and the term $x(xy')'$ also remains unchanged.

Comparison with Bessel's equation shows that $J_m(ax)$ is a solution to Eq. 5.2.5. Similarly, $J_m(bx)$ is a solution to

$$x(xy')' + (b^2x^2 - m^2)y = 0. \qquad [5.2.6]$$

To simplify the subsequent equations, define $y_a \equiv J_m(ax)$ and $y_b \equiv J_m(bx)$. Then Eqs. 5.2.5 and 5.2.6 become

$$x(xy_a')' + (a^2x^2 - m^2)y_a = 0, \qquad [5.2.7]$$

$$x(xy_b')' + (b^2x^2 - m^2)y_b = 0. \qquad [5.2.8]$$

Multiplying Eq. 5.2.7 by y_b and Eq. 5.2.8 by y_a, subtracting the two equations, and canceling a factor of x yields

$$y_b(xy_a')' - y_a(xy_b')' + x\,y_a y_b(a^2 - b^2) = 0. \qquad [5.2.9]$$

Since $y_b(xy_a')' - y_a(xy_b')' = \frac{d}{dx}(y_b x y_a' - y_a x y_b')$, Eq. 5.2.9 may be integrated to

$$\left[y_b x y_a' - y_a x y_b'\right]_{x=0}^{x=1} + (a^2 - b^2)\int_{x=0}^{1} x\,y_a y_b\,dx = 0. \qquad [5.2.10]$$

Therefore, Eq. 5.2.10 is equivalent to Eq. 5.2.2 if $\left[y_b x y_a' - y_a x y_b'\right]_{x=0}^{x=1} = 0$. The evaluation at $x=1$ is zero since a and b are zeros of $J_m(x)$, and the evaluation at $x=0$ is also zero since the Bessel functions and their derivatives are finite.

Comparison of Eqs. 5.2.1 and 5.2.2 shows that the natural orthogonality of Bessel functions does not contribute to the solution for $\rho(x)$. Therefore, it is necessary to develop a set of functions from which the x-component of the spin density can be computed from the known values of ρ'_m. This set of functions is the basis functions for the PERL transform. The basis functions are termed $\phi_m(x)$ and satisfy the following two properties:

$$\int_{x=-\infty}^{\infty} \phi_m(x)\,J_{m'}(k_x x)\,dx = \delta_{mm'} \qquad [5.2.11]$$

$$\sum_{m=0}^{\infty} J_m(k_x x)\,\phi_m(x') = h(x-x') \qquad [5.2.12]$$

where $h(x-x')$ is the system function for obtaining $\rho(x)$ from ρ'_m, and $\delta_{mm'}$ is the standard Kronecker delta function. (Note that the functional form of $h(x-x')$ is evaluated in Section 4 of this chapter.)

The utility of the functions $\phi_m(x)$ in the reconstruction is appreciated by multiplying both sides of Eq. 5.2.1 by $\phi_m(x')$ and summing over m:

$$\sum_{m=0}^{\infty} \phi_m(x')\, \rho'_m = \sum_{m=0}^{\infty} \phi_m(x') \int_{x=-\infty}^{\infty} \rho(x)\, J_m(k_x\, x)\, dx. \qquad [5.2.13]$$

The summation of $\phi_m(x')$ can be moved into the integrand on the right-hand side since the integral is with respect to x. Then applying Eq. 5.2.12 and defining the result as $\tilde{\rho}(x)$,

$$\tilde{\rho}(x) = \sum_{m=0}^{\infty} \rho'_m\, \phi_m(x) = \rho * h \qquad [5.2.14]$$

where $\rho * h$ is the convolution of the functions $\rho(x)$ and $h(x)$. The process of obtaining $\tilde{\rho}(x)$ from ρ'_m via Eqs. 5.2.11-14 is called the PERL transform and is summarized in Figure 5.2.1. The inverse PERL transform is the calculation of ρ'_m from $\tilde{\rho}(x)$. It is derived by multiplying both sides of Eq. 5.2.14 by $J_m(k_x\, x)$, integrating with respect to x, and applying Eq. 5.2.11.

Section 5.3 The basis functions

Although the calculation of $\phi_m(x)$ is the focus of Chapter 6 the procedure is briefly outlined here. The functions $\phi_m(x)$ are obtained by expansion with a convenient basis set. For use in the reconstruction algorithm, the basis functions are spatially sampled at a distance corresponding to a desired spatial resolution in x. To obtain square pixels, the resolution in x and z are chosen to be identical. (The limits of resolution in the z-dimension are discussed in Chapter 4.) The expansion coefficients of the basis set are then calculated numerically. The resulting $\phi_m(x)$ for m=0, 25, and 50 are plotted in Figure 5.3.1 respectively.

Figure 5.3.1 suggests that the functions $\phi_m(x)$ have the property of spatial localization; specifically, $\phi_m(x) \approx 0$ in the region $|x| < \frac{m}{k_x}$, and the amplitude of the oscillations approaches zero for large x. (The functions $\phi_m(x)$ are not plotted for x<0, but in Chapter 6, $\phi_m(x)$ is shown to be an even function for m even and an odd function for m

$$\sum_{m=0}^{\infty} J_m(k_x\, x)\, \phi_m(x') = h(x-x')$$

$$\rho'_m = \int_{-\infty}^{\infty} \rho(x)\, J_m(k_x\, x)\, dx \qquad \begin{array}{c} \xrightarrow{\text{PERL Transform}} \\ \xleftarrow[\text{inverse PERL Transform}]{} \end{array} \qquad \tilde{\rho}(x) = \sum_{m=0}^{\infty} \rho'_m\, \phi_m(x)$$

$$\int_{-\infty}^{\infty} \phi_m(x)\, J_{m'}(k_x\, x)\, dx = \delta_{mm'}$$

Figure 5.2.1 The PERL transform between the variables m and x.

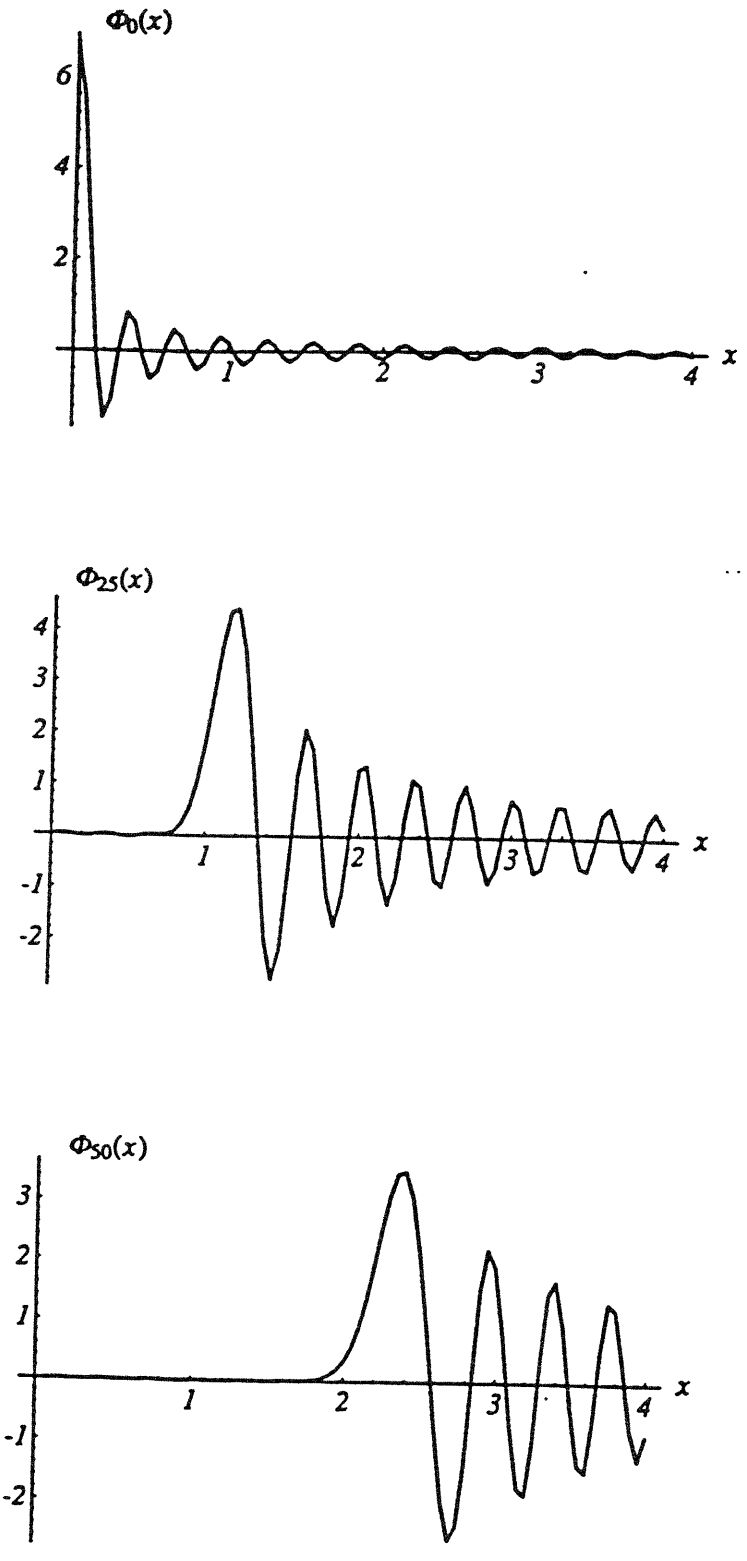

Figure 5.3.1 Plots of $\phi_m(x)$ for m = 0, 25, and 50 respectively.

odd.) Because of this property of $\phi_m(x)$, an arbitrary function f(x) defined in the domain $-L \le x \le L$ may be expanded with only those $\phi_m(x)$ for which $0 \le m \le k_x L$. As with a Fourier expansion, this expansion introduces a truncation error. However, the error in this expansion is introduced since $\phi_m(x)$ is not identically zero for $m > k_x L$. The error increases as $|x|$ approaches L, and it is rapidly reduced by increasing the number of functions incorporated into the expansion. That is, f(x) becomes

$$f(x) = \sum_{m=0}^{\infty} c_m \phi_m(x) \approx \sum_{m=0}^{M_{max}} c_m \phi_m(x) \qquad [5.3.1]$$

where c_m are the expansion coefficients and $M_{max} > k_x L$. Appendix 1 presents the relationship between the coefficients for a Fourier expansion of an arbitrary function and c_m, the coefficients of the expansion over the basis functions $\phi_m(x)$.

In the present imaging application, the FOV for the reconstruction of $\rho(x)$ is limited to [-L, L]. Therefore, the spatial localization of $\phi_m(x)$ sets an upper limit (M_{max}) on the number of terms required for an accurate expansion in Eq. 5.3.1. The experimental consequence is that M_{max} bounds the number of spin echoes which will contribute to the reconstruction of $\rho(x)$. For example, in the 2D simulations presented in Chapter 6, the FOV is [-2.0 cm, 2.0 cm] and $k_x \approx 22$. Therefore, at least 44 spin echoes must be acquired to accurately reconstruct the spin density. To reconstruct a larger FOV requires either a larger value of M_{max} or smaller k_x. As described below, a larger M_{max} is preferable since the point-spread function of the reconstruction improves as k_x increases.

Section 5.4 The system function

The usefulness of the PERL transform as a foundation for image reconstruction rests on the properties of the system function h(x-x'). (Note that in the context of the PERL transform, h(x-x') is termed the system function, and in the context of image reconstruction, the same function is termed the point-spread function.) Chapter 4

presents a first attempt at reconstruction based on the addition theorem for Bessel coefficients with a point-spread function of $J_0(k_x x)$. Equation 5.2.12 is the defining relationship for the system function h(x-x') in the PERL transform. To begin the evaluation of the system function, consider the plot of

$$h(x) = \sum_{m=0}^{M_{max}} g_m(x)\, \phi_m(0) \qquad [5.4.1]$$

in Figure 5.4.1. As mentioned above and detailed in Chapter 6, the expansion coefficients of $\phi_m(x)$ are computed numerically, making it impossible to analytically prove the functional form of h(x-x'). However, Figure 5.4.1 resembles the function

$$\frac{\sin(k_x x)}{\pi x} \qquad [5.4.2]$$

where, as before, $k_x = \gamma g_x T$. The difference between the two functions,

$$\text{diff}(x) = h(x) - \frac{\sin(k_x x)}{\pi x} \qquad [5.4.3]$$

is plotted on a magnified scale over the interval [-0.5, 0.5] in Figure 5.4.2.

Figures 5.4.1 and 5.4.2 suggests that h(x-x') has the form

$$h(x-x') = \sum_{m=0}^{\infty} g_m(x)\, \phi_m(x') = \frac{\sin[k_x (x - x')]}{\pi (x - x')}. \qquad [5.4.4]$$

This hypothesis is tested by comparing the two functions

$$h_{expt}(x-x') = \sum_{m=0}^{M_{max}=51} g_m(x)\, \phi_m(x') \qquad [5.4.5]$$

$$h_{hypo}(x-x') = \frac{\sin[k_x (x - x')]}{\pi (x - x')} \qquad [5.4.6]$$

for values of x and x' in increments of 0.1 over the interval [-2.0, 2.0]. In this range, the difference between $h_{expt}(x-x')$ and $h_{hypo}(x-x')$ is less than 0.5% of full scale with the maximum error occurring at the edges, numerically confirming the hypothesis in Eq. 5.4.4. In addition, h(x-x') is numerically shown to depend only on the difference x-x'

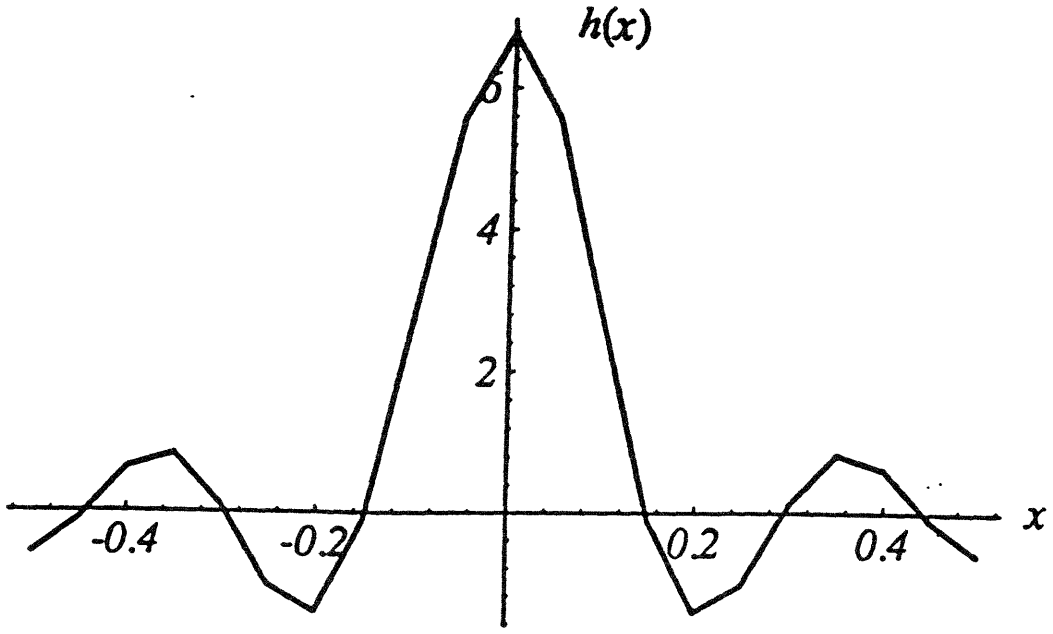

Figure 5.4.1. The system function centered at x'=0 computed from the basis functions $\phi_m(x)$. $M_{max} = 51$, and the separation between points along x is 0.05.

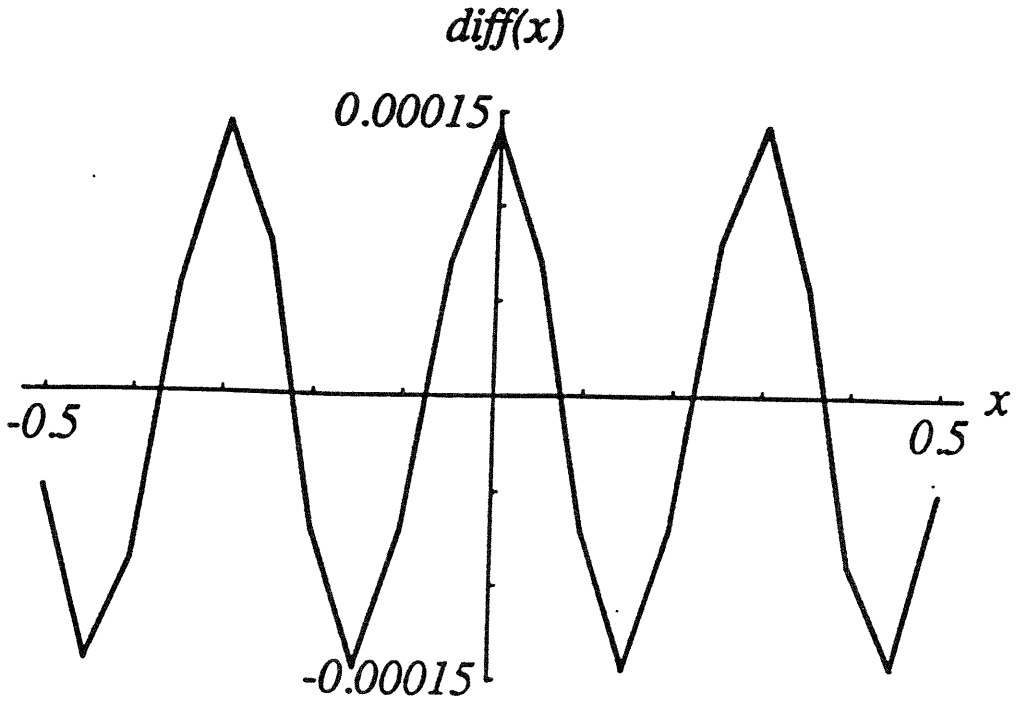

Figure 5.4.2. The function diff(x) as defined in the text.

over [-2.0, 2.0]. Therefore, the system function of the PERL transform it is written h(x) in the remainder of the text. This evaluation of the system function has fundamental consequences for imaging with the PERL encoding field. First, it demonstrates that the PERL technology has the potential to produce useful images for medical diagnoses. Second, it lends physical insight to the defining parameters of the PERL field. As mentioned above, in the 2D image reconstruction, h(x) becomes the point-spread function in the x-dimension for the reconstruction of $\rho(x)$. (This is verified in Chapter 6; the PERL signal from a delta function input is calculated, and this signal becomes the input for the reconstruction algorithm. The reconstruction in the x-dimension matches Figure 5.4.1). Since the point-spread function has the form of a sinc function, its behavior is well known. As the value of k_x becomes large, h(x) approaches $\delta(x)$. Recall that $k_x = \gamma g_x T$, implying that the point-spread function improves as the product $g_x T$ increases. This means that the image reconstruction becomes more ideal as the product of the amplitude of the PERL field and its duration in the pulse sequence increases.

Section 5.5 Conclusions

The goal of this chapter is to define and characterize the PERL transform. The PERL transform over the variables m and x is a set of equations which reconstructs the x-component of the spin density after spatial encoding with the PERL field. The PERL transform is defined in Figure 5.2.1, and it is characterized in four steps. The first step shows mathematically that the reconstruction requires a new set of basis functions $\phi_m(x)$ which are orthogonal to Bessel functions over their order m. The second step discusses the properties of $\phi_m(x)$. Most importantly, $\phi_m(x)$ is spatially localized, and an arbitrary function may be expanded with a basis set $\phi_m(x)$ in a manner similar to a Fourier series expansion. In fact, Appendix 1 presents the relationship between the coefficients for a Fourier expansion of an arbitrary function and the coefficients of the expansion over $\phi_m(x)$. The third step implements $\phi_m(x)$ into a reconstruction procedure in which the

calculated spin density is the convolution of the actual spin density and a point-spread function. The final step computes the functional form of the point-spread function and describes its dependence on the parameters defining the PERL field.

Chapter 5 References

[1] Boas ML. *Mathematical Methods in the Physical Sciences,* 2nd Ed. John Wiley and Sons, 1983.

Chapter 6. The reconstruction algorithm.

Section 6.1. Introduction

This chapter applies the PERL transform developed in Chapter 5 to a reconstruction algorithm for the x-dimension of this spin density after encoding with the PERL field. The reconstruction is a two step process. The first step includes a method to calculate the functions $\phi_m(x)$ via Eqs. 5.2.11-12, and the second part incorporates $\phi_m(x)$ into an algorithm based on the PERL transform. As described in Chapter 5, a closed-form solution for $\phi_m(x)$ has not been obtained; thus, $\phi_m(x)$ is expanded over a set of functions, and the expansion coefficients are obtained with techniques of linear algebra. The choice of expansion functions leads to a stable solution for the expansion coefficients and lends insight to the PERL encoding technology. The reconstruction algorithm is then tested for two sample spin densities, and the reconstruction along x (PERL) is comparable to the reconstruction along z (Fourier). To illustrate the robustness of the algorithm, the reconstruction is also performed in the presence of Gaussian noise.

Section 6.2. Theory

The computations in this chapter assume that the PERL signal is acquired from data sampled at the Nyquist sampling rate, and if phase encoding steps are incorporated into the pulse sequence, they are decoded to produce the individual $S_m(t)$ echoes. Briefly reviewing earlier results which are relevant to this discussion, the PERL signal is a series of spin echoes $S_m(t)$ which are related to $\rho'_m(z)$, the partial spin density, by a 1DFT. That is, the z-component of the spin density is reconstructed by standard Fourier analysis since it is linearly encoded. However, the 2D reconstruction of $\rho(x,z)$ is separable in x and z, and the x-component reconstruction problem reduces to a one-dimensional integral (Eq. 4.3.17) in which the kernel is a Bessel function with an order corresponding to a specific number of the spin echo in the PERL signal. The calculation of the x-component of

$\rho(x,z)$ from the known values of $\rho'_m(z)$ is the definition of the PERL transform. (See Figure 5.2.1.)

Chapter 5 includes a discussion of the relationship between M_{max} (the number of spin echoes which must be acquired), the FOV, and the parameter k_x. Specifically, $M_{max} > k_x FOV_x$, and the present discussion assumes this criteria has been met and data from M+1 spin echoes is collected for $t \geq 0$. Consequently, Eq. 5.2.14 becomes

$$\tilde{\rho}(x) = \sum_{m=0}^{M} \rho'_m \phi_m(x). \qquad [6.2.1]$$

The first step of the reconstruction algorithm is to obtain the functions $\phi_m(x)$. Chapter 5 details the natural orthogonality of Bessel functions (Eq. 5.2.2) and shows the difficulty in implementing this property to the reconstruction. Thus, the basis functions $\phi_m(x)$ are created to satisfy Eqs. 5.2.11 and 5.2.12, but a closed form solution for $\phi_m(x)$ has not been obtained. Consequently, these functions are calculated by the expansion

$$\phi_m(x) = \sum_{n=0}^{M} \alpha_{nm} \frac{1}{x} J_{n+1}(k_x x). \qquad [6.2.2]$$

Throughout this chapter the expansion functions are written as $f_n(x)$ for convenience; that is

$$f_n(x) \equiv \frac{1}{x} J_{n+1}(k_x x). \qquad [6.2.3]$$

Expansions of a generalized function over a series of Bessel functions were first investigated by Webb[1] and have been discussed by Kapteyn[2] and Bateman.[3]

The expansion functions $f_n(x)$ have three properties which are incorporated into the reconstruction algorithm. First, $f_n(x)$ is an even function for n even and an odd function for n odd. This is understood by combining Eqs. 4.3.11 and 4.3.14 to give the

result $J_n(-a) = (-1)^n J_n(a)$ and noting that the function x^{-1} is odd. Second, the functions $f_n(x)$, like the functions $\phi_m(x)$, have the property of spatial localization. Specifically, $f_n(x) \approx 0$ for $|x| < n/k_x$, and therefore the expansion in Eq. 6.2.2 includes $f_n(x)$ for values of n between zero and M. The third property of the functions $f_n(x)$ is their relationship with the functions $J_{m'}(k_x x)$. Ideally, the expansion functions would be orthogonal to $J_{m'}(k_x x)$ over the order of the Bessel functions, implying that the coefficients α_{nm} in Eq. 6.2.2 would be nonzero only when n = m. (If this were the case, $f_n(x)$ and $\phi_m(x)$ would differ by at most a scaling factor.) This type of orthogonality does not hold for $f_n(x)$, but the relationship between $J_{m'}(k_x x)$ an the expansion functions is:

$$b_{m'n} \equiv \int_{x=-\infty}^{\infty} J_{m'}(k_x x)\, f_n(x)\, dx = \frac{4}{\pi} \frac{\sin \frac{\pi}{2}[m' - (n+1)]}{m'^2 - (n+1)^2}. \qquad [6.2.4]$$

Since the proof of Equation 6.2.4 is quite lengthy, the reader is referred to Watson.[4]

Returning to the expansion for $\phi_m(x)$, Eq. 6.2.2 is substituted into 5.2.11 to yield

$$\delta_{mm'} = \int_{x=-\infty}^{\infty} \sum_{n=0}^{M} \alpha_{nm} f_n(x)\, J_{m'}(k_x x)\, dx = \sum_{n=0}^{M} \alpha_{nm} \int_{-\infty}^{\infty} f_n(x) J_{m'}(k_x x)\, dx$$

$$= \sum_{n=0}^{M} b_{m'n}\, \alpha_{nm}. \qquad [6.2.5]$$

where $b_{m'n}$ is given by Eq. 6.2.4. This analysis provides a simple method to calculate the expansion coefficients in Eq. 6.2.2 and therefore obtain the functions $\phi_m(x)$. As seen below, this procedure not only leads directly to the reconstruction algorithm, but also provides insight into how the PERL field encodes spatial information.

The expression $\delta_{mm'} = \sum_{n=0}^{M} b_{m'n}\, \alpha_{nm}$ in Eq. 6.2.5 may be recast into matrix notation

$$\bar{\bar{I}} = \bar{\bar{B}}\, \bar{\bar{A}} \qquad [6.2.6]$$

where $\bar{\bar{I}}$ is the identity matrix, the matrix elements of $\bar{\bar{A}}$ are the expansion coefficients α_{nm}, and the matrix elements of $\bar{\bar{B}}$ are $b_{m'n}$ as defined in Eq. 6.2.4. Therefore, the expansion coefficients are obtained by inverting $\bar{\bar{B}}$ to solve for $\bar{\bar{A}}$:

$$\bar{\bar{A}} = \bar{\bar{B}}^{-1}. \qquad [6.2.7]$$

Since the matrix elements of $\bar{\bar{B}}$ obey the rules

$$\left\{ \begin{array}{c} b_{m'n} = 0 \text{ for m' even, n odd} \\ b_{m'n} = 0 \text{ for m' odd, n even} \\ b_{m'n} \neq 0 \text{ otherwise} \end{array} \right\},$$

the matrix assumes the form

$$\bar{\bar{B}} = \begin{bmatrix} b_{00} & 0 & b_{02} & 0 & \cdots & b_{0M} \\ 0 & b_{11} & 0 & b_{13} & \cdots & 0 \\ b_{20} & 0 & b_{22} & 0 & \cdots & b_{2M} \\ 0 & b_{31} & 0 & b_{33} & \cdots & 0 \\ \cdots & \cdots & \cdots & \cdots & \cdots & \cdots \\ b_{M0} & 0 & b_{M2} & 0 & \cdots & b_{MM} \end{bmatrix}. \qquad [6.2.8]$$

As noted earlier in this chapter, the ideal expansion functions in Eq. 6.2.2 would be orthogonal to $J_{m'}(k_x x)$ over the order of the Bessel functions. If this were the case, the matrices $\bar{\bar{A}}$ and $\bar{\bar{B}}$ would be diagonal, implying that α_{nm} would be nonzero only when $n = m$ and $\alpha_{nm} = (b_{m'n})^{-1}$. Although this property can not realized, choosing the basis functions $f_n(x)$ ensures that half the elements of $\bar{\bar{B}}$ are zero. At first glance, this property may not suggest a computational advantage: Eq. 6.2.8 appears difficult to implement since in this form $\bar{\bar{B}}$ may be ill-conditioned or singular.[5] However, a procedure is developed below in which the calculation of $\bar{\bar{B}}^{-1}$ (and therefore α_{nm}) is greatly simplified by the form of Eq. 6.2.8.

The first step of this procedure is to exchange several rows and columns of $\bar{\bar{B}}$ until it assumes the form

$$\bar{\bar{B}} = \begin{bmatrix} \bar{\bar{B}}^{\text{even}} & 0 \\ 0 & \bar{\bar{B}}^{\text{odd}} \end{bmatrix}. \qquad [6.2.9]$$

The elements of $\overline{\overline{B}}^{even}$ and $\overline{\overline{B}}^{odd}$ are defined as follows:

$$b_{m'n}^{odd} = b_{2m'+1,\,2n+1}\ ;\ m',n = 0,1,2,\ldots,\ \frac{M}{2}, \qquad [6.2.10]$$

and

$$b_{m'n}^{even} = b_{2m',\,2n}\ ;\ m',n = 0,1,2,\ldots,\ \frac{M}{2}. \qquad [6.2.11]$$

To illustrate the specific row and column exchanges required to obtain the form in Eq. 6.2.9, the sequence is performed on a 4x4 example matrix

$$\begin{bmatrix} b_{00} & 0 & b_{02} & 0 \\ 0 & b_{11} & 0 & b_{13} \\ b_{20} & 0 & b_{22} & 0 \\ 0 & b_{31} & 0 & b_{33} \end{bmatrix}. \qquad [6.2.12]$$

In this simple case, two exchanges are necessary. The first step exchanges the second and third rows to yield

$$\begin{bmatrix} b_{00} & 0 & b_{02} & 0 \\ b_{20} & 0 & b_{22} & 0 \\ 0 & b_{11} & 0 & b_{13} \\ 0 & b_{31} & 0 & b_{33} \end{bmatrix}. \qquad [6.2.13]$$

The second step exchanges the second and third columns, giving the desired result

$$\begin{bmatrix} b_{00} & b_{02} & & \\ b_{20} & b_{22} & \multicolumn{2}{c}{0} \\ & & & \\ \multicolumn{2}{c}{0} & b_{11} & b_{13} \\ & & b_{31} & b_{33} \end{bmatrix}. \qquad [6.2.14]$$

Larger matrices are converted to the matrix form in Eq. 6.2.9 by extending the above sequence.

The form of $\overline{\overline{B}}$ in Eq. 6.2.9 suggests a theorem of linear algebra to simplify the calculations of α_{nm}:

$$\begin{bmatrix} \overline{\overline{X}} & 0 \\ 0 & \overline{\overline{Y}} \end{bmatrix}^{-1} = \begin{bmatrix} \overline{\overline{X}}^{-1} & 0 \\ 0 & \overline{\overline{Y}}^{-1} \end{bmatrix}. \qquad [6.2.15]$$

where $\overline{\overline{X}}$ and $\overline{\overline{Y}}$ are matrices with equal dimensions. The proof of Eq. 6.2.15 utilizes several properties of linear algebra which have not been developed in this thesis, and consequently the reader is referred to Strang.[6]

Applying this theorem to Eqs. 6.2.7 and 6.2.9, the matrix $\overline{\overline{A}}$, composed of the expansion coefficients α_{nm}, assumes the form

$$\overline{\overline{A}} = \begin{bmatrix} \overline{\overline{E}} & \underline{0} \\ 0 & \overline{\overline{O}} \end{bmatrix} \qquad [6.2.16]$$

where $\overline{\overline{E}} \equiv \left(\overline{\overline{B}}^{even}\right)^{-1}$ and $\overline{\overline{O}} \equiv \left(\overline{\overline{B}}^{odd}\right)^{-1}$. From this it follows directly that the expansion coefficients α_{nm} obey the conditions:

$$\left\{ \begin{array}{c} \alpha_{nm} = 0 \text{ for n even, m odd} \\ \alpha_{nm} = 0 \text{ for n odd, m even} \\ \alpha_{nm} \neq 0 \text{ otherwise} \end{array} \right\}.$$

Combined with the parity of the functions $f_n(x)$ described above, this property of α_{nm} proves that $\phi_m(x)$ is an even function for m even and an odd function for m odd. Therefore, $\phi_m(x)$ can be decomposed into two functions:

$$\phi_{2m}^{even}(x) = \sum_{n=0}^{M/2} e_{nm} f_{2n}(x) \qquad [6.2.17]$$

where e_{nm} are the elements of $\overline{\overline{E}}$, and

$$\phi_{2m+1}^{odd}(x) = \sum_{n=0}^{M/2} o_{nm} f_{2n+1}(x) \qquad [6.2.18]$$

where o_{nm} are the elements of $\overline{\overline{O}}$.

Equations 6.2.17 and 6.2.18 offer an opportunity to gain valuable intuition about the PERL encoding field. Because $\phi_m(x)$ can be decomposed into the functions $\phi_{2m}^{even}(x)$ and $\phi_{2m+1}^{odd}(x)$, the x-component of the spin density can be reconstructed in two pieces: $\tilde{\rho}^{even}(x)$ and $\tilde{\rho}^{odd}(x)$. The functional form of $\tilde{\rho}^{even}(x)$ and $\tilde{\rho}^{odd}(x)$ follows directly from

Eq. 6.2.1, and the properties of these two expressions are derived from the basis functions $\phi_m(x)$. $\tilde{\rho}^{even}(x)$ is an even function in x defined as the sum of the terms $\rho'_m \phi_m^{even}(x)$ for even values of m. $\tilde{\rho}^{odd}(x)$ is an odd function in x defined as the sum of the terms $\rho'_m \phi_m^{odd}(x)$ for odd values of m. The two reconstruction pieces are expressed as follows:

$$\tilde{\rho}^{even}(x) = \sum_{m=0}^{M/2} \rho'_{2m} \phi_{2m}^{even}(x) \qquad [6.2.19]$$

$$\tilde{\rho}^{odd}(x) = \sum_{m=0}^{M/2} \rho'_{2m+1} \phi_{2m+1}^{odd}(x). \qquad [6.2.20]$$

There are three direct consequences of the reconstruction algorithm.

1. The PERL field separates the image spin density into its even and odd components with respect to x. (Recall that ρ'_m represents the z-component of the spin density which is calculated by a 1DFT of the spin echoes.) Therefore, the m-even spin echoes provide the information to reconstruct $\rho^{even}(x)$, and the m-odd spin echoes are used to reconstruct $\rho^{odd}(x)$.

2. The separation of $\tilde{\rho}(x)$ into even and odd components has a positive impact on the reconstruction since the size of the matrices required in the algorithm is reduced by a factor of two.

3. The functions $\phi_m(x)$ (which form the foundation of the PERL transform) do not need to be calculated for each image reconstruction. These functions are a direct consequence of the PERL encoding field and may be hard-wired into the reconstruction algorithm software.

Section 6.3 Computer simulations

This chapter now turns from a theoretical discussion of image reconstruction to testing by computer simulation. Results are presented from several experiments. The

reconstructions are simulated by assuming a known spin density and calculating the PERL signal via Eq. 4.3.2. The signal becomes the input to the algorithm, and the reconstruction output is compared to the known spin density.

As discussed in Chapter 5, a 1D reconstruction along x for a 'delta' input $\delta(x)$ is expected to yield the point-spread function h(x). The input for this 1D reconstruction appears in Figure 6.3.1. The reconstructed function, $h_{recon}(x)$, appears in Figure 6.3.2 and comparison with Figure 5.4.1 again confirms the hypothesis of the form of the point-spread function in Eq. 5.4.4.

In the 2D reconstructions, Eqs. 6.2.19 and 6.2.20 are recast into two systems of linear equations $\overline{\overline{P}}^e = \overline{\overline{Q}}^e \overline{\overline{R}}^e$ and $\overline{\overline{P}}^o = \overline{\overline{Q}}^o \overline{\overline{R}}^o$ where the matrices $\overline{\overline{P}}$, $\overline{\overline{Q}}$, and $\overline{\overline{R}}$ represent $\tilde{\rho}(x,z)$, $\rho'_m(z)$, and $\phi_m(x)$ respectively. $\overline{\overline{Q}}$ and $\overline{\overline{R}}$ are constructed by the procedures outlined below, and $\overline{\overline{P}}$ is obtained by a matrix multiplication of $\overline{\overline{Q}}$ and $\overline{\overline{R}}$.

<u>To obtain</u> $\overline{\overline{Q}}$. The spin echoes $S_m(t)$ are first sampled in time by the Nyquist criteria, and a discrete form of $\rho'_m(z)$ is then computed by an inverse 1DFT of $S_m(t)$. Each row of $\overline{\overline{Q}}$ corresponds to $\rho'_m(z)$ for a specific m.

<u>To obtain</u> $\overline{\overline{R}}$. The discrete form of the functions $\phi_m(x)$ are obtained by the method detailed above. Each column of $\overline{\overline{R}}$ corresponds to $\phi_m(x)$ for a specific m.

The resolution along x is denoted dx; as discussed in Chapter 4, dx is fixed by the parameters of the pulse sequence (Figure 4.2.1). To obtain square pixels in the image display, the linear gradient is applied so that the resolution along z (the Fourier direction) matches dx, or dz=dx.

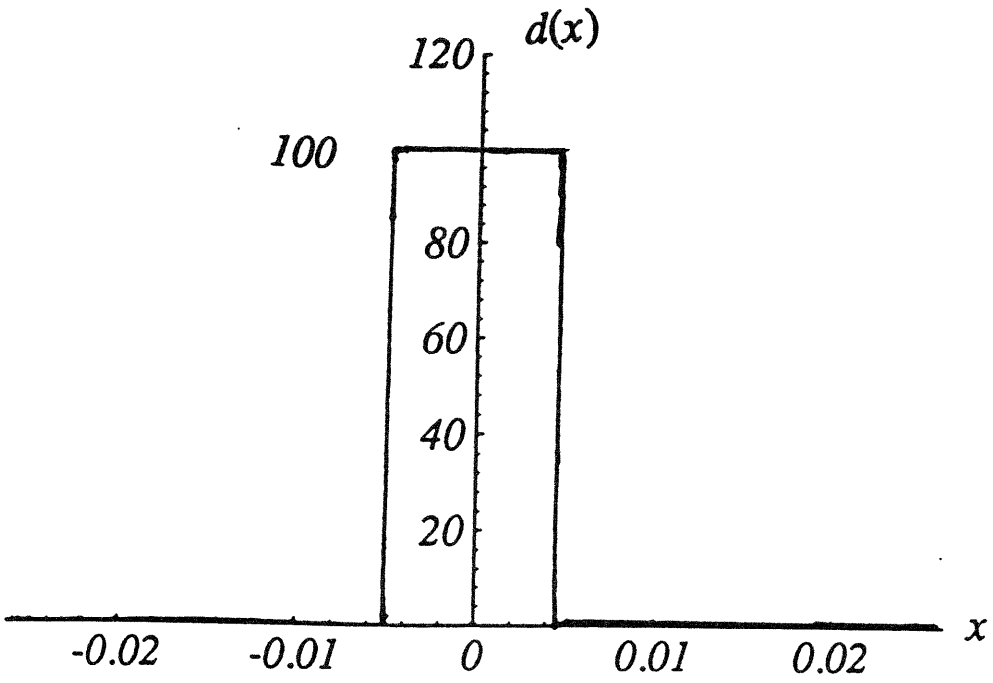

Figure 6.3.1. One dimensional rectangular input having width 0.01 cm and centered at the origin (x'=0). This function approximates $\delta(x)$.

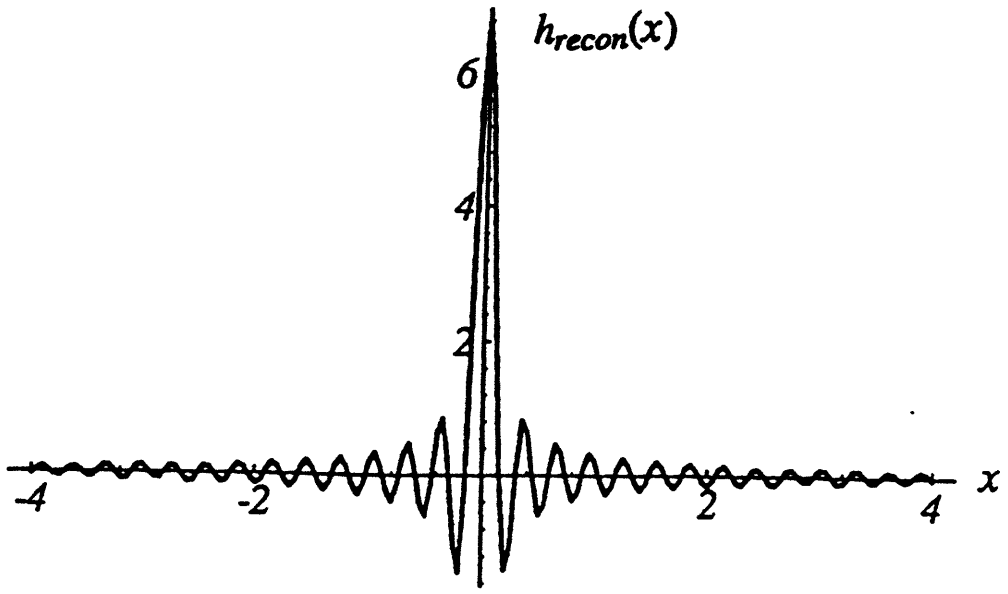

Figure 6.3.2 Reconstruction of function approximating δ(x). Compare with the form of h(x-x').

The system parameters chosen for the algorithm are given in Table 6.3.1. For this system, dz=dx=0.12cm , the pixel width in the 2D simulations. In Figures 6.3.3 and 6.3.4, the x and z axes are numbered by pixel number. In these plots, pixel 33 corresponds to either x=0 or z=0.

The input spin density in Figure 6.3.3 is a box in the first quadrant with dimensions 2.0 cm x 2.0 cm. Figure 6.3.4 is the reconstructed spin density $\tilde{\rho}(x,z)$. In Figure 6.3.5, the assumed spin density $\rho(x,z)$ is two square objects on a rectangular pedestal. The reconstructed function $\tilde{\rho}(x,z)$ appears in Figure 6.3.6.

The results from these simulations are quite satisfying: the ringing along x (PERL) is comparable to the ringing along z (Fourier). However, in these simulations the signal produced by the initial spin densities is uniform. Thus, these results do not provide information about the reconstruction in the presence of random fluctuations in the signal. To demonstrate the robustness of the reconstruction, the spin density in Figure 6.3.3 is reconstructed in the presence of zero mean Gaussian noise of maximum amplitude 0.1. The assumed spin density appears in Figure 6.3.7; the reconstructed spin density appears in Figure 6.3.8. In these two figures several rows of pixels near the edges are set to zero for convenience in data storage and printing. Additional properties of the reconstruction algorithm in the presence of noise (such as the noise-power spectrum) have not been investigated and are proposed for future work.

Section 6.4 Conclusions

This chapter is divided into two parts. Section 6.2 illustrates the calculation of the basis functions $\phi_m(x)$ and their incorporation into the reconstruction algorithm, and Section 6.3 presents computer simulations of the algorithm. In Section 6.2 the basis functions of the PERL transform are calculated by an expansion over the functions

PARAMETER	PHYSICAL MEANING	VALUE
G_z	magnitude of B_z, the linear gradient during data aquisition	2.4 G/cm
g_x	magnitude of x-component of the PERL field	1.0 G/cm
g_z	frequency of oscillating component of the PERL field	20 π rad/cm
T	duration of the PERL field	5 msec
nsam	number of samples obtained from each spin-echo	128
SI	time between samples	0.04 msec

Table 6.3.1. Parameters used in 2D reconstruction algorithm.

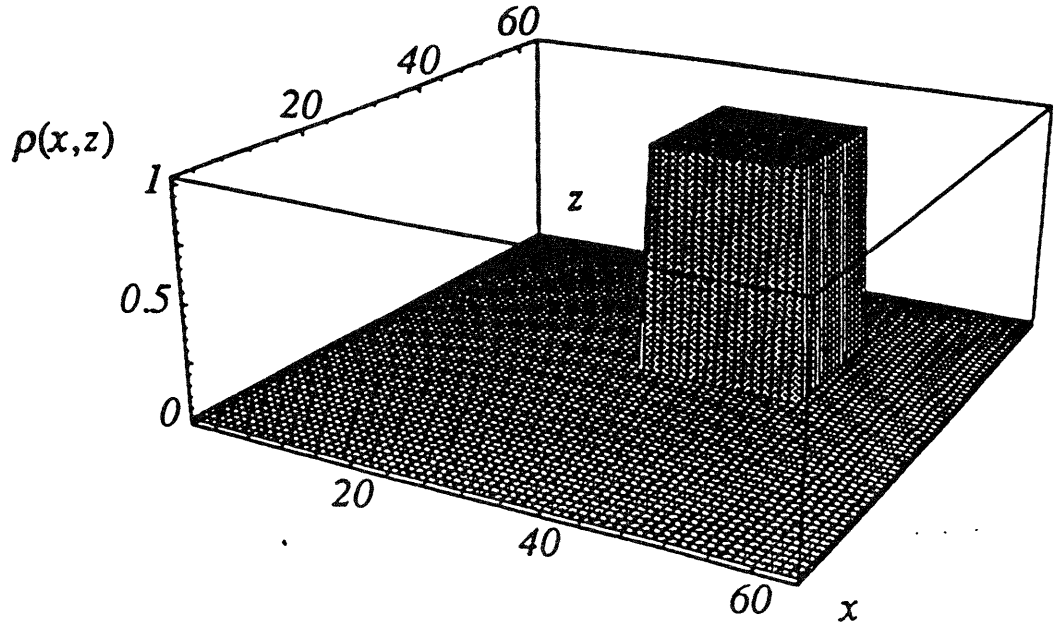

Figure 6.3.3 Input spin density equal to one in the square region between zero and two in both the x and z dimensions. The axes are labeled by pixel number. The origin is at pixel (33,33), and the pixel dimensions are 0.12 cm square.

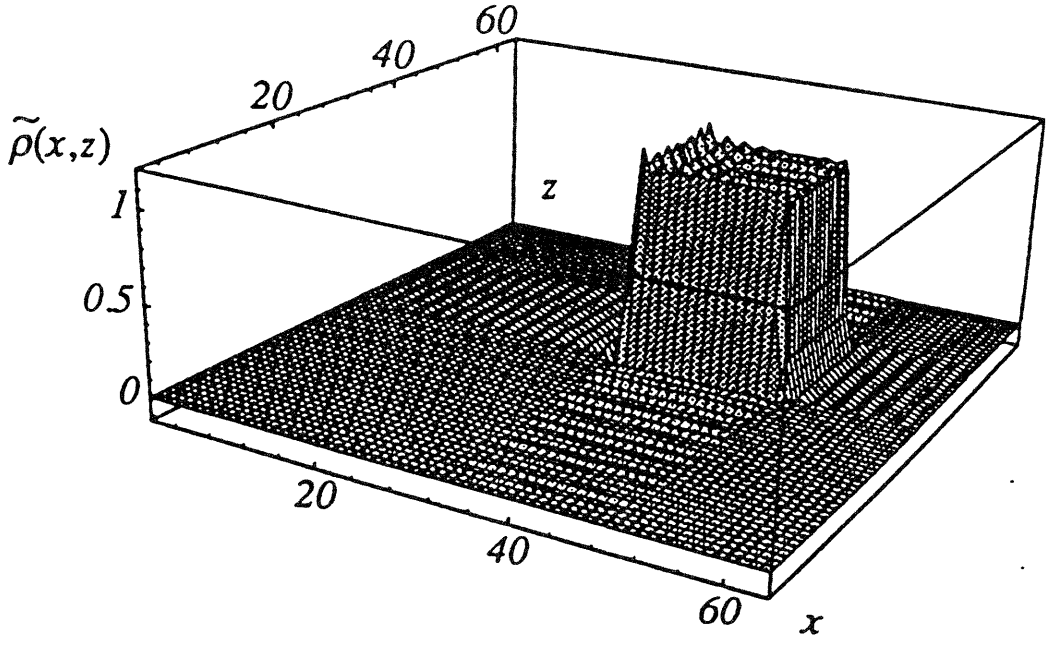

Figure 6.3.4 Reconstructed spin density. Note the ringing along x (Fourier) is comparable to the ringing along z (PERL).

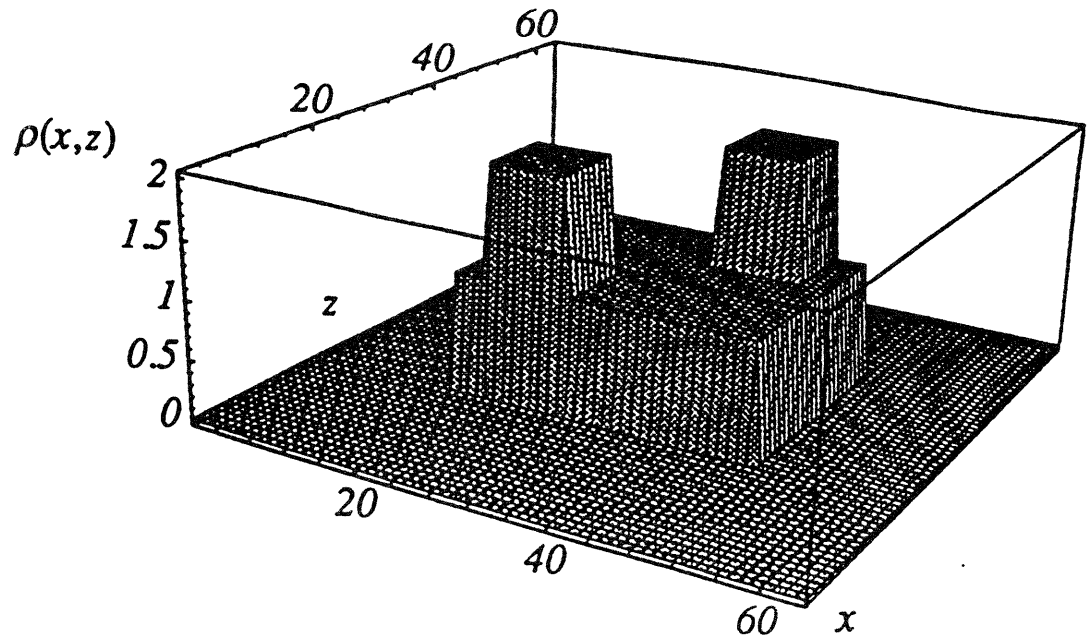

Figure 6.3.5 Nonuniform input spin density. The axes are labeled by pixel number. The origin is at pixel (33,33), and the pixel dimensions are 0.12 cm square.

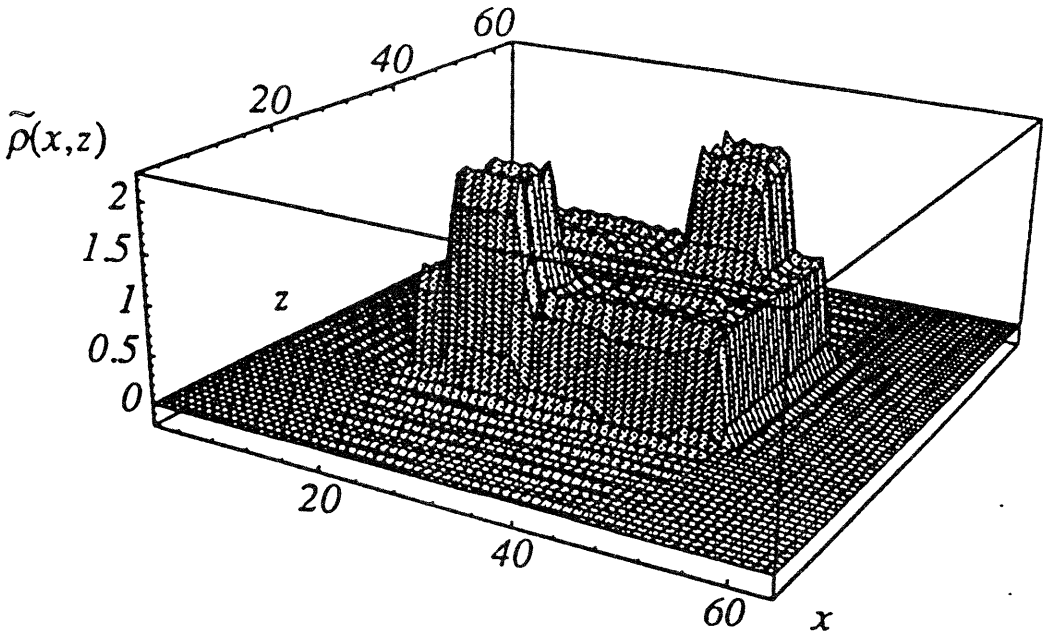

Figure 6.3.6 Reconstruction of nonuniform spin density.

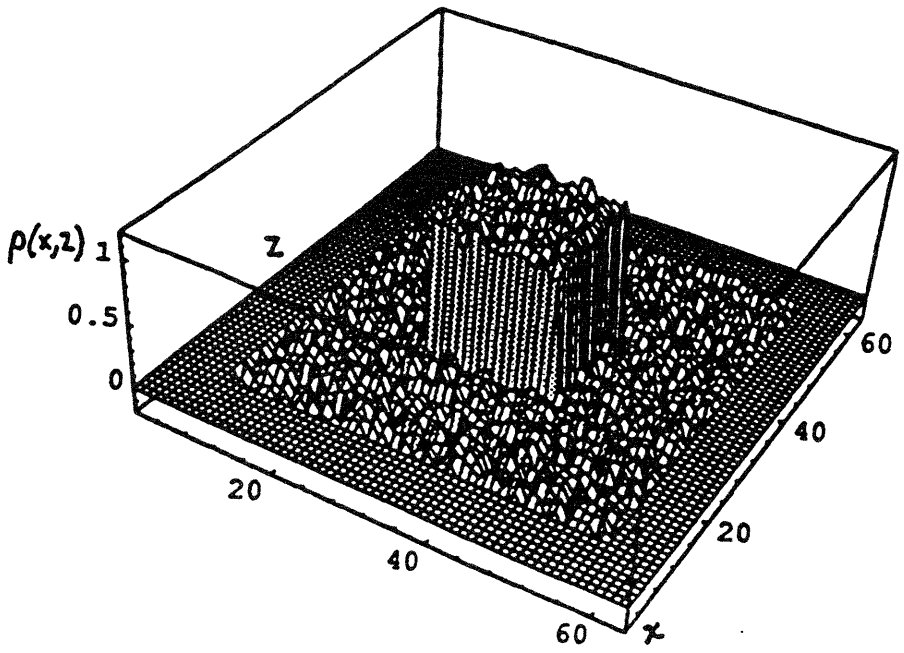

Figure 6.3.7 Input spin density identical to square box between zero and two in both the x and z dimensions with the addition of zero mean Gaussian noise of maximum amplitude 0.1. The origin is at pixel (33,33), and the pixel dimensions are 0.12 cm square.

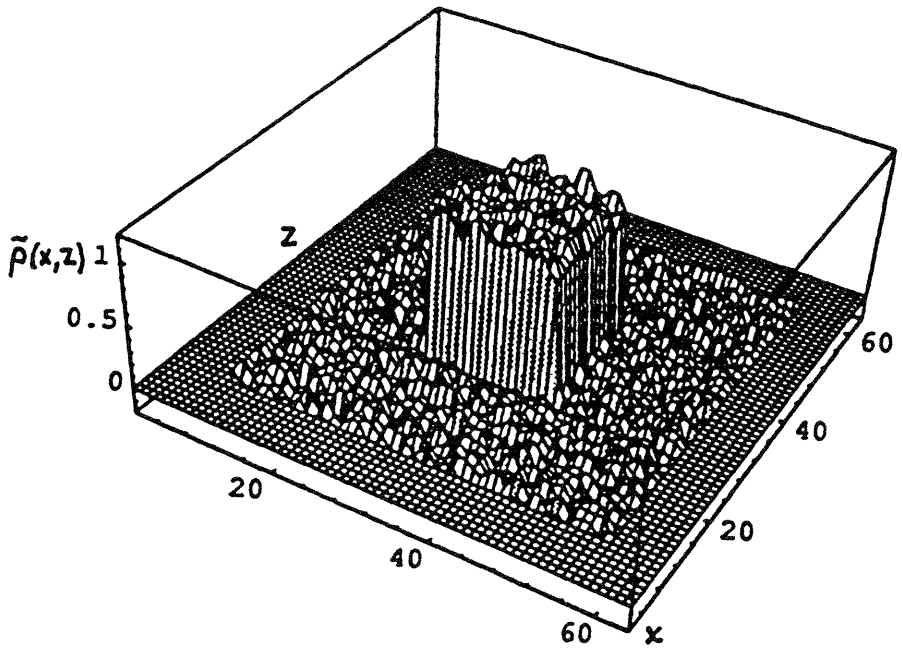

Figure 6.3.8 Reconstruction of spin density in the presence of noise.

$f_n(x) \equiv J_{n+1}(k_x x)/x$. This expansion is recast into a matrix problem, and the expansion coefficients are calculated by a matrix inversion. The matrix of expansion coefficients is inherently ill-conditioned, but a stable solution is obtained by methods of linear algebra. This solution lends insight to the PERL encoding technology. In Section 6.3 the reconstruction algorithm is tested for two sample spin densities, and the reconstruction along x (PERL) is comparable to the reconstruction along z (Fourier). To illustrate the robustness of the algorithm, the reconstruction for one of the sample spin densities is repeated in the presence of Gaussian noise.

Chapter 6 References

[1] HA Webb, Messenger of Mathematics 33, 55 (1904).
[2] W Kapteyn, Messenger of Mathematics 35, 122 (1906).
[3] H Bateman, Messenger of Mathematics 36, 31 (1907).
[4] GN Watson, *A Treatise on the Theory of Bessel Functions*, University Press, Cambridge, 1948. (p. 404)
[5] G Strang, *Linear Algebra and its Applications*, 3rd Edition. Harcourt Brace Jovanovich, San Diego, 1988. (p. 363)
[6] G Strang, *Linear Algebra and its Applications*, 3rd Edition. Harcourt Brace Jovanovich, San Diego, 1988. (p. 42)

Chapter 7. PERL coil design.

Section 7.1 Introduction

This chapter illustrates the method[1,2] used to design a cylindrical magnetic field gradient coil from a desired field which is termed the "target field". In Chapter 8, the method is applied to a form of the PERL field to yield the actual current density of the cylindrical coil used to produce the field. The analysis is divided into six steps corresponding to Sections 7.2-7 in this chapter.

Since the mathematics in this chapter becomes quite detailed, the calculations in Sections 7.2-6 are summarized in steps below. This summary can be used as either an introduction to the mathematics or a replacement of these sections if the reader is not interested in the mathematical detail. The results of this chapter which are used in the PERL coil specifications appear in Section 7.7.

Outline of Sections 7.2-6:

I. Compute the expression for the vector potential within the coil volume in cylindrical coordinates. The coordinate system is illustrated in Figure 7.2.1. This equation is an integral whose integrand includes the current density. The phi component of the current density is written $j_\varphi(\varphi,z)$, and the z-component is written $j_z(\varphi,z)$. (Since the current is constrained to a surface, the current density is expressed in units of current per unit length.)

II. Simplify the expressions for the vector potential by noting that current does not flow in the radial direction of the cylinder, and the problem is constrained by the equation of continuity.

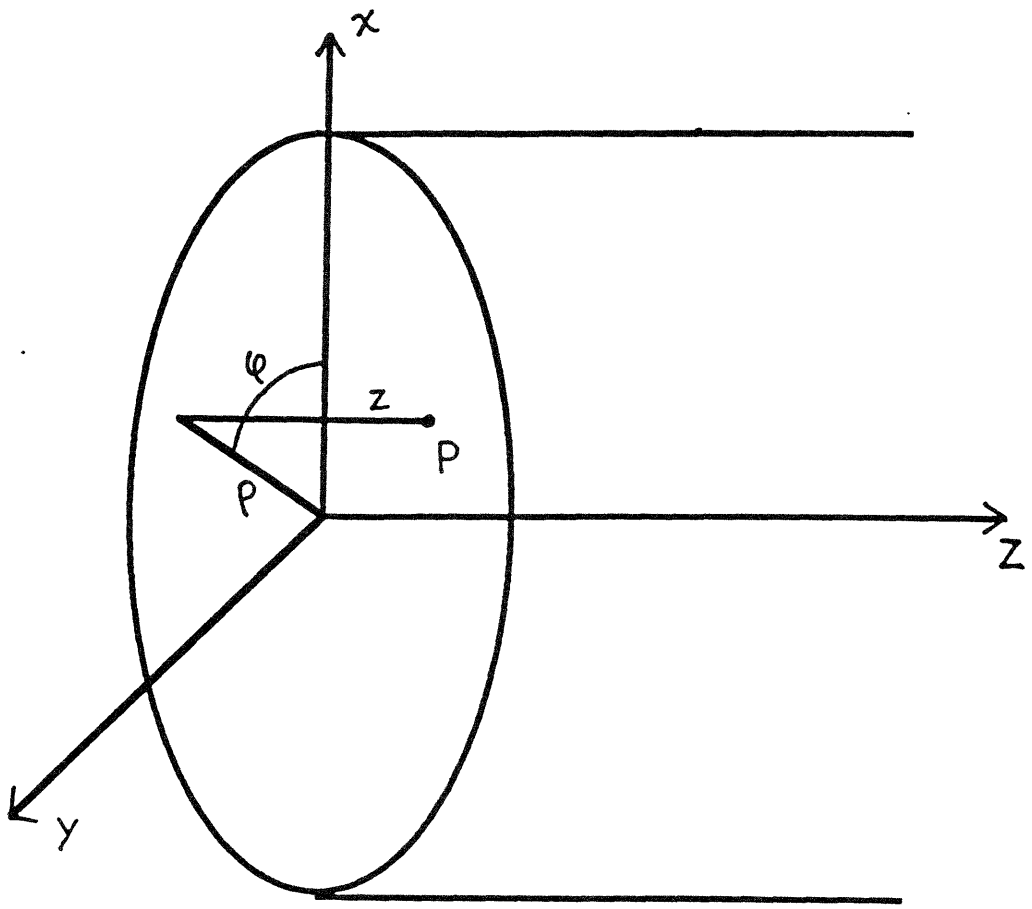

Figure 7.2.1 Cylindrical coordinate system used in the PERL coil design.

III. Reformulate the vector potential equations using the Green's function expansion. The Green's function expansion utilizes a summation over modified Bessel functions of the first and second kind.

IV. Simplify again, this time by identifying the 2DFT of the current density. The result at this stage is the vector potential written as a sum (from the Green's expansion) and an integral (from the 2DFT of the current density).

V. Use the vector potential derived in steps I-IV to write B_z, the axial component of the magnetic field. The result is Eq. 7.6.9, a Fourier-Bessel series. "Fourier" since it includes the 2DFT of the current density and "Bessel" since the Green's function is written in terms of modified Bessel functions of the first and second kind:

$$B_z(\rho,\varphi,z)=\left(\frac{-a\mu_0}{2\pi}\right)\sum_{m=-\infty}^{\infty}\int_{-\infty}^{\infty} dk\, e^{im\varphi}e^{ikz}j_{\varphi}^{m}(k)\,k\,I_m(k\rho)\,K'_m(|k|a). \qquad [7.6.9]$$

In this expression, μ_0 is the permeability constant, a is the radius of the coil, K'_m is the first derivative of the modified Bessel function K_m, and $j_{\varphi}^{m}(k)$ is the 2DFT of $j_\varphi(\varphi,z)$, the phi component of the current density.

VI. Solve Eq. 7.6.9 for $j_{\varphi}^{m}(k)$ by taking the 2DFT of both sides of the equality. The result is Eq. 7.7.3 and is expressed in terms of the 2DFT of the target field

$$j_{\varphi}^{m}(k)=\left(\frac{-1}{a\mu_0}\right)\frac{B_z^m(\rho,k)}{k\,I_m(k\rho)\,K'_m(|k|a)} \qquad [7.7.3]$$

where $B_z^m(\rho,k)$ is the 2DFT of the desired field $B_z(\rho,\varphi,z)$ with conjugate variable pairs $(\varphi\leftrightarrow m)$ and $(z\leftrightarrow k)$.

VII. Compute $B_z^m(\rho, k)$, the 2DFT of the desired field described in Step VI. This result is substituted into Eq. 7.7.3 to yield $j_\varphi^m(k)$, the 2DFT of $j_\varphi(\varphi, z)$.

VIII. Use the equation of continuity to obtain the z component of the current density from the phi component.

Section 7.2 Laws of transformation of vectors

Since the coil is mounted on a cylinder, it is natural to approach the coil design in cylindrical coordinates. As in the previous chapters, the z axis is assumed to be along the axis of the cylinder. (See Figure 7.2.1.) The laws of transformation of vectors from rectangular coordinates (x, y, z) to cylindrical coordinates (ρ, φ, z) are

$$x = \rho \cos \varphi \qquad [7.2.1]$$

$$y = \rho \sin \varphi \qquad [7.2.2]$$

$$a_x = a_\rho \cos \varphi - a_\varphi \sin \varphi \qquad [7.2.3]$$

$$a_y = a_\rho \sin \varphi + a_\varphi \cos \varphi, \qquad [7.2.4]$$

where the z axis remains unaffected by the transformation.

Section 7.3 Derivation of the vector potential in cylindrical coordinates

This section begins with the differential laws of magnetostatics and briefly outlines the derivation of A_ρ, A_φ, and A_z, the components of the vector potential in cylindrical coordinates. The differential laws of magnetostatics state:

$$\nabla \times \bar{B} = \frac{4\pi}{c} \bar{J} \qquad [7.3.1]$$

and

$$\nabla \cdot \bar{B} = 0. \qquad [7.3.2]$$

Since $\nabla \cdot \bar{B} = 0$, B must be the curl of the vector field $\bar{A}(\bar{r})$ termed the vector potential. The general form for the vector potential in unbounded space is[3]

$$\bar{A}(\bar{r}) = \frac{1}{c}\int \frac{\bar{J}(\bar{r}')}{|\bar{r}-\bar{r}'|} d^3\bar{r}' \qquad [7.3.3]$$

where $\bar{J}$ is the current density. Since there is no current flow in the radial direction, $\bar{J}$ has only z and φ components.

Consider first the x-component of the vector potential,

$$A_x(\bar{r}) = \frac{\mu_0}{4\pi}\int dv' \frac{J_x(\bar{r}')}{|\bar{r}-\bar{r}'|} \qquad [7.3.4]$$

where μ_0 is the permeability constant, J_x is the x-component of the current density, and $dv' = \rho' \, d\rho' \, d\varphi' \, dz'$. Using Eq. 7.2.3 to substitute for the left-hand side and the numerator of the integrand,

$$A_\rho(\bar{r})\cos\varphi - A_\varphi(\bar{r})\sin\varphi = \frac{\mu_0}{4\pi}\int dv' \frac{J_\rho(\bar{r}')\cos\varphi' - J_\varphi(\bar{r}')\sin\varphi'}{|\bar{r}-\bar{r}'|}. \qquad [7.3.5]$$

Equation 7.3.5 is simplified by assuming no current flow in the radial direction. That is,

$$J_\rho(\bar{r}') = 0, \qquad [7.3.6]$$

and

$$A_\rho(\bar{r})\cos\varphi - A_\varphi(\bar{r})\sin\varphi = \frac{\mu_0}{4\pi}\int dv' \frac{-J_\varphi(\bar{r}')\sin\varphi'}{|\bar{r}-\bar{r}'|}. \qquad [7.3.7]$$

The y-component of the vector potential is manipulated in a similar fashion via Eqs. 7.2.4 and 7.3.6 to yield

$$A_\rho(\bar{r})\sin\varphi + A_\varphi(\bar{r})\cos\varphi = \frac{\mu_0}{4\pi}\int dv' \frac{J_\varphi(\bar{r}')\cos\varphi'}{|\bar{r}-\bar{r}'|}. \qquad [7.3.8]$$

Subtracting the product of Eq. 7.3.8 and $\cos\varphi$ from the product of Eq. 7.3.7 and $\sin\varphi$, and applying the identities $\sin^2\varphi + \cos^2\varphi = 1$ and $\cos(\varphi-\varphi') = \cos\varphi\cos\varphi' + \sin\varphi\sin\varphi'$,

$$A_\varphi(\bar{r}) = \frac{\mu_0}{4\pi}\int dv' \frac{J_\varphi(\bar{r}')\cos(\varphi-\varphi')}{|\bar{r}-\bar{r}'|}. \qquad [7.3.9]$$

The ρ component of the vector potential, A_ρ, is obtained by a similar procedure. Specifically, the product of Eq. 7.3.7 and $\sin\varphi$ is added to the product of Eq. 7.3.8 and $\cos\varphi$. The result is simplified by $\sin(\varphi-\varphi') = \sin\varphi\cos\varphi' - \cos\varphi\sin\varphi'$ to yield

$$A_\rho(\bar{r}) = \frac{\mu_0}{4\pi}\int dv' \, \frac{J_\varphi(\bar{r}')\sin(\varphi-\varphi')}{|\bar{r}-\bar{r}'|}. \qquad [7.3.10]$$

Since the z axis is unaffected by the coordinate transformation, A_z can be written directly from Eq. 7.3.3,

$$A_z(\bar{r}) = \frac{\mu_0}{4\pi}\int dv' \, \frac{J_z(r')}{|\bar{r}-\bar{r}'|}. \qquad [7.3.11]$$

Section 7.4 The Green's function expansion in cylindrical coordinates

The previous section concluded with equations for the vector potential in cylindrical coordinates: A_ρ, A_φ, and A_z. (Equations 7.3.9-11.) To incorporate these expressions into the coil analysis, it is necessary to replace the common term $\frac{1}{|\bar{r}-\bar{r}'|}$ by the Green's function expansion in cylindrical coordinates

$$\frac{1}{|\bar{r}-\bar{r}'|} = \frac{1}{\pi}\sum_{m=-\infty}^{\infty}\int_{k=-\infty}^{\infty} dk \, e^{im(\varphi-\varphi')} e^{ik(z-z')} I_m(k\rho_<) K_m(|k|\rho_>) \qquad [7.4.1]$$

where $\rho_<$ is the lesser of ρ and $\rho_>$ is the greater of ρ. The lesser of ρ and the greater of ρ are defined with respect to a reference value. In Eq. 7.4.1, the reference value is the parameter a, the coil radius. For example, if the problem is constrained by the boundary condition $\rho < a$, then $I_m(k\rho_<) K_m(|k|\rho_>)$ becomes $I_m(k\rho) K_m(|k|a)$.

Note that the standard form for the Green's function expansion is given by[4]

$$\frac{1}{|\bar{r}-\bar{r}'|} = \frac{2}{\pi}\sum_{m=-\infty}^{\infty}\int_{k=0}^{\infty} dk \, e^{im(\varphi-\varphi')} \cos[k(z-z')] I_m(k\rho_<) K_m(k\rho_>), \qquad [7.4.2]$$

an integral over positive values of k. For reasons which will become apparent in Section 8.3, substitution of the Green's function expansion with an integral over all k is desired.

To prove the equivalence of Eq. 7.4.1, the desired expansion, and the standard form in Eq. 7.4.2, first expand the term $e^{ik(z-z')}$ into its real and imaginary parts. The real part of Eq. 7.4.1 is

$$\mathrm{Re}\left[\frac{1}{|\bar{r}-\bar{r}'|}\right] = \frac{1}{\pi}\sum_{m=-\infty}^{\infty}\int_{k=-\infty}^{\infty} dk\, e^{im(\varphi-\varphi')}\cos[k(z-z')]\, I_m(k\rho_<)\,\mathrm{Re}[K_m(k\rho_>)] \qquad [7.4.3]$$

where the analytic continuation of the modified Bessel functions makes it necessary to incorporate the real part of $K_m(k\rho_>)$.[5] The imaginary part of Eq. 7.4.1 equals zero since there is no imaginary component of the term $\frac{1}{|\bar{r}-\bar{r}'|}$. This is verified mathematically by writing the equation analogous to 7.4.3 for the imaginary part of Eq. 7.4.1. The subsequent integral over all k is zero since the integrand is an odd function with respect to k.

Returning to Eq. 7.4.3, the term $\mathrm{Re}[K_m(k\rho_>)]$ is equivalent to $K_m(|k|\rho_>)$,[6] and the integrand is an even function with respect to k. Consequently, the integral is identically Eq. 7.4.2 in which the integrand is doubled and the range of integration reduced to only the positive values of k.

Section 7.5 Incorporation of the Green's function expansion into the vector potential

The previous section provided the form of the Green's function which is useful to expand the equations for the vector potential. Before the substitution, two sets of definitions are required to simplify the results. The first definition describes the fact that the gradient coils are designed to be mounted on the cylinder form of radius a. Consequently, the current density can be written as

$$\bar{J} = \bar{j}(z,\varphi)\,\delta(\rho - a) \qquad [7.5.1]$$

where $\bar{j}$ is the current density in the gradient coils. (Since the current is constrained to a surface, the current density is expressed in terms of current per unit length.) Throughout the text the current density is discussed in terms of its component equations:

$$J_\varphi = j_\varphi(z,\varphi)\,\delta(\rho - a) \qquad [7.5.2]$$

$$J_z = j_z(z,\varphi)\,\delta(\rho - a). \qquad [7.5.3]$$

The second set of definitions is the 2DFT pairs of the components of $\bar{j}$, the current in the gradient coils:

$$j_z^m(k) \equiv \frac{1}{2\pi}\int_{-\pi}^{\pi} d\varphi\, e^{-i m \varphi} \int_{-\infty}^{\infty} dz\, e^{-ikz}\, j_z(\varphi,z) \qquad [7.5.4]$$

$$j_\varphi^m(k) \equiv \frac{1}{2\pi}\int_{-\pi}^{\pi} d\varphi\, e^{-i m \varphi} \int_{-\infty}^{\infty} dz\, e^{-ikz}\, j_\varphi(\varphi,z) \qquad [7.5.5]$$

In words, $j_z^m(k)$ and $j_z(\varphi,z)$ are 2DFT pairs with conjugate variable pairs $(\varphi \leftrightarrow m)$ and $(z \leftrightarrow k)$. $j_\varphi^m(k)$ and $j_\varphi(\varphi,z)$ are also 2DFT pairs with the same conjugate variable pairs.

Substitution of the Green's function expansion in Eq. 7.4.1 into Eq. 7.3.10, the expression for A_ρ, and considering the region $\rho < a$ (inside the cylinder),

$$A_\rho(\bar{r}) = \frac{\mu_0}{4\pi^2} \sum_{m=-\infty}^{\infty} \int_{k=-\infty}^{\infty} dk\, e^{i m \varphi}\, e^{ikz}\, I_m(k\rho)\, K_m(|k|a)\, \Lambda \qquad [7.5.6]$$

where

$$\Lambda = \int_{v'} dv'\, \sin(\varphi - \varphi')\, e^{-i m \varphi'}\, e^{-ikz'}\, j_\varphi(z', \varphi')\, \delta(\rho' - a) \qquad [7.5.7]$$

is a triple integral with $dv' = \rho'\, d\rho'\, d\varphi'\, dz'$, and the phi component of the current density is written as in Eq. 7.5.2. The expression for Λ is simplified by writing it as the product of three integrals

$$\Lambda = \int_{-\infty}^{\infty} d\rho' \rho' \, \delta(\rho' - a) \int_{-\pi}^{\pi} d\varphi' \sin(\varphi - \varphi') e^{-i m \varphi'} \int_{-\infty}^{\infty} dz' e^{-i k z'} j_{\varphi}(z', \varphi') \qquad [7.5.8]$$

and noting

$$\int_{-\infty}^{\infty} d\rho' \rho' \, \delta(\rho' - a) = a. \qquad [7.5.9]$$

Consequently,

$$\Lambda = a \int_{-\pi}^{\pi} d\varphi' \sin(\varphi - \varphi') e^{-i m \varphi'} \int_{-\infty}^{\infty} dz' e^{-i k z'} j_{\varphi}(z', \varphi'), \qquad [7.5.10]$$

and $A_{\rho}(\mathbf{r})$ can be written as

$$A_{\rho}(\bar{r}) = \frac{a \mu_0}{4\pi^2} \sum_{m=-\infty}^{\infty} \int_{-\infty}^{\infty} dk \, e^{i m \varphi} e^{i k z} I_m(k\rho) K_m(|k|a) \int_{-\pi}^{\pi} d\varphi' \sin(\varphi - \varphi') e^{-i m \varphi'} \int_{-\infty}^{\infty} dz' e^{-i k z'} j_{\varphi}(z', \varphi'). \qquad [7.5.11]$$

Making the substitution $\sin(\varphi - \varphi') = \frac{i}{2}\left[e^{-i(\varphi - \varphi')} - e^{i(\varphi - \varphi')}\right]$,

$$A_\rho(\bar{r}) = \left(\frac{i a \mu_0}{8\pi^2}\right) \left[\sum_{m=-\infty}^{\infty} \int_{-\infty}^{\infty} dk\, e^{i(m-1)\varphi}\, e^{ikz}\, I_m(k\rho)\, K_m(|k|a) \right.$$

$$\int_{-\pi}^{\pi} d\varphi' \sin(\varphi - \varphi')\, e^{-i(m-1)\varphi'} \int_{-\infty}^{\infty} dz'\, e^{-ikz'}\, j_\varphi(z', \varphi')$$

$$- \sum_{m=-\infty}^{\infty} \int_{-\infty}^{\infty} dk\, e^{i(m+1)\varphi}\, e^{ikz}\, I_m(k\rho)\, K_m(|k|a)$$

$$\left. \int_{-\pi}^{\pi} d\varphi' \sin(\varphi - \varphi')\, e^{-i(m+1)\varphi'} \int_{-\infty}^{\infty} dz'\, e^{-ikz'}\, j_\varphi(z', \varphi') \right]. \qquad [7.5.12]$$

Equation 7.5.12 may be simplified by noting that both summations over m are infinite in both the positive and negative directions. Therefore, m may be replaced by m+1 in the first sum, and m may be replaced by m-1 in the second sum yielding the result

$$A_\rho(\bar{r}) = \left(\frac{i a \mu_0}{8\pi^2}\right) \left[\sum_{m=-\infty}^{\infty} \int_{-\infty}^{\infty} dk\, e^{im\varphi}\, e^{ikz}\, I_{m+1}(k\rho)\, K_{m+1}(|k|a) \right.$$

$$\int_{-\pi}^{\pi} d\varphi'\, e^{-im\varphi'} \int_{-\infty}^{\infty} dz'\, e^{-ikz'}\, j_\varphi(z', \varphi')$$

$$- \sum_{m=-\infty}^{\infty} \int_{-\infty}^{\infty} dk\, e^{im\varphi}\, e^{ikz}\, I_{m-1}(k\rho)\, K_{m-1}(|k|a)$$

$$\left. \int_{-\pi}^{\pi} d\varphi'\, e^{-im\varphi'} \int_{-\infty}^{\infty} dz'\, e^{-ikz'}\, j_\varphi(z', \varphi') \right]. \qquad [7.5.13]$$

Thus, $A_\rho(\bar{r})$ has been manipulated into a form suitable to incorporate the 2DFT pair in Eq. 7.5.5. After this substitution and a combination of terms,

$$A_\rho(\bar{r}) = \left(\frac{i a \mu_0}{4\pi}\right) \sum_{m=-\infty}^{\infty} \int_{-\infty}^{\infty} dk\, e^{i m \varphi} e^{i k z} j_\varphi^m(k) \\ [I_{m+1}(k\rho) K_{m+1}(|k|a) - I_{m-1}(k\rho) K_{m-1}(|k|a)] . \qquad [7.5.14]$$

A similar procedure is used to calculate the phi component of the vector potential A_φ, again considering the region $\rho < a$ (inside the cylinder). First, the Green's function expansion in Eq. 7.4.1 is substituted into Eq. 7.3.9. This results in a sum over m and a four dimensional integral as in Eq. 7.5.6. Second, the integral is simplified by Eq. 7.5.9 and the substitution

$$\cos(\varphi - \varphi') = \frac{1}{2}[e^{i(\varphi-\varphi')} + e^{-i(\varphi-\varphi')}]. \qquad [7.5.15]$$

The result for A_φ becomes

$$A_\varphi(\bar{r}) = \left(\frac{a \mu_0}{8\pi^2}\right) \Bigg[\sum_{m=-\infty}^{\infty} \int_{-\infty}^{\infty} dk\, e^{i(m+1)\varphi} e^{i k z} I_m(k\rho) K_m(|k|a) \\ \int_{-\pi}^{\pi} d\varphi'\, e^{-i(m+1)\varphi'} \int_{-\infty}^{\infty} dz' e^{-i k z'} j_\varphi(z', \varphi') \\ + \sum_{m=-\infty}^{\infty} \int_{-\infty}^{\infty} dk\, e^{i(m-1)\varphi} e^{i k z} I_m(k\rho) K_m(|k|a) \\ \int_{-\pi}^{\pi} d\varphi'\, e^{-i(m-1)\varphi'} \int_{-\infty}^{\infty} dz' e^{-i k z'} j_\varphi(z', \varphi') \Bigg] . \qquad [7.5.16]$$

Equation 7.5.16 may be simplified by noting that both summations over m are infinite in both the positive and negative directions. Therefore, in step three m may be replaced by

m-1 in the first sum, and m may be replaced by m+1 in the second sum to give a form suitable for substitution by the 2DFT in Eq. 7.5.5. After combining terms the final result becomes

$$A_\varphi(\bar{r}) = \left(\frac{a\mu_0}{4\pi}\right) \sum_{m=-\infty}^{\infty} \int_{-\infty}^{\infty} dk\, e^{im\varphi} e^{ikz} j_\varphi^m(k) \\ [I_{m-1}(k\rho) K_{m-1}(|k|a) + I_{m+1}(k\rho) K_{m+1}(|k|a)] . \qquad [7.5.17]$$

The z-component of the vector potential follows a simpler procedure. First, Eq. 7.4.1 is substituted into Eq. 7.3.11. The result is simplified via Eq. 7.5.9, and incorporation of the 2DFT in Eq. 7.5.4 gives

$$A_z(\bar{r}) = \left(\frac{a\mu_0}{2\pi}\right) \sum_{m=-\infty}^{\infty} \int_{-\infty}^{\infty} dk\, e^{im\varphi} e^{ikz} j_z^m(k)\, I_m(k\rho)\, K_m(|k|a). \qquad [7.5.18]$$

Section 7.6 Fourier-Bessel expansion of the axial component of a magnetic field

Section 7.5 concluded with working expressions for the three cylindrical components of the vector potential. In this section, those expressions are used to write $B_z(\rho, \varphi, z)$, the axial component of a generalized magnetic field, as an expansion containing Fourier and Bessel components.

Since a magnetic field $\bar{B}$ is the curl of its vector potential $\bar{A}$,

$$\bar{B}(\bar{r}) = \bar{\nabla} \times \bar{A}(\bar{r}), \qquad [7.6.1]$$

and the curl of $\bar{A}$ in cylindrical coordinates is[7]

$$\bar{\nabla} \times \bar{A}(\bar{r}) = \bar{a}_\rho \left(\frac{1}{\rho}\frac{\partial A_z}{\partial \varphi} - \frac{\partial A_\varphi}{\partial z}\right) + \bar{a}_\varphi \left(\frac{\partial A_\rho}{\partial z} - \frac{\partial A_z}{\partial \rho}\right) + \bar{a}_z \frac{1}{\rho}\left(\frac{\partial(\rho A_\varphi)}{\partial \rho} - \frac{\partial A_\rho}{\partial \varphi}\right), \qquad [7.6.2]$$

the axial component of a generalized magnetic field may be written

$$B_z(\rho, \varphi, z) = \frac{1}{\rho}\left(\frac{\partial(\rho A_\varphi)}{\partial \rho} - \frac{\partial A_\rho}{\partial \varphi}\right). \qquad [7.6.3]$$

Differentiating Eqs. 7.5.14 and 7.5.17, substituting into 7.6.3, and algebriacally simplifying the result gives

$$B_z(\rho,\varphi,z)=\left(\frac{a\mu_0}{4\pi\rho}\right)\sum_{m=-\infty}^{\infty}\int_{-\infty}^{\infty}dk\,e^{im\varphi}e^{ikz}j_{\varphi}^{m}(k)$$
$$\left\{K_{m-1}(|k|a)\left[(1-m)I_{m-1}(k\rho)+k\rho\,I'_{m-1}(k\rho)\right]\right. \qquad [7.6.4]$$
$$\left.+K_{m+1}(|k|a)\left[(1+m)I_{m+1}(k\rho)+k\rho\,I'_{m+1}(k\rho)\right]\right\}.$$

where the symbol (′) represents the first derivative and is unrelated to the "prime" symbol ('). This form of $B_z(\rho,\varphi,z)$ is simplified by manipulating the recurrence relationships for cylinder functions[8] into the forms:

$$(1-m)I_{m-1}(k\rho)+k\rho\,I'_{m-1}(k\rho)=k\rho\,I_m(k\rho) \qquad [7.6.5]$$

$$(1+m)I_{m+1}(k\rho)+k\rho\,I'_{m+1}(k\rho)=k\rho\,I_m(k\rho) \qquad [7.6.6]$$

$$-2K'_m(|k|a)=K_{m+1}(|k|a)+K_{m-1}(|k|a). \qquad [7.6.7]$$

Equations 7.6.5 and 7.6.6 may be directly substituted into Eq. 7.6.4 and simplified to

$$B_z(\rho,\varphi,z)=\left(\frac{a\mu_0}{4\pi\rho}\right)\sum_{m=-\infty}^{\infty}\int_{-\infty}^{\infty}dk\,e^{im\varphi}e^{ikz}j_{\varphi}^{m}(k)\,k\rho\,I_m(k\rho)\{K_{m+1}(|k|a)+K_{m-1}(|k|a)\} \qquad [7.6.8]$$

which becomes

$$B_z(\rho,\varphi,z)=\left(\frac{-a\mu_0}{2\pi}\right)\sum_{m=-\infty}^{\infty}\int_{-\infty}^{\infty}dk\,e^{im\varphi}e^{ikz}j_{\varphi}^{m}(k)\,k\,I_m(k\rho)\,K'_m(|k|a) \qquad [7.6.9]$$

after application of Eq. 7.6.7.

Section 7.7 Solution for the current density of a generalized target field

Equation 7.6.9 is a fundamental step in the design of the PERL coil. In general terms, the left hand side is the desired magnetic field profile which is termed the "target field". In section 8.2, the target field will be defined as a form of the PERL field. The right hand side is the Fourier-Bessel series expansion over the parameters m and k. At

the present stage of this analysis, the advantages of the Fourier-Bessel expansion have not become apparent. However, when the functional form of the PERL field is applied to the design, the utility of this expansion will become apparent.

The subsequent analysis incorporates the 2DFT of the target field

$$B_z^m(\rho, k) = \left(\frac{1}{2\pi}\right) \int_{-\pi}^{\pi} d\varphi \, e^{-im\varphi} \int_{-\infty}^{\infty} dz \; e^{-ikz} B_z(\rho, \varphi, z). \qquad [7.7.1]$$

In words, $B_z^m(\rho, k)$ and $B_z(\rho, \varphi, z)$ are 2DFT pairs with conjugate variable pairs $(\varphi \leftrightarrow m)$ and $(z \leftrightarrow k)$.

Recall from Eq. 7.5.5 that the parameter $j_\varphi^m(k)$ in Eq. 7.6.9 is the 2DFT of the phi component of the current density in the gradient coils. Thus, a solution for $j_\varphi^m(k)$ gives the phi component of the current density distribution on the cylinder form required to create the target field. This solution is obtained by taking the inverse 2DFT of 7.6.9,

$$\left(\frac{1}{4\pi^2}\right) \int_{-\pi}^{\pi} d\varphi \, e^{-im\varphi} \int_{-\infty}^{\infty} dz \; e^{-ikz} B_z(\rho, \varphi, z) = \left(\frac{-a\mu_0}{2\pi}\right) j_\varphi^m(k) \, k \, I_m(k\rho) \, K'_m(|k|a), \qquad [7.7.2]$$

substituting Eq. 7.7.1, canceling 2π on both sides, and solving for $j_\varphi^m(k)$ to yield

$$j_\varphi^m(k) = \left(\frac{-1}{a\mu_0}\right) \frac{B_z^m(\rho, k)}{k \, I_m(k\rho) \, K'_m(|k|a)}. \qquad [7.7.3]$$

Equation 7.7.3 illustrates a two-step procedure to calculate the phi component of the current density required to create a target field $B_z(\rho, \varphi, z)$. The first step is to compute $B_z^m(\rho, k)$ from Eq. 7.7.1, and the second step is to substitute the result into Eq. 7.7.3.

The constraints on the solution for the current density provide a solution for the z component directly from the phi component. Since charge is conserved on the cylindrical

form and the coil operates at steady state, the divergence of the current density equals zero, or

$$\overline{\nabla} \cdot \bar{j} = 0. \qquad [7.7.4]$$

Writing the divergence in cylindrical coordinates,

$$\overline{\nabla} \cdot \bar{j} = \frac{1}{\rho}\left(\frac{\partial(\rho j_\rho)}{\partial \rho} + \frac{\partial j_\varphi}{\partial \varphi}\right) + \frac{\partial j_z}{\partial z} = 0, \qquad [7.7.5]$$

and since $j_\rho = 0$ and $\rho = a$ on the cylinder,

$$\frac{1}{a}\frac{\partial j_\varphi}{\partial \varphi} + \frac{\partial j_z}{\partial z} = 0. \qquad [7.7.6]$$

Thus, Eq. 7.7.6 may be used to calculate j_z and j_φ as functions of φ and z. However, the two step procedure described above works in the 2DFT space defined by the parameters m and k. The expressions for j_φ and j_z as functions of φ and z are obtained from their 2DFT counterparts by inverting Equations 7.5.4 and 7.5.5:

$$j_\varphi(\varphi,z) = \frac{1}{2\pi}\sum_{m=-\infty}^{\infty}\int_{k=-\infty}^{\infty} dk\, e^{i m \varphi} e^{i k z} j_\varphi^m(k) \qquad [7.7.7]$$

and

$$j_z(\varphi,z) = \frac{1}{2\pi}\sum_{m=-\infty}^{\infty}\int_{k=-\infty}^{\infty} dk\, e^{i m \varphi} e^{i k z} j_z^m(k). \qquad [7.7.8]$$

Taking the derivatives of Eq. 7.7.7 with respect to phi and Eq. 7.7.8 with respect to z, substituting into Eq. 7.7.6, and solving for $j_z^m(k)$,

$$j_z^m(k) = \frac{-m}{ka} j_\varphi^m(k). \qquad [7.7.9]$$

Thus, Eqs. 7.7.6 and 7.7.9 give the relationship between the two nonzero components of the current density in both spaces.

Section 7.8 Conclusions

This chapter derives a formalism to design cylindrical magnetic field gradient coils. The input to the formalism is the target field, and the output is the current density required on the cylindrical form required to create the target field. Section 7.1 gives an overview of the method, and the mathematics appear in the remaining sections of this chapter. Chapter 8 identifies a form of the PERL field as the target, and this technique yields an analytic solution for the current density used to produce the field.

Chapter 7 References

[1] R Turner. A target field approach to optimal coil design, J. Physics D. 19, L147, 1986.
[2] R Turner and RM Bowley. Passive screening of switched magnetic field gradients, J. Physics E. 19, 876, 1986.
[3] JD Jackson. *Classical Electrodynamics*, John Wiley ans Sons, New York, 1962. (pp. 139-141)
[4] JD Jackson. *Classical Electrodynamics*, John Wiley ans Sons, New York, 1962. (p. 86)
[5] M Abramowitz and IA Stegun. *Handbook of Mathematical Functions*. Dover Publications, New York, 1970. (p. 376)
[6] M Abramowitz and IA Stegun. *Handbook of Mathematical Functions*. Dover Publications, New York, 1970. (p. 376)
[7] PM Morse and H Feshbach. *Methods of Theoretical Physics*. McGraw Hill, New York, 1953. (p. 116)
[8] M Abramowitz and IA Stegun. *Handbook of Mathematical Functions*. Dover Publications, New York, 1970. (p. 376)

Chapter 8. PERL coil specifications.

Section 8.1 Introduction

While Chapter 7 derives the mathematical foundation on which to design the PERL coil, the present chapter uses the foundation to yield specifications for an actual coil. Section 8.2 uses Laplace's equation to compute a realizable field with cylindrical geometry, and the remaining sections compute both the surface current density and the actual wire configurations to produce the field with a cylindrical geometry.

Section 8.2 The functional form of the PERL field

This section discusses the realization of a functional form of the PERL field which can be incorporated into the coil design analysis developed in Chapter 7. Using the terminology adopted in Chapter 7, this section specifies a suitable target field for incorporation to the Fourier-Bessel mathematics.

This discussion is an important step to bridge the idea of the novel encoding technology with a realizable coil. One essential condition for the coil is that any realizable magnetic field must satisfy Maxwell's equations. It can be shown[12] that a sufficient substitute for this condition is that the magnetic field satisfies the vector Laplacian equation:

$$\nabla^2 \overline{B} = 0. \qquad [8.2.1]$$

NMR applications consider only B_z, the z component of the field, since contributions to the MRI signal from the B_x and B_y components are negligible.

Substituting the definition of the PERL field into Eq. 8.2.1 gives

$$q_z^2 \, g_x \, x \cos(q_z z) = 0 \qquad [8.2.2]$$

and leads to the conclusion that the PERL field profile defined in Chapter 1 is not realizable. Therefore, the goal of this section is to identify a functional form of the PERL field which approximates Eq. 1.1.1 while satisfying Laplace's equation.

Linear magnetic field gradients satisfying the equation $\overline{G} = \nabla B_z$ are the most common field profiles used for MRI. Gradients of this form satisfy Laplace's equation, and more importantly, each component, G_x G_y, and G_z, independently satisfies Laplace's equation. Thus, each gradient component may be applied without constraining the field along another direction. In order to determine the types of field profiles which satisfy Eq. 8.2.1, this equation is solved in cylindrical coordinates by separation of variables for a field which is periodic along the z direction.

Consider the cylindrical coordinate system (ρ, φ, z) illustrated in Figure 7.2.1. The solution to Laplace's equation in cylindrical coordinates assuming a periodic component along z, the axis of the cylinder, can be written[3]

$$B_z(\rho,\varphi,z) = \sum_{m=0}^{\infty} \sum_{\alpha=0}^{\infty} C_{m\alpha} \begin{Bmatrix} I_m(\alpha\rho) \\ K_m(\alpha\rho) \end{Bmatrix} \begin{Bmatrix} \cos(m\varphi) \\ \sin(m\varphi) \end{Bmatrix} \cos(\alpha z + \theta_\alpha) \qquad [8.2.3]$$

where I_m and K_m are the modified Bessel functions of order m and are plotted in Figure 4.3.1. For generality the phase shift term θ_α is introduced to include the possibility of shifting or translating the periodic dependence along the z axis. There are several physical constraints which restrict and simplify the solution for $B_z(\rho,\varphi,z)$ in Eq. 8.2.3. To begin, solutions involving K_m are eliminated by the condition that $B_z(\rho,\varphi,z)$ is finite at the origin. The result simplifies further since only a single periodic component $(\alpha = q_z)$ is desired, and the solution for $B_z(\rho,\varphi,z)$ becomes

$$B_z(\rho,\varphi,z) = \sum_{m=0}^{\infty} C_m I_m(q_z\rho) \begin{Bmatrix} \cos(m\varphi) \\ \sin(m\varphi) \end{Bmatrix} \cos(q_z z + \theta). \qquad [8.2.4]$$

The next restriction stems from the plots of the modified Bessel functions in Figure 4.3.1: $I_m(0) = 1$ for $m = 0$, and $I_m(0) = 0$ otherwise. In order to satisfy the condition that the PERL field is zero at the origin, i.e. where $\rho = 0$, the $m = 0$ term is eliminated from the sum by setting $C_0 = 0$.

One representation of $I_m(x)$ is the following power series expansion[4]

$$I_m(x) = \sum_{n=0}^{\infty} \frac{1}{n!\,(n+m)!} \left(\frac{x}{2}\right)^{2n+m} \qquad [8.2.5]$$

which shows that $I_m(x)$ is monotonic with even symmetry for m even and odd symmetry for m odd. This expression shows that the $m = 1$ term is the only term of $I_m(x)$ which contains a linear component along x. As seen in Figure 4.3.1, $I_1(x)$ is well approximated by $x/2$ in the range $|x| \leq 1$. In order to maintain this linear dependence, the terms in Eq. 8.2.4 for which $m \neq 1$ must be eliminated. This is accomplished by setting $C_m = 0$ for $m \neq 1$.

The final desired condition is to minimize the dependence of B_z on the y axis in rectangular coordinates which corresponds to minimizing the dependence on $\rho\,(\varphi = \pi/2)$. This dependence is minimized by dropping the $\sin\varphi$ term to leave

$$B_z(\rho,\varphi,z) = \frac{2g_x}{q_z} I_1(q_z\rho) \cos\varphi \cos(q_z z). \qquad [8.2.6]$$

For this form of the PERL field, the parameter q_z affects both the x and the z axes equally, and a large value for q_z restricts the available imaging region to a small size.

Section 8.3 The current density of the PERL coil

Section 8.2 concludes with Eq. 8.2.6, the form of the PERL field which will be incorporated into the design of the PERL coil described in Chapter 7. Eq. 8.2.6 is the input to this four step algorithm summarized in Section 7.7. The output is $\bar{j}$, the current density on a cylindrical form of radius a. The first step is to compute the 2DFT of the target field by substituting Eq. 8.2.6 into Eq. 7.7.1

$$B_z^m(\rho,k)=\left(\frac{g_x I_1(q_z\rho)}{\pi q_z}\right)\int_{-\pi}^{\pi} d\varphi\, e^{-im\varphi}\cos\varphi\int_{-\infty}^{\infty} dz\; e^{-ikz}\cos(q_z z). \qquad [8.3.1]$$

The first integral in Eq. 8.3.1 is solved by writing the cosine term as

$$\cos\varphi=\frac{e^{i\varphi}+e^{-i\varphi}}{2}. \qquad [8.3.2]$$

The integral is then broken into two pieces and solved readily:

$$\int_{-\pi}^{\pi} d\varphi\; e^{-im\varphi}\cos(\varphi)=\frac{1}{2}\left[\int_{-\pi}^{\pi} d\varphi\; \exp(-i(m-1)\varphi)+\int_{-\pi}^{\pi} d\varphi\; \exp(-i(m+1)\varphi)\right]$$

$$=\frac{\sin[(m-1)\pi]}{m-1}+\frac{\sin[(m+1)\pi]}{m+1}$$

$$=\begin{cases}\pi, \text{ for } m=\pm 1\\ 0, \text{ otherwise}\end{cases} \qquad [8.3.3]$$

The second integral in Eq. 8.3.1 is also solved by expanding the cosine term as in Eq. 8.3.2 to yield

$$\int_{-\infty}^{\infty} dz\; e^{-ikz}\cos(q_z z)=\frac{1}{2}\left[\int_{-\infty}^{\infty} dz\; \exp[-i(k-q_z)z]+\int_{-\infty}^{\infty} dz\; \exp[-i(k+q_z)z]\right]. \qquad [8.3.4]$$

Recognizing one definition for the Dirac delta function as[5]

$$\delta(x-a)\equiv\frac{1}{2\pi}\left[\int_{-\infty}^{\infty} d\alpha\; \exp[i\alpha(x-a)]\right], \qquad [8.3.5]$$

Eq. 8.3.4 becomes

$$\int_{-\infty}^{\infty} dz\ \exp[-ikz]\cos(q_z z) = \pi\left[\delta(q_z\text{-}k) + \delta(q_z\text{+}k)\right]. \qquad [8.3.6]$$

Substituting Eqs. 8.3.3 and 8.3.6, the results of the two integrations, into the expression for $B_z^m(\rho, k)$,

$$B_z^m(\rho,k) = \begin{cases} \dfrac{\pi\, g_x\, I_1(q_z\rho)}{q_z}\left[\delta(q_z\text{-}k) + \delta(q_z\text{+}k)\right], \text{ for } m = \pm 1 \\ 0, \text{ otherwise.} \end{cases} \qquad [8.3.7]$$

Section 7.7 mentions that the advantages of the Fourier-Bessel expansion become apparent when the functional form of the PERL field is incorporated into the problem. These advantages become evident in Eq. 8.3.7. Specifically, $B_z^m(\rho, k)$ equals zero when $m \neq \pm 1$, and the result for $m = \pm 1$ contains two delta function which will greatly simplify integrations over the parameter k.

The second step of the algorithm is to substitute $B_z^m(\rho, k)$ into Eq. 7.7.3 to yield $j_\varphi^m(k)$, the 2DFT of the phi component of the current density,

$$j_\varphi^{\pm 1}(k) = \frac{-\pi\, g_x I_1(q_z\rho)\left[\delta(q_z\text{-}k) + \delta(q_z\text{+}k)\right]}{a\mu_0\, q_z\, k I_m(k\rho)\, K'_m(|k|a)} \qquad [8.3.8]$$

where $j_\varphi^m(k) = 0$ for $m \neq \pm 1$.

The third step of the algorithm uses Eq. 7.7.7 to calculate $j_\varphi(\varphi, z)$:

$$j_\varphi(\varphi, z) = \left(\frac{e^{i\varphi}}{2}\right) C \int_{-\infty}^{\infty} \frac{N(k)\, dk}{I_1(k\rho)\, K'_1(|k|a)} + \left(\frac{e^{-i\varphi}}{2}\right) C \int_{-\infty}^{\infty} \frac{N(k)\, dk}{I_{-1}(k\rho)\, K'_{-1}(|k|a)} \qquad [8.3.9]$$

where $C \equiv \frac{-g_x I_1(q_z\rho)}{a\mu_0 q_z}$ and $N(k) \equiv \left[\delta(q_z-k) + \delta(q_z+k)\right] \frac{e^{ikz}}{k}$. In a manner similar to Section 7.6, the integrals over the modified Bessel functions are simplified by manipulating the recurrence relationships for cylinder functions into the forms[6]

$$I_1(k\rho)\, K'_1(|k|a) = I_{-1}(k\rho)\, K'_{-1}(|k|a) \qquad [8.3.10]$$

$$I_1(q_z\rho)\, K'_1(q_z a) = -\, I_1(-q_z\rho)\, K'_1(-q_z a). \qquad [8.3.11]$$

Equation 8.3.10 proves that the two integrands in Eq. 8.3.9 are equivalent and the expression for $j_\varphi(\varphi, z)$ may be reduced to

$$j_\varphi(\varphi, z) = \left(\frac{e^{i\varphi} + e^{-i\varphi}}{2}\right) C \int_{-\infty}^{\infty} \frac{\left[\delta(q_z-k) + \delta(q_z+k)\right] e^{ikz}\, dk}{k\, I_1(k\rho)\, K'_1(|k|a)}$$

$$= \frac{C \cos\varphi}{q_z} \left[\frac{e^{iq_z z}}{I_1(q_z\rho)\, K'_1(q_z a)} - \frac{e^{-iq_z z}}{I_1(-q_z\rho)\, K'_1(-q_z a)}\right]. \qquad [8.3.12]$$

which is then simplified by Equation 8.3.11,

$$j_\varphi(\varphi, z) = \frac{-2\, g_x \cos\varphi \cos(q_z z)}{a\mu_0 q_z^2\, K'_1(q_z a)}. \qquad [8.3.13]$$

Equation 8.3.13 is the final form for $j_\varphi(\varphi, z)$; the fourth step of the algorithm obtains $j_z(\varphi, z)$ from the results from $j_\varphi(\varphi, z)$. One approach returns to Eq. 7.7.9, the relationship between $j_z^m(k)$ and $j_\varphi^m(k)$. After identifying $j_z^m(k)$, its inverse 2DFT can then be computed to yield $j_z(\varphi, z)$. A simpler method begins by rearranging the continuity equation (Eq. 7.7.6) and solving for $j_z(\varphi, z)$

$$j_z(\varphi, z) = \int dz \frac{\partial}{\partial z}\left(j_z(\varphi, z)\right) \qquad [8.3.14]$$

where

$$\frac{\partial}{\partial z}\left(j_z(\varphi, z)\right) = -\frac{1}{a} \frac{\partial j_\varphi(\varphi, z)}{\partial \varphi}. \qquad [8.3.15]$$

Substituting the result from Eq. 8.3.13 into Eq. 8.3.14 and performing the integration with respect to z gives

$$j_z(\varphi,z) = \frac{-2\, g_x \sin\varphi \sin(q_z z)}{a^2 \mu_0 q_z^3 K'_1(q_z a)} \,. \qquad [8.3.16]$$

Equations 8.3.13 and 8.3.16 completely specify the current density in the PERL coil, and Figure 8.3.1 illustrates a vector plot of the current density.

These results for the current density can be rewritten as

$$j_\varphi(\varphi,z) = f(q_z,g_x,a)\cos\varphi\cos(q_z z) \qquad [8.3.17]$$

and

$$j_z(\varphi,z) = f(q_z,g_x,a)(a q_z)^{-1}\sin\varphi\sin(q_z z) \qquad [8.3.18]$$

where f is given by

$$f(q_z,g_x,a) = \frac{2 g_x}{\mu_0 a q_z^2 K'_1(q_z a)} \qquad [8.3.19]$$

and is identified in Section 8.5 as an efficiency function with dimensions of current per unit length.

Section 8.4. The surface current of the PERL coil

While Eqs. 8.3.17-19 give the current density required on a cylinder former of radius a to produce the form of the PERL field in Eq. 8.2.6, they do not directly yield the actual current on the cylindrical surface. This current is termed the surface current, and it is denoted by $\bar{I}(\varphi,z)$. The derivation of $\bar{I}(\varphi,z)$ begins with Figure 8.3.1, the vector plot of the current density.

The vector plot illustrates the direction and the magnitude of the surface current. Specifically, the direction of the vectors are the direction of the current, and integration

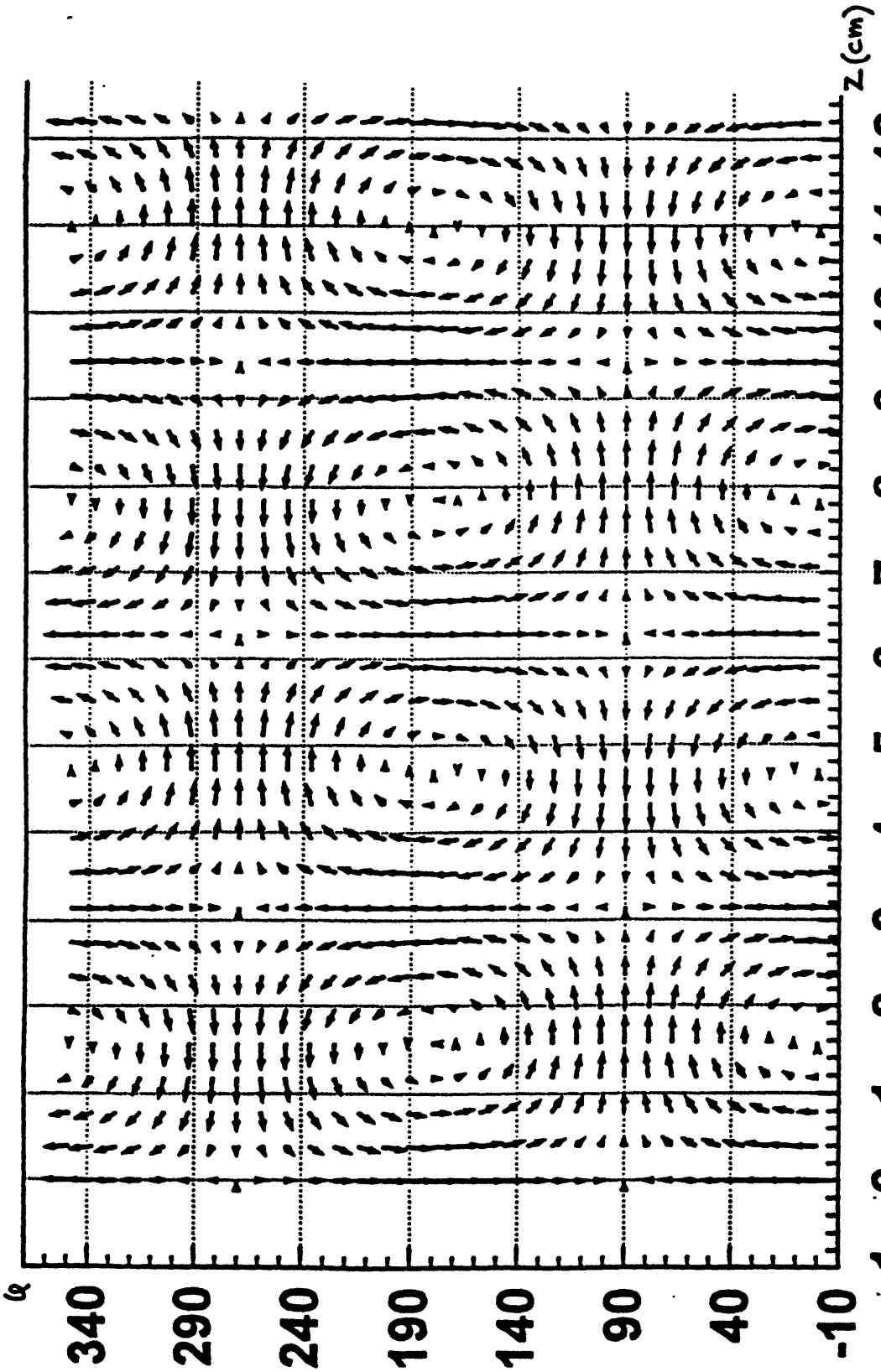

Figure 8.3.1 Vector plot of the current density $\bar{j}$. Constants are set to one to illustrate the functional form. Vector arrows point in the direction of the current density; vector lengths indicate the magnitude of the current density.

perpendicular to the current density vector at any point gives the magnitude of the current at that point. The calculation is formalized by introducing the stream function $S(\varphi, z)$.[7,8,9] In general, $S(\varphi, z)$ describes a flow in which every region of the flow is free from sources or sinks. Lines of constant S are called streamlines and are parallel to the flow. In this application, the surface current is the flow, and the streamlines represent the idealized surface current $\bar{I}(\varphi, z)$.

From the discussion of the vector plot above, the relationship between the current density and the stream function can be written as

$$\bar{j} = \bar{e}_l \frac{dS}{dl_\perp} \qquad [8.4.1]$$

where $\bar{e}_l$ is a unit vector and the subscript l represents the direction of the current density at any given point in Figure 8.3.1. The term $dS/dl_\perp$ is the derivative of the stream function with respect to the direction perpendicular to the current density at the same point. In cylindrical coordinates with the current density $\bar{j}$ restricted to a cylinder of constant radius a, the nonzero components of Eq. 8.4.1 become

$$-j_\varphi = \frac{\partial S}{\partial z} \qquad [8.4.2]$$

and

$$a j_z = \frac{\partial S}{\partial \varphi}. \qquad [8.4.3]$$

The stream function for the PERL coil is obtained by substituting Eqs. 8.3.17 and 8.3.18 into Eqs. 8.4.2 and 8.4.3 respectively and solving for $S(\varphi, z)$,

$$S(\varphi, z) = f q_z^{-1} \cos\varphi \sin(q_z z). \qquad [8.4.4]$$

The functional form of the streamlines is plotted in Figure 8.4.1 with $q_z = 1\,\text{cycle/cm}$. They are a series of concentric closed curves, and as mentioned above, they represent an idealized surface current $\bar{I}(\varphi, z)$. The actual surface current is obtained by plotting streamlines separated by a constant step-size, breaking each closed curve at a convenient point, and joining adjacent curves to form a spiral winding pattern.

Section 8.5. The efficiency of the PERL coil

Given the solution for the current profile to produce the PERL field as defined in Eq. 8.2.6, the discussion turns to an evaluation of the current required on the cylindrical form to create the field. This current is determined by the efficiency function $f(q_z, g_x, a)$ given in Eq. 8.3.19. In terms of current density (current per unit distance), the efficiency function represents the required current per unit cm on the surface of the cylinder. The actual current is determined by Eq. 8.4.4; the value of f/q_z yields the current (in Amperes) required through the wire positions as determined by the stream function. Figure 8.5.1 plots f as a function of a, the coil radius, where $g_x = 1\,\text{G/cm}$ and $q_z/2\pi = 1\,\text{cycle/cm}$. This plot illustrates the efficiency problem for large scale imaging with the PERL technology. (Since $q_z/2\pi = 1\,\text{cycle/cm}$, the plot for f/q_z would be identical.) The behavior of f is dominated by the term K'_1 in the denominator. As seen in Figure 4.3.1, $K'_1(x)$ approaches zero asymptotically for $x > 3$, and thus the first derivative becomes small. At a coil radius of 8 cm, the current density approaches 100 A/cm; at 10 cm, the current density exceeds 500 A/cm. Typical gradient power amplifiers for MRI have continuous current rating between 100 and 400 A, depending on the impedance of the coil and therefore the rate of voltage output. Assuming for example a power supply of 200 A and an integration of the current density of 1 cm perpendicular to its direction, a coil radius of approximately 9 cm can be achieved. However, it is important to identify the usable region of this coil which is restricted to portion where the linearity along x is preserved. This creates an efficiency criteria of the coil where the

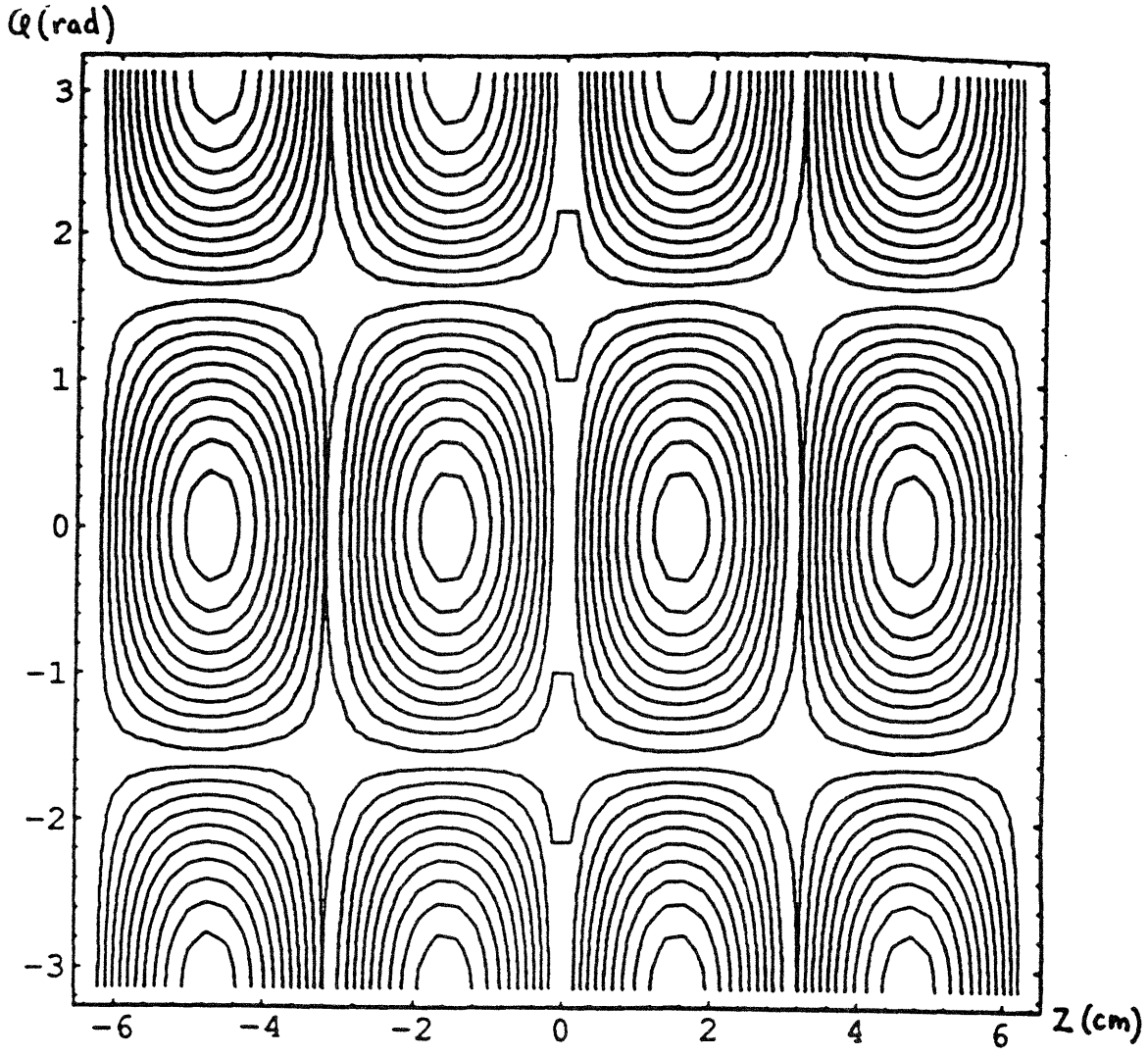

Figure 8.4.1 Plot of the PERL coil streamlines with constants set to one to illustrate the functional form. See text for description.

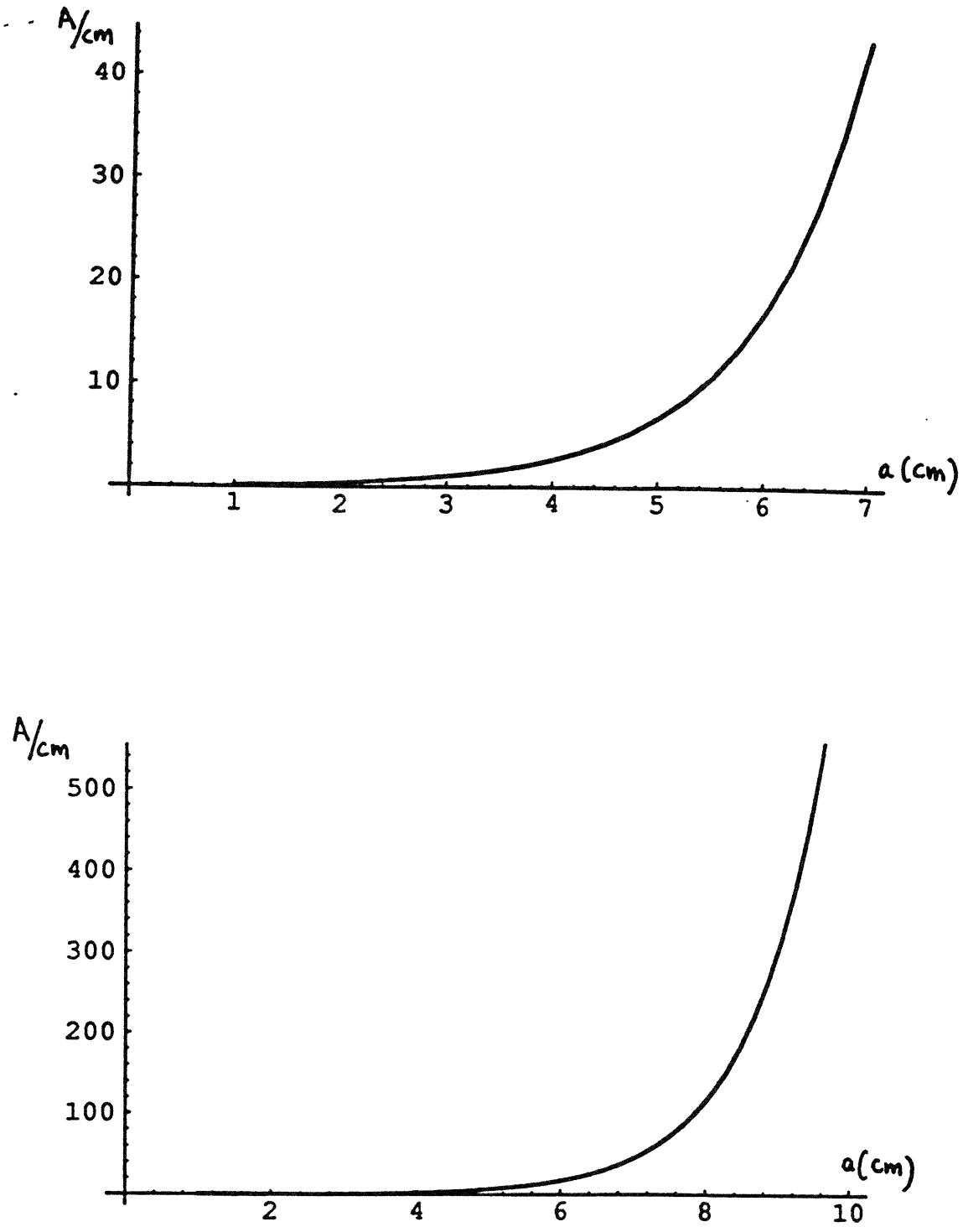

Figure 8.5.1 The efficiency function for the PERL coil as a function of coil radius a. The lower plot includes larger values of a.

central linear region has optimal efficiency. (Recall the behavior of I_1 as illustrated in Figure 4.3.1; this region of strict linearity of the modified Bessel function translates into the restriction $|q_z \rho| \leq 1$ for the PERL coil.)

Although the poor efficiency effectively prohibits whole body imaging with the PERL technology, coils with small radii have an excellent efficiency since $K'_1(x)$ has a steep slope in the region $0<x<2$. Recalling the tradeoff between imaging speed and penetration discussed in Chapter 4, and adding the limitations discussed in this chapter, the PERL field becomes ideally suited for imaging the surface of small volumes.

Section 8.6 Conclusions

This chapter uses the Fourier-Bessel formalism developed in Chapter 7 and stream functions to specify the cylindrical PERL coil. Since the original function for the PERL field can not be realized, the target field in Eq. 8.2.6 is derived by solving Laplace's equation by separation of variables and restricting the result with the desired boundary conditions. The Fourier-Bessel formalism yields the current density required on the cylindrical form, and the stream functions convert the current density to a final current profile. An efficiency function for the PERL coil is identified; this function effectively limits the PERL technology to small imaging volumes.

Chapter 8 References

[1] F Romeo and DI Hoult. Magnetic field profiling: analysis and correcting coil design. Magnetic Resonance in Medicine 1:44, 1984.
[2] JD Jackson. *Classical Electrodynamics*, John Wiley ans Sons, New York, 1962. (p. 138)
[3] PM Morse and H Feshbach. *Methods of Theoretical Physics*. McGraw Hill, New York, 1953. (p. 1259)
[4] J Spanier and KB Oldham, *An Atlas of Functions*, Harper and Row Publishers, Washington, 1987.
[5] Boas ML. *Mathematical Methods in the Physical Sciences, 2nd Ed.* John Wiley and Sons, 1983. (p.669)
[6] M Abramowitz and IA Stegun. *Handbook of Mathematical Functions*. Dover Publications, New York, 1970. (p. 376)
[7] Edelstein et al. Current streamline method for coil construction. US Patent 4,840,700. Jun. 20, 1989.
[8] Schenck et al. Transverse gradient field coils for nuclear magnetic resonance imaging. US Patent 4,646,024. Feb. 24, 1987.
[9] Roemer et al. Self-shielded gradient coils for nuclear magnetic resonance imaging. US Patent 4,737,716. Apr. 12, 1988.

CHAPTER 9. Conclusions and future work.

Section 9.1 Conclusions

This project presents a new magnetic field geometry for encoding of spatial information for MRI. The field given in Eq. 1.1.1 and illustrated in Figure 1.1.1 is called the PERL field since it is PERiodic in the z-dimension and Linear in the x-dimension. The PERL geometry offers fundamentally new ways to image, and it requires a new reconstruction algorithm and a new coil design.

The PERL technology developed to date is divided into three parts. The first part is based on the two pulse sequences using the PERL encoding field (Figures 4.2.2 and 4.6.1) and the penetration problem for periodic fields (Eq. 4.5.14). The result is a new opportunity for MRI in which the penetration of the PERL field in the direction orthogonal to its periodicity is linked to the number of required field switches in the pulse sequence. The second and third parts of this work are direct consequences of incorporating the PERL field for spatial encoding. Since the PERL filed is nonlinear along one direction, the reconstruction of the PERL signal requires the definition and characterization of a new transform called the PERL transform illustrated in Figure 5.2.1. The PERL transform provides a stable reconstruction algorithm for the x-component of the image spin density as seen in the Figures accompanying Section 6.3. Finally, the PERL field requires a coil design to perform the encoding and an evaluation of working volume of the coil. The usable region of the PERL coil may be recast as an efficiency criteria for developing a coil with a periodic dependence on a spatial variable.

Section 9.2 Future Work

The work presented in this thesis is part of a long term project based at the Brigham and Women's Hospital in Boston, MA, and while this thesis focuses on the work original to the author, the immediate project plans of the PERL technology are briefly sketched here. These goals include fabrication of a prototype PERL coil as specified in Chapter 8 in order to test and if necessary modify the theory as described in this thesis. This prototype coil will then require field mapping. This map will serve three purposes: 1) to evaluate the relationship between the true field an the target field, 2) to determine the working volume for imaging, and 3) to provide feedback for future designs.

There are several theoretical aspects of the PERL technology which require experimental determination with a prototype unit. Three specific issues are 1) the effect of experimental noise on the reconstruction algorithm, 2) the overall point-spread function of the imaging sequence, and 3) the SNR of the PERL technology in relation to standard spin echo techniques. In addition, the noise-power spectrum created by the PERL transform reconstruction will be evaluated.

Finally, as suggested by Appendix 1, the consequences of the PERL transform are of interest beyond the scope of imaging and are under investigation. This Appendix provides the mathematical relationship between the PERL transform and the Fourier transform, but it does not give a true intuitive sense of the PERL transform. In contrast, a deep understanding of the Fourier transform is obtained by deriving the FT theorems and observing their effects in the spatial and frequency domains. The PERL transform, like all of the novel and interesting results in this thesis, is a direct outgrowth of the periodic component of the field incorporated into the complex exponential form of the signal. The physical intuition behind this application is seen in the penetration problem for periodic fields and the efficiency criteria of the coil, but the deep mathematical intuition behind

the PERL transform (such as the one which exists for the Fourier transform) remains elusive and fascinating.

APPENDIX 1. The PERL expansion.

This appendix derives the relationship between the PERL expansion and the Fourier expansion. Consider an arbitrary function f(x) defined over the interval [-L, L]. The Fourier expansion of f(x) is

$$f(x) = \frac{1}{2}a_0 + \sum_{l=1}^{\infty} \left(a_l \cos \frac{l\pi x}{L} + b_l \sin \frac{l\pi x}{L} \right). \qquad [A1.1]$$

The function f(x) may also be represented over the same region by the expansion

$$f(x) = \sum_{m=0}^{\infty} c_m \phi_m(x) \qquad [A1.2]$$

where $\phi(x) = \sum_{n=0}^{\infty} \alpha_{nm} f_n(x)$, $f_n(x) = \frac{1}{x} J_{n+1}(kx)$, and $f_n(x)$ can itself be expanded as

$$f_n(x) = \frac{1}{2}a_{0n} + \sum_{l=1}^{\infty} \left(a_{ln} \cos \frac{l\pi x}{L} + b_{ln} \sin \frac{l\pi x}{L} \right). \qquad [A1.3]$$

Then the Fourier coefficients in Equation [A1.1] can be expressed in terms of the new expansion coefficients as follows:

$$a_0 = \sum_{m=0}^{\infty} \sum_{n=0}^{\infty} a_{0n} \alpha_{nm} c_m, \qquad [A1.4]$$

$$a_l = \sum_{m=0}^{\infty} \sum_{n=0}^{\infty} a_{ln} \alpha_{nm} c_m, \qquad [A1.5]$$

and

$$b_l = \sum_{m=0}^{\infty} \sum_{n=0}^{\infty} b_{ln} \alpha_{nm} c_m. \qquad [A1.6]$$

Similarly, the coefficient of the new expansion, c_m, is related to the Fourier coefficients by the expression

$$c_m = \frac{1}{2}a_0 K_m + \sum_{l=1}^{\infty} (a_l C_{lm} + b_l S_{lm}) \qquad [A1.7]$$

where

$$K_m = \int_{-L}^{L} g_m(x)\, dx, \qquad [A1.8]$$

$$C_{lm} = \int_{-L}^{L} g_m(x) \cos \frac{l\pi x}{L} dx, \qquad [A1.9]$$

and

$$S_{lm} = \int_{-L}^{L} g_m(x) \sin \frac{l\pi x}{L} dx. \qquad [A1.10]$$